# Heterogeneous catalysts for the linear oligomerization of olefins

By

Joseph P. Chada

A dissertation submitted in partial fulfillment of

the requirements for the degree of

Doctor of Philosophy

(Chemical Engineering)

at the

UNIVERSITY OF WISCONSIN-MADISON

2018

Date of final oral examination: July 20th, 2018

The dissertation is approved by the following members of the final oral committee:

George W. Huber, Professor, Chemical and Biological Engineering
Thatcher W. Root, Professor, Chemical and Biological Engineering
Daniel J. Klingenberg, Professor, Chemical and Biological Engineering
Reid Van Lehn, Assistant Professor, Chemical and Biological Engineering
Ive Hermans, Professor, Chemistry

# Heterogeneous catalysts for the linear oligomerization of olefins

Joseph P. Chada

Under the supervision of Professor George W. Huber at the University of Wisconsin-Madison

## Abstract

The oligomerization of olefins is a valuable route to produce fuels and chemicals from light hydrocarbon ($C_2$-$C_4$) feedstocks. Recent increases in both the availability of natural gas-derived ethylene and the demand for linear polymer precursors has driven research for the development of heterogeneous catalysts capable of selectively producing linear oligomers. Previous reports have suggested that heterogeneous systems suffer from lower activity, selectivity, and stability compared to homogeneous, catalytic systems predominantly used in the chemical industry. This dissertation is focused on the design and characterization of heterogeneous, catalytic materials for linear oligomerization reactions.

In Chapter 2, we investigate the use of an acidic, medium-pore zeolite, H-ferrierite, as an olefin oligomerization catalyst. The effect of temperature, pressure, and solvent on 1-butene conversion was studied. With the use of two-dimensional gas chromatography, reaction products were extensively characterized. We found that the selectivity towards oligomerization products could be maximized at temperatures below 200°C. While cracking and aromatization reactions were effectively suppressed, products contained a high number of chain branching due to skeletal isomerization. H-ferrierite was relatively stable for production of longer chain olefins ($C_6$–$C_{20}$) in supercritical conditions. The deactivation rate decreased with increasing 1-butene partial pressure.

In Chapter 3-6, we evaluated a heterogeneous, carbon-supported cobalt oxide catalyst to selectively produce linear octenes with 87% selectivity from oligomerization of liquid-phase 1-butene in a continuous flow reactor. Chapter 3 is focused on the characterization of reaction products and the bulk material properties of cobalt oxide. Major products of 1-butene dimerization primarily included linear internal octenes (2-, 3-, and 4-octene). In Chapter 4, we demonstrate a two-step process that combines the carbon-supported cobalt oxide catalyst with a homogeneous Rh-BiPhePhos catalyst to further upgrade internal linear oligomers to linear aldehydes with a normal/isomeric (N/I) ratio of 3.8. This process demonstrates a potential route to produce linear aldehydes from light olefins.

Chapter 5 and Chapter 6 focus on the characterization of the cobalt oxide surface sites. In Chapter 5, the role of the support material on the formation of the active species is tracked with temperature-programmed desorption techniques. It was found that the activated carbon support can react with a cobalt nitrate precursor under synthesis conditions and reduce the oxidation state of the surface from $Co^{3+}$ to $Co^{2+}$. In Chapter 6, we summarize characterization efforts for the $CoO_x$/C catalyst outlined in Chapters 3-4 as well as a chromium-promoted cobalt oxide catalyst with enhanced activity. Finally, we conclude with a summary of the findings of this dissertation and recommendations for future studies.

# Acknowledgments

First and foremost, I would like to thank my advisor, Professor George W. Huber, for his support and guidance over the past five years. The pursuit of scientific answers to research questions is a challenging endeavor. I am confident that the journey has been more enjoyable because I have been able to work with a PI who ensures that his students are not only solving the right problems but also satisfied with their growth as researchers. I have never met a more capable connector who has opened routes to both exciting projects and new collaborators. In addition, I would like to thank my committee members, Prof. Thatcher Root, Prof. Daniel Klingenberg, Prof. Reid Van Lehn, and Prof. Ive Hermans for their interest in my work.

I would like to thank the many bright researchers of the Huber Research Group. From day one, we have always been an open and collaborative team. I've been a part of several research groups yet this one will always be special to me as a collection of people who would generously devote time to helping each other solve problems. To Ani, Jechan, Yong, Insoo, Zhuoran, Kevin, Dan, Nat, Siddarth, Peter, Ted, Alvin, Mark, Anthony, and Keishla, I appreciate all your hard work and long hours. Specifically, I want to acknowledge Yong, Zhuoran, Dongting, and Alvin for their contributions to the olefin oligomerization project. I am also indebted to some of the most impressive undergraduate researchers who in many cases were just as influential on my work as I (hopefully) was on their development. Zach, Bradley, Kimmy, Brandon, and Andy thank you for your efforts in the lab.

I am grateful for the financial support of the Dow Chemical Company and the Wisconsin Alumni Research Foundation. To the "Dow team", which consisted of Devon, Jessica, and Yomaira, I appreciate the amount of time invested in proofreading manuscripts, searching for resources, and providing me with the opportunity to complete an internship in Texas. Being able

to experience the scale of a commercial laboratory and chemical plant was an incredible learning experience.

To my parents, I thank you for always being supportive of my personal endeavors. I've never had to go a single day not knowing that I have a family that believes in me. Finally, I need to thank my partner, Andrea. I will never be able to fully express what your unwavering support means to me.

The complete list of people who have influenced me along the way is too long to list in its entirety. To those of you who have been a part of this journey so far, it means the world to me.

# Table of Contents

# List of Figures

# List of Tables

# Chapter 1. Introduction

## 1.1 Supply chain for light olefins

Ethylene, one of the world's most manufactured commodity chemicals, is primarily produced by the steam cracking of light hydrocarbons (e.g. ethane, propane). Annual production is estimated to be 1.5 x $10^8$ tonnes [1, 2]. In the U.S., the major source of these light hydrocarbons is from the extraction of natural gas plant liquids (NGPLs) during shale gas production. Technological advancements in horizontal drilling and hydraulic fracturing have drastically increased the supply of these light hydrocarbons [3]. Since 2010, U.S. production of dry natural gas and NGPLs has risen steadily; in that time, the production of ethane and propylene has nearly doubled (Figure 1.1) [4]. Consequently, to be able to process the increased supply, the petroleum industry has invested in new ethane-based steam crackers that are projected to increase current U.S. ethylene production by an additional 1 x $10^7$ tonnes by 2020 [2].

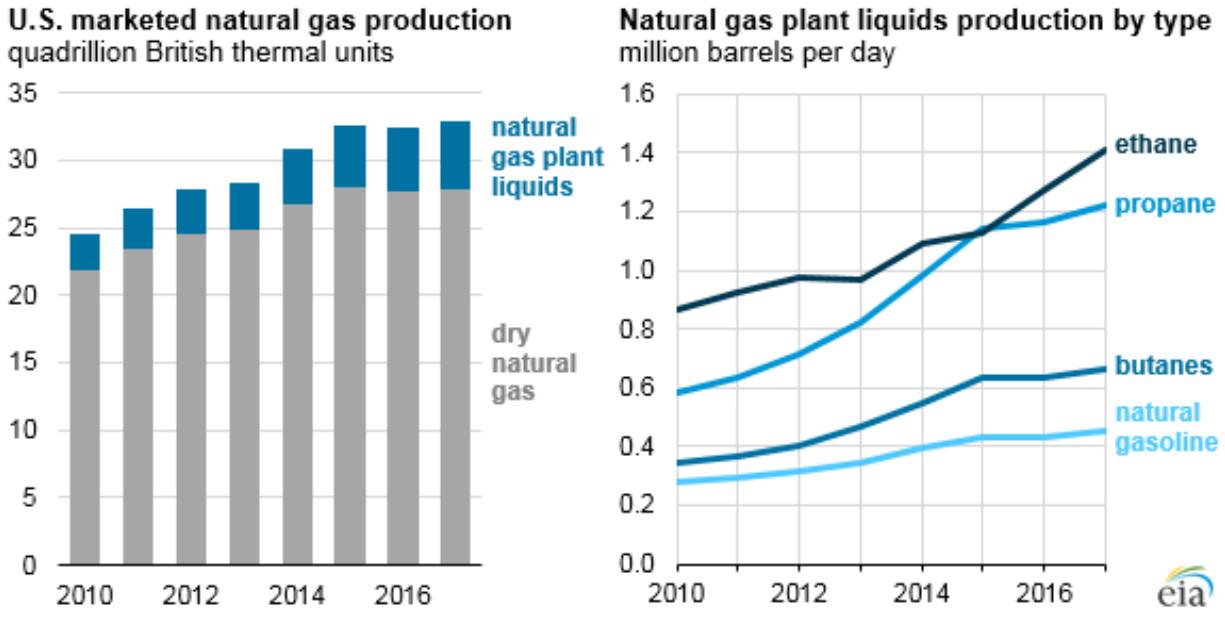


**Figure 1.1** Summary of U.S. natural gas and NGPLs production from 2010-2017. Source: U.S. Energy Information Administration (Jun 2018). [4]

Ethylene's predominant industrial use is as a precursor to polyethylene, which comprises 60% of all ethylene consumption [1, 5]. Polyethylene is typically classified as either high-density (HDPE), low-density (LDPE), or linear low-density polyethylene (LLDPE) based on both the bulk density of the material and the degree of branching of the polymer chain. The physical properties of the former two polymers can be modified by changing reaction conditions and the type of catalyst used. The latter, LLDPE, is manufactured by a controlled copolymerization of ethylene with a linear alpha olefin (LAO; i.e. 1-butene, 1-hexene, 1-octene). The uniform branch length in LLDPE, caused by the LAO comonomer addition, translates to unique properties (i.e. impact and puncture resistance) making it a useful material for the film and packaging industries [5]. Current estimates expect LLDPE markets to expand at a combined annual growth rate (CAGR) of 5.5% from 2017-2022. [6] To meet the increasing demand for LAO comonomers in LLDPE production, research is being devoted to developing new catalysts and processes capable of selectively converting ethylene into high-valued LAOs.

## 1.2 Olefin oligomerization technology

As of 2010, six of the seven largest commercial processes for the production of LAOs were based on the oligomerization of ethylene [1]. Sasol, the exception, separates LAOs from Fischer-Tropsch synthesis (FTS) products. Most ethylene oligomerization to LAOs is currently performed with various homogeneous catalysts, such as aluminum alkyls (INEOS, Gulf, CP Chemicals Process), nickel ligand catalyst (Shell), mixtures of zirconium tetrachloride, an aluminum alkyl, and a Lewis base (Idemitsu), and Ziegler Natta-type titanium complex with triethylaluminum (IFP) [7]. Due to the expensive catalyst separation and environmentally-unfriendly solvents required by the homogeneous reactions, there is a strong motivation for heterogeneous oligomerization

research. Both the activity and selectivity of current processes for converting light olefins ($C_2$-$C_4$) to linear oligomer products, however, cannot be attained with heterogeneous catalysts.

The large product distribution serves as a major drawback of most commercial LAO manufacturing. Catalytic chain growth mechanisms have been shown to follow a statistical Schulz-Flory distribution, given in Eqn. 1.1.

$$f_\alpha(k) = \alpha^2 k(1-\alpha)^{k-1} \quad [1.1]$$

Originally proposed for polymerization, the Schulz-Flory distribution provides the theoretical weight fraction of a chain of length ($k$) as a function of the chain growth probability ($\alpha$) [8-10]. Even though the chain growth probability can be adjusted by varying reaction conditions, if each monomer addition has the same probability of insertion, regardless of chain length, then product mixtures will form a statistical distribution irrespective of the catalyst or mechanism. The desirable range for useful LAOs will not often match that of a Schulz-Flory distribution. The INEOS process involves stoichiometric chain growth followed by a final displacement step in which excess ethylene replaces a growing olefin on the alkyl aluminum catalyst effectively stopping the chain growth and forming a product mixture with a narrower Poisson distribution [7].

## 1.3 Solid acid oligomerization catalysts

Oligomerization is well-known to occur over acidic catalysts via a carbocation mechanism. Numerous studies have explored various acidic support such as silica-alumina [11], zeolites [12-14], and bifunctional metal-exchanged supports [15-19] for the production of both branched and linear oligomers. Zeolites have been known for decades as shape-selective catalysts for certain reactions and have been investigated for oligomerization for this reason. Shape selectivity in zeolites can be defined as a deviation from a statistically expected product distribution by the stabilization or exclusion of certain reactions by the confining aluminosilicate framework [20]. If

the void space inside pores matches the size of a reaction transition state, this can result in enzyme-like behaviors. Figure 1.2 shows a representation of the types of shape-selectivity known to occur within the confined pore structures of zeolites.

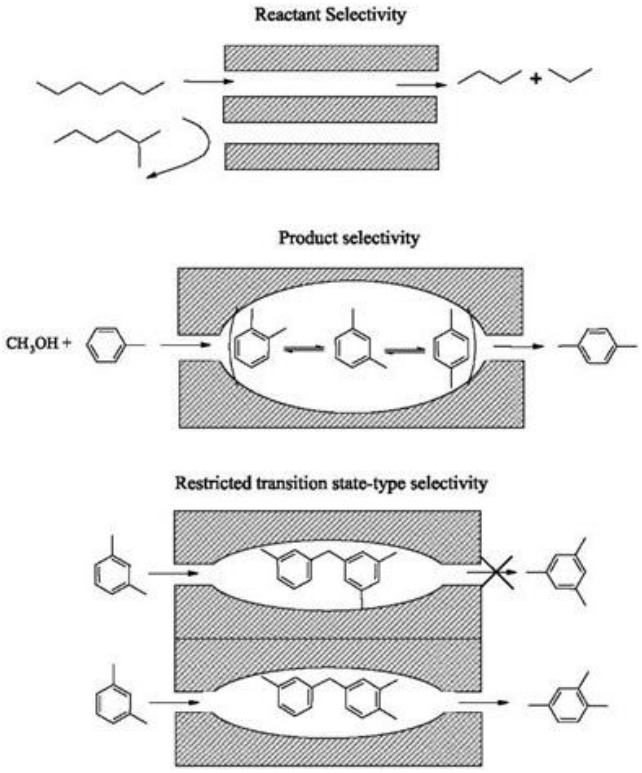


**Figure 1.2.** Representation of shape-selectivity within pores of zeolites (Reproduced from [21] with permission from Elsevier).

Several groups have explored the theory that the shape selectivity of zeolites can be used to increase selectivity towards oligomerization or ideally linear chain olefins (LCO). Particularly, medium-pore zeolites have been proposed for oligomerization to linear molecules as their pore openings are on the same scale as n-oligomers [22]. Several groups have published convincing evidence to support this hypothesis. The group of Martens has shown that the pore structure of ZSM-57 was particularly selective towards $C_8$ olefins from butenes compared to other similar sized medium-pore zeolites [14]. An evaluation of the Lennard-Jones potentials of olefins within the

zeolite framework found the pore structure was favorable for butene adsorption and the formation of dimethyl $C_8$ species. Beltrame et al. found H-ZSM-5 with a high Si/Al ratio (80) to be selective for linear dimerization of butene at high pressure [16]. Their most selective conditions produced 36.6% n-octenes. By poisoning external, unconfined acid sites, several studies have shown increased selectivity towards linear species [12, 13]. Chen and Bridger compared surface-deactivated and unmodified H-ZSM-5 and established that reactions within confining voids were favorable for the formation of nearly linear $C_{20+}$ oligomers while products of unmodified H-ZSM-5 were highly branched.

The desirable properties of metal sites and acidic supports are often combined. In the specific case of nickel-exchanged zeolites, it is still unclear if the appearance of selectivity is based on metal coordination chemistry or the shape selective nature of the support. It has been suggested that bifunctional metal-exchanged catalysts with acid sites are generally more active for oligomerization although it is not yet clear the function of the acid site. Recently, several groups have presented evidence that acidic framework plays a role in the activation of Ni sites [23, 24]. Mlinar et al. studied propylene oligomerization on Ni-exchanged zeolites, mesoporous materials and MOFs [17-19, 25]. Surprisingly, they ascertained that the most active and selective supports were larger pore MOFs. It has been claimed by several authors that the larger openings allow less restricted access to the active metal site [26-28].

It can be challenging to accurately characterize metals in aluminosilicate materials. By use of in situ XANES, Mlinar et al. showed that the active species in Ni-X zeolite was $Ni^{2+}$ and remains unchanged after the exposure to propylene [17]. Importantly, they observed an activation period with TOS that was believed to be the migration of nickel within the zeolite cage. Franken et al. synthesized a CoCaNa-Y zeolite that was selective for the production of semi-linear oligomers

from 1-butene [29]. They attributed the enhanced selectivity to the confined positions of the cations within the pores of the faujasite zeolite (Y).

## 1.4 Transition metal oligomerization catalysts

Classes of heterogeneous oligomerization catalysts include immobilized metal complexes, supported transition metals, and solid acid catalysts [26, 30]. Efforts to immobilize active homogeneous species have largely been unsuccessful, as they cannot match the activity of the homogeneous system [31]. The most studied transition metals known to oligomerize light olefins include Ni, Pd, Ti, Zr, Al, Cr, and Co, of which, Ni is generally regarded as the most active and cost-effective for heterogeneous systems. [31, 32] Reports of metals supported on inorganic, porous structures are generally limited to Ni [16, 33-37] and Co [38-40]. Information is presented here on Ni-based catalysts as they participate in similar reaction mechanisms and have comparable properties as cobalt. Many different oxidations states have been reported as the most active for oligomerization. Several sources have claimed NiO [35], $Ni^{+}$ [41, 42], or $Ni^{2+}$ [43] to be the active oligomerization site. Even more, complexity is added when acidic supports are used as the active nickel may require a neighboring Brønsted site [23, 24, 26]. A correct understanding of the active oxidation state, role of a bifunctional acid site, or catalyst mechanism would be a significant contribution to the field. It is believed that the reaction mechanism for heterogeneous systems follows similarly to the commonly recognized mechanisms for homogeneous catalysts, namely, either a Metallocycle or Cossee-Arlman mechanism (Figure 1.3). The Cossee-Arlman mechanism has been recently suggested by several research groups as the most likely mechanism for supported Ni systems [24, 44].

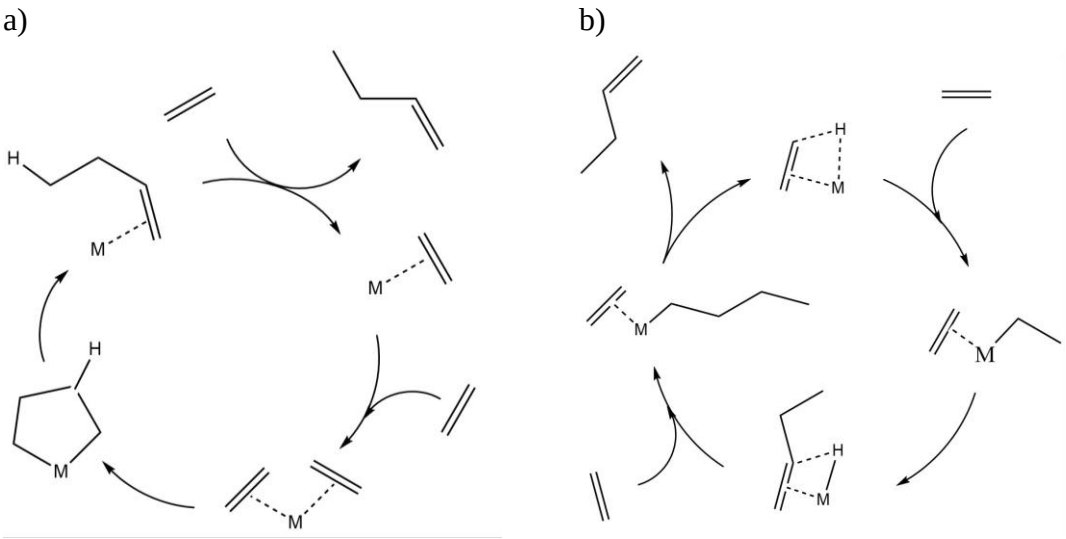


**Figure 1.3.** Commonly recognized ethylene oligomerization mechanisms for homogeneous catalysts. a) Metallacycle and b) Cossee-Arlman Mechanism. Adapted from [24]

Cobalt oxide on carbon, a catalyst described in Chapters 3-6, has been reported by few sources for oligomerization. Originally proposed by Schuster for ethylene dimerization in 1932 [40], further reports by Cheney et al. in 1950 [45] and Schultz et al. in 1966 [38, 39], establish its use for oligomerization. Experiments by Schultz et al. have shown linear selectivity of 41%, 52%, 65%, and 83% for ethylene, propylene, 1-butene, and 1-hexene, respectively, towards linear olefins. Internal olefins were observed in the highest concentrations. Some interesting observations included the sensitivity to the preparation technique. For example, the addition of ammonia to the support and catalyst resulted in a 4-fold increase in activity. Cobalt on silica-alumina, silica-magnesia, and alumina produced mostly branched products. It was even found that the conversion (not product distribution) was dependent on the type of carbon support used. Catalysts were found to be most active after pretreated at 275°C with enhanced isomerization activity at higher temperatures (500°C). Surprisingly, the highest activity was claimed to be at 25°C with higher temperatures (85°C) showing less activity. Elemental analysis showed that the

oxidation state is sensitive to pretreatment and ammonia addition but the results were not conclusive in support of either $Co^{2+}$ or $Co^{3+}$.

## 1.5 Thesis scope

The previously mentioned studies suggest that both confined zeolite frameworks and supported transition metals have the potential to compete with homogeneous systems for the oligomerization of light olefins. In this thesis, we discuss our efforts to design and characterize heterogeneous, catalytic materials for linear oligomerization reactions.

In Chapter 2, the effect of temperature, pressure, and solvent on 1-butene oligomerization was studied over H-ferrierite. Two-dimensional gas chromatography (GCxGC-MS) was used to analyze the olefin, paraffin, aromatic, and cycloalkane products of the $C_4$ olefin conversion. The reaction product mixture revealed that H-ferrierite promoted double-bond and skeletal isomerization, oligomerization, hydrogen transfer, cyclization and cracking reactions. Double-bond isomerization reactions reached equilibrium for both $C_4$ and $C_8$ olefins. Most of the heavier olefins ($>C_{12}$) were highly branched (>trimethyl- and methyl-ethyl-species). The selectivity towards oligomerization products was maximized at low temperatures (below 473 K). At temperatures above 473 K olefins underwent cracking and hydride transfer reactions to produce olefins, paraffins, and aromatics. Co-feeding hexane solvent increased $C_4$ olefin conversion and led to a shift of the product distribution from heavier to lighter species. The medium pores were relatively stable for production of longer chain olefins ($C_6$–$C_{20}$) from $C_4$ olefins near supercritical conditions which could make catalyst potentially viable for fuel production.

In Chapter 3, we report on the production of linear octenes in high (70−85%) selectivity from oligomerization of liquid 1-butene using carbon-supported cobalt oxide catalysts in a continuous flow reactor. The liquid products were characterized by GCxGC-MS. Above 95% of

the oligomers were $C_8$ olefins, with the other products primarily being branched $C_{12}$ olefins. The activated catalyst contained both $Co_3O_4$ and CoO as confirmed by x-ray diffraction (XRD), in situ Raman spectroscopy, and x-ray absorption spectroscopy. The cobalt oxide particle size was estimated to be between 5 and 10 nm by high-resolution transmission electron microscopy and x-ray diffraction. The $Co^{3+}$ : $Co^{2+}$ ratio decreased with increasing pretreatment temperature.

In Chapter 4, a two-step process was demonstrated for the conversion of 1-butene to n-nonanal with an overall reaction selectivity of 70.8% (Figure 1.4). The process consists of a dimerization step over a carbon-supported cobalt oxide catalyst to a mixture of oligomers, consisting primarily of internal linear octenes. After product distillation, the olefinic mixture was converted to C9 aldehydes with a normal/isomeric (N/I) ratio of 3.8 over a homogeneous Rh/BiPhePhos catalyst. This work demonstrates a new route to produce linear aldehydes from light olefins.

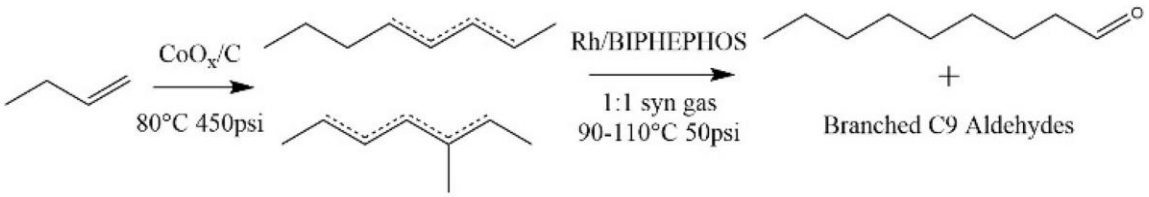


**Figure 1.4.** Catalytic reaction route to produce n-nonanal from 1-butene by first oligomerizing the terminal olefin to an equilibrium mixture of linear and mono-branched isomers followed by the tandem isomerization/hydroformylation to the corresponding aldehyde. Double-bond positions of the major $C_8$ products are shown as dotted lines. Branched C9 aldehydes were not drawn for simplicity.

In Chapters 5 and 6, we report on the effect of the support material on the formation and activity of the cobalt oxide surface sites. Chapter 5 discusses the possible reactions that activated carbons can have with the cobalt precursor during preparation and pretreatment which result in the observed autoreductive behavior (i.e. the reduction of $Co^{3+}$ to $Co^{2+}$ to $Co^0$ with increasing temperature in an inert atmosphere when supported on carbon). Chapter 6 summarizes

characterization efforts for various carbon supported materials and their implications about the compositions of the cobalt active sites.

This thesis is concluded with suggestions for future work in Chapter 7. We suggest that further studies continue to focus on the identification of the catalytically-active cobalt oxide sites. A conclusive understanding of the cobalt coordination environment will rationally guide the development of commercially-competitive, heterogeneous oligomerization catalysts.

## 1.6 References


1. K.M. Sundaram;, M.M. Shreehan;, E.F. Olszewski, Ethylene, in: Kirk-Othmer Encyclopedia of Chemical Technology, 2010.
2. I. Amghizar, L.A. Vandewalle, K.M. Van Geem, G.B. Marin, New Trends in Olefin Production, Engineering, 3 (2017) 171-178.
3. Natural Gas Liquids Primer: With a Focus on the Appalachian Region, in, U.S. Department of Energy, December 2017.
4. S. MacIntyre, Ethane production growth led to record U.S. natural gas plant liquids production in 2017, in, U.S. Energy Information Administration, 2018.
5. Polyethylene, in: Ullmann's Encyclopedia of Industrial Chemistry.
6. Linear Low-Density Polyethylene (LLDPE) Market by Application (Films, Injection Molding, Rotomolding), Process Type (Gas Phase, Solution Phase, Slurry Loop) & Region (APAC, North America, Europe, Middle East, Latin America) - Global Forecast to 2022, in, Research and Markets, March 2018.
7. G.R. Lappin;, L.H. Nemec;, J.D. Sauer;, J.D. Wagner, Olefins, Higher, in: Kirk‐Othmer Encyclopedia of Chemical Technology. 2000.
8. G.V.Z. Schulz, Phys. Chem., Abt. B, (1935) 379-398.
9. G.V.Z. Schulz, Phys. Chem., Abt. B, (1939) 25-46.
10. P.J. Flory, Molecular Size Distribution in Ethylene Oxide Polymers, J. Am. Chem. Soc., 62 (1940) 1561-1565.
11. S. Peratello, M. Molinari, G. Bellussi, C. Perego, Olefin Oligomerization: Thermodynamics and Kinetics over a Mesoporous Silica-Alumina. Catal. Today, 52 (1999), pp. 271-277.
12. K.G. Wilshier, P. Smart, R. Western, T. Mole, T. Behrsing, Oligomerization of Propene over H-Zsm-5 Zeolite, Appl Catal, 31 (1987) 339-359.
13. C.S.H. Chen, R.F. Bridger, Shape-Selective Oligomerization of Alkenes to Near-Linear Hydrocarbons by Zeolite Catalysis, J. Catal., 161 (1996) 687-693.
14. J.A. Martens, R. Ravishankar, I.E. Mishin, P.A. Jacobs, Tailored Alkene Oligomerization with H-ZSM-57 Zeolite, (2007).
15. M. Bjørgen, K.-P. Lillerud, U. Olsbye, S. Bordiga, A. Zecchina, 1-Butene Oligomerization in Bro1nsted Acidic Zeolites: Mechanistic Insights from Low-Temperature in Situ FTIR Spectroscopy, J. Phys. Chem. B, 108 (2004) 7862-7870.
16. P. Beltrame, L. Forni, A. Talamini, G. Zuretti, Dimerization of 1-butene over nickel zeolite catalysts: A search for linear dimers, Appl. Catal. A: Gen., 110 (1994) 39-48.
17. A.N. Mlinar, G.B. Baur, G.G. Bong, A.B. Getsoian, A.T. Bell, Propene oligomerization over Ni-exchanged Na-X zeolites, J. Catal., 296 (2012) 156-164.
18. A.N. Mlinar, B.K. Keitz, D. Gygi, E.D. Bloch, J.R. Long, A.T. Bell, Selective Propene Oligomerization with Nickel(II)-Based Metal–Organic Frameworks, ACS Catalysis, 4 (2014) 717-721.
19. A.N. Mlinar, S. Shylesh, O.C. Ho, A.T. Bell, Propene Oligomerization using Alkali Metal- and Nickel-Exchanged Mesoporous Aluminosilicate Catalysts, ACS Catalysis, 4 (2014) 337-343.
20. B. Smit, T.L. Maesen, Towards a molecular understanding of shape selectivity, Nature, 451 (2008) 671-678.

21. S.M. Csicsery, Shape-selective catalysis in zeolites, Zeolites, 4 (1984) 202-213.
22. N.Y. Chen;, J. Thomas, F. Degnan;, C.M. Smith, Molecular Transport and Reaction in Zeolites: Design and Application of Shape Selective Catalysts, John Wiley & Sons., 1994.
23. I. Agirrezabal-Telleria, E. Iglesia, Stabilization of active, selective, and regenerable Ni-based dimerization catalysts by condensation of ethene withinordered mesopores, J. Catal., 352 (2017) 505-514.
24. R.Y. Brogaard, U. Olsbye, Ethene Oligomerization in Ni-Containing Zeolites: Theoretical Discrimination of Reaction Mechanisms, ACS Catalysis, 6 (2016) 1205-1214.
25. A.N. Mlinar, O.C. Ho, G.G. Bong, A.T. Bell, The Effect of Noncatalytic Cations on the Activity and Selectivity of Nickel-Exchanged X Zeolites for Propene Oligomerization, ChemCatChem, 5 (2013) 3139-3147.
26. A. Finiels, F. Fajula, V. Hulea, Nickel-based solid catalysts for ethylene oligomerization – a review, Catalysis Science & Technology, 4 (2014) 2412.
27. R.D. Andrei, M.I. Popa, F. Fajula, V. Hulea, Heterogeneous oligomerization of ethylene over highly active and stable Ni-AlSBA-15 mesoporous catalysts, J. Catal., 323 (2015) 76-84.
28. V. Hulea, F. Fajula, Ni-exchanged AlMCM-41?An efficient bifunctional catalyst for ethylene oligomerization, J. Catal., 225 (2004) 213-222.
29. J. Franken, C.E.A. Kirschhock, G.M. Mathys, J.A. Martens, Design of a Cobalt-Zeolite Catalyst for Semi-Linear Higher-Olefin Synthesis, ChemCatChem, 4 (2012) 1245-1248.
30. A.M. Al-Jarallah, J.A. Anabtawi, M.A.B. Siddiqui, A.M. Aitani, A.W. Al-Sa'doun, Ethylene dimerization and oligomerization to butene-1 and linear α-olefins:A review of catalytic systems and processes, Catal. Today, (1992).
31. H. Zhang, X. Li, Y. Zhang, S. Lin, G. Li, L. Chen, Y. Fang, H. Xin, X. Li, Ethylene Oligomerization Over Heterogeneous Catalysts, Energy and Environment Focus, 3 (2014) 246-256.
32. J. Skupinska, Oligomerization of a-Olefins to Higher Oligomers, Chemical Reviews, 91 (1991) 613-648.
33. R.L. Espinoza, C.J. Korf, C.P. Nicolaides, R. Snel, Catalytic oligomerization of ethene over nickel-exchanged amorphous silica-alumina; effect of the reaction conditions and modelling of the reaction, Appl Catal, 29 (1987) 175-184.
34. F.T.T. Ng, D.C. Creaser, Ethylene dimerization over modified nickel exchanged Y-zeolite, Appl. Catal. A: Gen., 119 (1994) 327-339.
35. R. Spinicci, A. Tofanari, A study of proplyene oligomerization on silica alumina supported nickel oxide, (1990).
36. M. Lallemand, A. Finiels, F. Fajula, V. Hulea, Catalytic oligomerization of ethylene over Ni-containing dealuminated Y zeolites, Appl. Catal. A: Gen., 301 (2006) 196-201.
37. M. Lallemand, O.A. Rusu, E. Dumitriu, A. Finiels, F. Fajula, V. Hulea, NiMCM-36 and NiMCM-22 catalysts for the ethylene oligomerization: Effect of zeolite texture and nickel cations/acid sites ratio, Appl. Catal. A: Gen., 338 (2008) 37-43.
38. R.G. Schultz, Olefin dimerization over cobalt-oxide-on carbon catalysts II: Dimerization of butene and hexene, J. Catal., 6 (1966) 419-424.

39. R.G. Schultz, Olefin dimerization over cobalt-oxide-on-carbon catalyst: I. Proplyene dimerization, J. Catal., 6 (1966) 385-396.
40. H.C. Schuster, UBEK KATALYTISCHE HYDRIERUNG UNI) POLYMERISATION, Z. Elektochem., (1932).
41. L. Bonneviot, D. Olivier, M. Che, Dimerization of olefins with nickel-surface complexes in X-type zeolite or on silica, J. Mol. Catal., 21 (1983) 415-430.
42. M. Lallemand, A. Finiels, F. Fajula, V. Hulea, Nature of the Active Sites in Ethylene Oligomerization Catalyzed by Ni-Containing Molecular Sieves: Chemical and IR Spectral Investigation, J. Phys. Chem. C, 113 (2009) 20360-20364.
43. J. Heveling, C.P. Nicolaides, M.S. Scurrell, Catalysts and conditions for the highly efficient, selective and stable heterogeneous oligomerisation of ethylene, Appl. Catal. A: Gen., 173 (1998) 1-9.
44. E.D. Metzger, R.J. Comito, C.H. Hendon, M. Dincă, Mechanism of Single-Site Molecule-Like Catalytic Ethylene Dimerization in Ni-MFU-4l, Journal of the American Chemical Society, 139 (2017) 757-762.
45. H.A. Cheney, S.H. McAllister, E.B. Fountain, J. Anderson, W.H. Peterson, Ethylene to butylene, (1950).

# Chapter 2. Low-temperature oligomerization of 1-butene with H-ferrierite[1]

## 2.1 Introduction

The advent of fracking technology has resulted in plentiful liquefied natural gas (LNG) resources, a cost-advantaged raw material for the chemical processing industry [1]. Olefins, propylene, and butenes, in particular, can be produced by steam cracking of LNGs [2]. They are readily available, cost-efficient, and easily converted into liquid fuels (i.e., gasoline and diesel) or chemical intermediates for a wide array of applications (i.e., surfactant, performance plastics, and elastomers) [3–5]. In particular, butenes in the $C_4$ stream of refinery and steam cracking units have received considerable attention in recent years [6]. Oligomerization of olefins into mixtures of longer chain olefins that contain $C_6$–$C_{16}$ carbon atoms has been demonstrated by solid–acid catalysts [4,5,7,8]. Compared to the commonly employed homogeneous catalyst, zeolitic systems have the advantages of being regenerable and stable over a wide temperature range and being able to process olefins feeds that contain mixtures of olefins. Zeolites also have the potential to control the product distribution by judicious catalyst and process parameter selection [9–16]. It has been shown, using density functional theory, that pore confinement effects inside zeolites (ZSM-5 and

---

[1] This chapter was adapted with permission from: Yong Tae Kim, Joseph P. Chada, Zhuoran Xu, Yomaira J. Pagan-Torres. Devon C. Rosenfeld, William L. Winniford, Eric Schmidt, George W. Huber, Low-temperature oligomerization of 1-butene with H-ferrierite, J. Catal., 2015, 323, 33-44.

Author contributions: Y.T.K., J.P.C., Z.X., and G.W.H designed research; Y.T.K. collected BET and TGA data; J.P.C. collected oligomerization data; Z.X. prepared catalysts and analyzed reaction pathway; Y.J.P.T, D.C.R, W.L.W, and E.S. assisted with analytical setup and provided technical guidance; and Y.T.K., J. P. C. and G.W.H. wrote the paper.

ZSM-22) increase the rate of ethylene dimerization reactions [17]. In addition, the shape selectivity of the zeolites can be used to tune the product selectivity [14–16]. One potential opportunity is that tuning the zeolite pore shape and internal pore structure of the zeolite will allow us to make target longer chain olefins more selectively for chemical applications.

Different zeolite frameworks have varying pore networks that influence the reaction selectivity for olefin oligomerization. Changing the zeolite structure influences the diffusivity of both reactants and products in this reaction. Medium-pore zeolites (constraint index between 1 and 12) having 10-ring channels are suitable structures for selective production of $C_8$–$C_{12}$ olefins through $C_4$ olefin oligomerization [18–31]. The side reactions such as cracking and hydride transfer are suppressed by the narrow 10-ring tubular channels [32]. The volume of the zeolite cavity having the maximum included sphere diameter of around 7 Å is almost the same as that of the n-octyl carbocations [33], which could be suitable for $C_4$ olefin dimerization. For example, ferrierite (FER), ZSM-57, and ZSM-23 have a volume of 124–165 $Å^3$, which is similar to that of n-octyl carbocations (180 $Å^3$). Martens and co-workers reported that ZSM-57 has a high $C_4$ olefin conversion and a high selectivity for $C_4$ olefin dimers [18]. They also suggested that 1-dimensional channel systems such as ZSM-22 and ZSM-23 are able to minimize the number of chain branching for oligomerization products [25]. Similar in pore size to ZSM-57 and ZSM-23, FER consists of 2-dimensional, intersecting 8- and 10-ring channels [33–37]. Yoon et al. reported that FER shows stable isobutene conversion with high selectivity for butene trimers as compared with ZSM-5 and mordenite [22]. Three-dimensional ZSM-5 undergoes slow deactivation because the formation of coke precursors is sterically inhibited inside micropores [12,13]. These zeolite catalysts could potentially be further modified by controlling the location of the acid sites that could minimize the number of chain branching [25,38].

Brønsted acid sites in zeolites are known to catalyze olefin oligomerization through a classical carbocation mechanism [39]. At moderate temperature (473–573 K) and pressure (30–100 bar), the product distribution shifted to high molecular weight olefins (trimers, tetramers, etc.) [16,33]. $C_4$ olefin conversion over acid-based catalysts involves undesired side reactions that lead to the accumulation of heavy hydrocarbons (i.e., coke) in zeolite pores [34,36,40,41]. It has been shown that hydrocarbon solvents can stabilize catalytic performance in olefin oligomerization because the heavy oligomers and coke precursors can be desorbed from the catalyst pores due to their favorable solubility in the solvents [32,42–46]. The catalytic activity and stability are dependent on the physical state of the hydrocarbon solvents [42]. The solvent molecules that have a smaller volume than catalyst pores could be effective for removal of oligomerization products of a similar molecular weight from the catalyst pores [47]. For example, Hulea and Fajula reported that co-feeding n-heptane with ethylene caused a higher activity for ethylene oligomerization than co-feeding n-octane, n-decane, toluene, or cyclohexane at 423 K and 35 bar [43]. Pater et al. studied 1-hexene oligomerization with paraffin solvents at 473 K and 50 bar over large-pore USY zeolite [42]. They found that the catalyst had a higher rate for 1-hexene conversion and was more stable when liquid-phase octane and dodecane solvents were used [42]. Medium-pore ZSM-5 is stable for 100 h TOS under supercritical conditions for 1-hexene oligomerization at 508 K [45]. Fan et al. also observed that using supercritical n-pentane as a solvent increased the activity and stability of ethylene oligomerization over ZSM-5 [46]. These studies show that the reaction pressure, temperature, and solvent co-feeds can greatly influence the activity, selectivity, and stability of zeolites such as FER for olefin oligomerization reactions.

The purpose of this chapter is to understand the catalytic reaction chemistry for $C_4$ olefin conversion over H-FER. We used two-dimensional gas chromatography (GCxGC–MS) [48] to

analyze the different types of paraffins, olefins, aromatics, and cycloalkanes produced by C4 olefin oligomerization. Catalytic measurements over H-FER were performed to elucidate differences in the reactivity as a function of conditions. The results from this chapter can be used to understand the detailed reaction mechanism about olefin oligomerization occurring within H-FER.

## 2.2 Experimental

### 2.2.1 Catalyst preparation

$NH_4$-ferrierite ($NH_4$-FER; $SiO_2/Al_2O_3$ = 20, CP914C) was purchased from Zeolyst. The as–purchased $NH_4$-FER was calcined in a muffle furnace at 823 K in stagnant air for 8 h at a heating rate of 2 K $min^{-1}$ to convert to proton form, H-FER. The structure of H-FER was verified by X-ray diffraction (XRD) (data not shown). Physicochemical properties of the H-FER are presented in Table 2.1.

### 2.2.2 Catalyst characterization

Brunauer–Emmett–Teller (BET) and Langmuir surface areas were calculated from nitrogen adsorption data at 77 K obtained using an ASAP 2020 system (Micromeritics). Before the measurements, the sample was degassed under vacuum at 523 K for 12 h. The external surface area and micropore volume were calculated by the *t*-plot method.

Temperature-programmed desorption of ammonia ($NH_3$-TPD) was conducted with approximately 100 mg of each sample in the temperature range 373–973 K at a heating rate of 10 K $min^{-1}$ under a constant He flow at 50 mL $min^{-1}$ while monitoring thermal conductivity detector signals (Autochem 2920). Prior to analysis, the sample was first saturated with $NH_3$ at 373 K for 30 min and flushed with He for 2 h. The sample was held at 973 K for an additional 2 h. All of the samples were treated at 873 K for 2 h in He before the experiments to remove adsorbed water

and organic species. The amount of adsorbed $NH_3$ was quantified with pulsed $NH_3$ injection experiments.

Thermogravimetric analysis (TGA) was conducted with approximately 20 mg of each sample in the temperature range of 318– 973 K at a heating rate of 10 K min1 under a constant $O_2$ (or N2) flow at 100 mL min1 using TA instruments Q500 system. The samples were purged with $O_2$ (or N2) at 318 K for 1 h prior to the experiments.

The bulk crystalline structure of the catalysts was determined by XRD. The XRD patterns were obtained with a high-resolution Bruker D8 Discover diffractometer using Cu Ka radiation (k = 0.15406 nm), operated at 50 kV and 1000 mA (2.0 kW) at a scan rate of 0.1° (2θ) $s^{-1}$. Crystal phases were identified using ICDD database and JADE 9.0 software package.

The amount of carbon formed on the used catalysts was determined using a total organic carbon (TOC) analyzer (Shimadzu TOC5000A). During the TOC measurement, the temperature was held at 1173 K in flowing oxygen. The surface carbon content was calculated by subtracting the amount of carbon on the fresh catalyst from that on the used catalyst.

**Table 2.1.** Physicochemical properties of H-FER.

| Sample | Langmuir surface area ($m^2/g$) | External surface area ($m^2/g$) | $V_{micropore}$ ($cm^3/g$) | Carbon deposit (wt. %)[a] | | | | |
|---|---|---|---|---|---|---|---|---|
| | | | | Total | Low (523- 539 K) | Medium (613 K) | High (769 K) | Hard coke (769 K)[b] |
| Fresh | 423.3 | 44.3 | 0.129 | - | - | - | - | - |
| After reaction at 423 K[c] | 96.9 | 17.5 | 0.026 | 9.2 (7.2) | 5.2 | - | 2.6 | 1.3 |
| After reaction at 423 K[d] | 32.9 | 13.0 | 0.053 | 11.4 (9.9) | 7.8 | - | 3.3 | 0.3 |
| After reaction at 423 K[e] | 53.7 | 11.4 | 0.014 | 10.4 (8.8) | 7.0 | - | 3.3 | 0.1 |
| After reaction at 423 K[f] | 25.4 | 12.6 | 0.003 | 10.0 (8.7) | 6.5 | - | 3.2 | 0.2 |
| After reaction at 523 K[g] | 19.8 | 8.7 | 0.003 | 9.5 (8.5) | - | 1.5 | 4.6 | 3.4 |

[a] The amount of carbon on the used catalysts was determined with TPO results. Data in parenthesis were determined with TOC analyzer.
[b] The hard coke (wt.%) is determined by the difference in total carbon deposit between TPD and TPO results.
[c] Reaction condition: $P_{1\text{-butene}} = 62.7$ bar, feed $WHSV_{1\text{-butene}} = 1.58\ h^{-1}$; $P_{total} = 62.7$ bar.
[d] Reaction condition: $P_{1\text{-butene}} = 1.2$ bar, feed hexane to 1-butene = 3.1, $WHSV_{1\text{-butene}} = 0.03\ h^{-1}$; $P_{total} = 62.7$ bar.
[e] Reaction condition: $P_{1\text{-butene}} = 0.9$ bar, feed hexane to 1-butene = 18.1, $WHSV_{1\text{-butene}} = 0.03\ h^{-1}$; $P_{total} = 62.7$ bar.
[f] Reaction condition: $P_{1\text{-butene}} = 0.8$ bar, feed hexane to 1-butene = 34.3, $WHSV_{1\text{-butene}} = 0.03\ h^{-1}$; $P_{total} = 62.7$ bar.
[g] Reaction condition: 2.0 mol% 1-butene in helium, $WHSV_{1\text{-butene}} = 0.03\ h^{-1}$; $P_{total} = 6.9$ bar, $P_{1\text{-butene}} = 0.14$ bar.

### 2.2.3 Catalytic performance studies

A schematic representation of the fixed-bed reactor system is given in Figure S2.1. 1-Butene oligomerization was carried out in a stainless-steel tubular flow reactor, in a downflow arrangement, heated by a Lindberg/blue M (TF55030A-1; Thermo Scientific) furnace. The reactor was 30.5 cm long and had an inner diameter of 8.46 mm. A uniform temperature profile along the catalyst bed was achieved by using aluminum heating block inserted into the void space between the furnace and the tubular reactor. The temperature was monitored by a K-type thermocouple contacted directly into the aluminum block. For catalytic activity measurements, 0.5–4 g of the catalyst without diluents was loaded into the reactor, held in place by quartz wool plugs. Void spaces on both ends of the catalyst were filled with glass beads (710–1180 μm, Aldrich). The catalyst was pelletized and sieved to a uniform diameter of 420–841 μm. Before the reaction, the pre-calcined catalyst was pretreated in situ in flowing helium (150 mL $min^{-1}$) at 773 K for 2 h at a heating rate of 4 K $min^{-1}$ to remove adsorbed water. After the pretreatment, the furnace was cooled to 373 K and the reactor system was pressurized to the desired reaction pressure using a backpressure regulator. The olefin feed was then fed to the reactor using mass flow controllers (SLA 5850, Brooks Instrument) (2% 1-butene 1% nitrogen in helium) or a high-pressure syringe pump (500D, Teledyne Isco) (99.9% 1-butene). Nitrogen was used as an internal standard. A chilled 75-mL stainless-steel gas-liquid separator was used to collect liquid products at the bottom of the reactor at 268 K and reaction pressure. A 50-mL glass pressure tube was installed after the back-pressure regulator to condense any residual liquid products at 0.1 MPa and 268 K. Online gas chromatography (GC; Shimadzu, 2014) was used to analyze the reactor effluent gas. $N_2$ and $CH_4$ in the gaseous products were analyzed using a thermal conductivity detector

(TCD) with a combination of Hayesep R (Supelco, Catalog No. 12085-U) and Shincarbon (Restek, Catalog No. 19808) packed column. The injection port and the detector were held at 473 K and 523 K, respectively. The column pressure was 300 kPa with He carrier gas. Hydrocarbons in the range of $C_1$ to $C_6$ components in the gaseous products were analyzed using a flame ionization detector (FID) with an RT-Alumina BOND/$Na_2SO_4$ (Restek, Catalog No. 19756). Both the injection port and the detector were held at 473 K. The column flow rate was 7.91 mL min1 with He carrier gas. The following GC oven temperature regime was used: The temperature was held at 318 K for 1 min, ramped to 453 K at 10 K $min^{-1}$, and held at 453 K for 41 min. The liquid product accumulated in the gas-liquid separators was drained periodically into a collecting container. The sampling vial was precooled to 194.5 K and preloaded with 0.5 wt% heptane in hexane solution to suppress volatilization of the liquid products. The liquid phase was analyzed using comprehensive two-dimensional gas chromatography-mass spectroscopy (GCxGC–MS) with both a FID (Agilent, 7890B) and a mass selective detector (MSD; Agilent, 5977A). A flow modulator (CFP; Agilent, G3487A) was installed to make a GCxGC system. Two capillary columns, DB-17 (Agilent, Catalog No. 121-1723) and CP-Sil 5 CB (Agilent, Catalog No. CP7700), were coupled in series with the CFP. The first-dimension column flow rate was 0.7 mL $min^{-1}$ with $H_2$ carrier gas. The second-dimension column flow rate was 25 mL $min^{-1}$ with a $H_2$ carrier gas. In all experiments, both the first and second dimensions were operated in constant flow mode. For each analysis, 0.5–1 μL of liquid sample was injected. The injection port and the detector were held at 473 K and 523 K, respectively. The following GC oven temperature regime was used: The temperature was held at 303 K for 4 min, ramped to 523 K at 5 K $min^{-1}$, and held at 523 K for 5 min. GCGC processing was done with GC-Image 2.3b data visualization software

(Zoex Corporation), as shown in Figure 2.1. All of the detected peaks were quantified using GC-FID. Unknown product peaks were identified by their mass spectra and retention indices. The conversion was calculated as moles of feedstock reacted per moles of feedstock fed to the system. The butene isomers (*trans*-2-butene and *cis*-2-butene) were grouped together and considered as the non-converted feed for calculation of $C_4$ olefin conversion. The selectivity was calculated as carbon moles of product produced per carbon moles of feedstock reacted within the system. The yield of product was calculated by carbon moles of product divided by carbon moles of feedstock fed to the system. Product distribution was defined as the ratio of carbon moles of product divided by the total carbon moles of corresponding categories (olefins, paraffins, aromatics/naphthalenes, cycloalkanes, etc.).

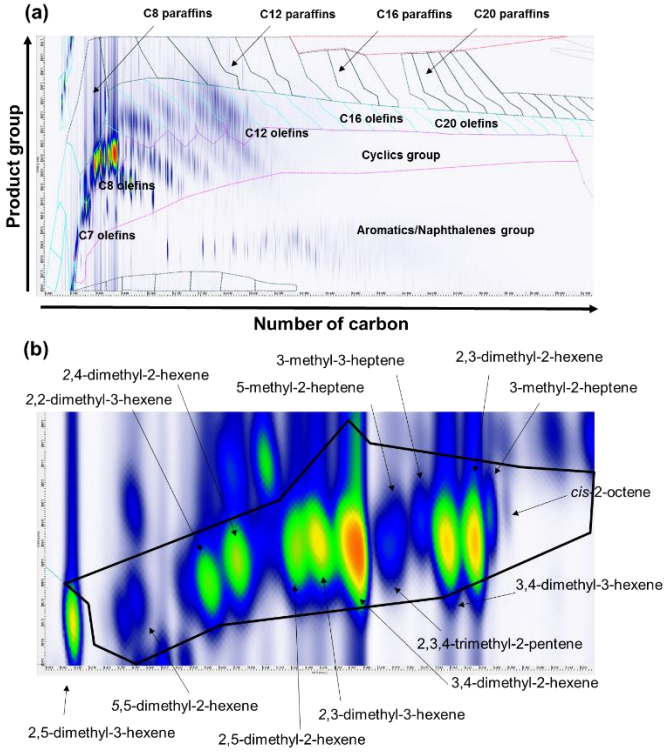


**Figure 2.1.** Separation of (a) entire products and (b) C8 olefins through 2-dimensional gas chromatography (2D-GC).

## 2.3 Results and Discussion

### 2.3.1 Effect of reaction temperature

The effect of reaction temperature on the gas-phase oligomerization of 1-butene was studied at 6.9 bar over H-ferrierite (H-FER) as shown in Figure 2.2 and Table 2.2. The $C_4$ olefin conversion, which is the conversion of linear $C_4$ olefins, increased with reaction temperature. No butenes or other products were detected during the first two hours of reaction at 373 K. Control experiments to determine system residence time at relevant reaction conditions show product detection in less than 20 min TOS. This transient period was associated with the time to fill the zeolite micropores. After this transient period, the $C_4$ olefin conversion stabilized and then slowly decreased with time on stream.

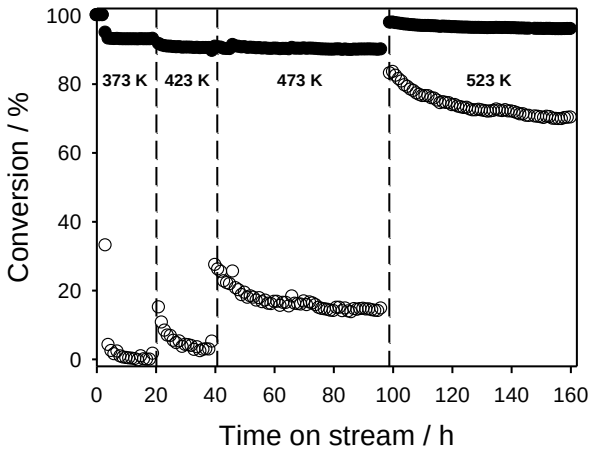


**Figure 2.2.** 1-butene conversion (●) and $C_4$ olefin conversion (○) as a function of time-on-stream and reaction temperature for oligomerization of 1-butene at low 1-butene partial pressure. Reaction condition: 2.0 mol% 1-butene in helium, $WHSV_{1\text{-butene}} = 0.03\ h^{-1}$; $P_{total} = 6.9$ bar, $P_{1\text{-butene}} = 0.14$ bar.

**Table 2.2.** Effect of reaction temperature on 1-butene oligomerization at low pressure (6.9 bar). (Reaction condition: 2.0 mol% 1-butene in helium, $WHSV_{1\text{-butene}}$ = 0.03 $h^{-1}$; $P_{total}$ = 6.9 bar, $P_{1\text{-butene}}$ = 0.14 bar)[a,b]

| Reaction temperature (K) | 373 | 423 | 473 | 523 |
|---|---|---|---|---|
| Reaction time (h) | 19 | 39 | 95 | 160 |
| $C_4$ olefin conversion (%) | 1.5 | 5.1 | 14.0 | 70.3 |
| Apparent deactivation rate constant ($k_d$) | 3.77 | 0.70 | 0.38 | 0.15 |
| Butene distribution (%) | | | | |
| 1-butene | 7.3 | 11.1 | 11.0 | 6.6 |
| *cis*-2-butene | 29.1 | 30.5 | 28.8 | 15.0 |
| *trans*-2-butene | 63.5 | 55.9 | 50.8 | 25.3 |
| *iso*-butene | 0.1 | 2.5 | 9.4 | 53.0 |
| Olefin selectivity (%) | 62.1 | 81.9 | 88.6 | 76.6 |
| Olefin distribution (%) | | | | |
| C2-C4 | 0 | 0 | 24.5 | 36.0 |
| C5-C7 | 10.0 | 6.2 | 5.9 | 26.4 |
| C8 | 90.0 | 75.6 | 57.7 | 28.6 |
| C9-C11 | 0 | 0 | 3.5 | 5.8 |
| C12 | 0 | 0 | 5.5 | 2.7 |
| C13-C15 | 0 | 0 | 2.4 | 0.6 |
| C16 | 0 | 0 | 0.4 | 0 |
| C17-C19 | 0 | 0 | 0.2 | 0 |
| C20 | 0 | 0 | 0 | 0 |
| Paraffin selectivity (%) | 34.3 | 16.6 | 8.8 | 10.1 |
| Paraffin distribution (%) | | | | |
| C2-C4 | 100 | 100 | 78.2 | 51.3 |
| C5-C7 | 0 | 0 | 2.8 | 2.0 |
| C8 | 0 | 0 | 2.8 | 15.7 |
| C9-C11 | 0 | 0 | 5.1 | 15.6 |
| C12 | 0 | 0 | 2.7 | 5.1 |
| C13-C15 | 0 | 0 | 5.8 | 9.7 |
| C16 | 0 | 0 | 1.0 | 0.5 |
| C17-C19 | 0 | 0 | 1.6 | 0 |
| C20 | 0 | 0 | 0.1 | 0 |
| Aromatic selectivity (%) | 0 | 0 | 1.1 | 1.0 |
| Cycloalkane selectivity (%) | 0 | 0 | 1.9 | 3.2 |
| Carbon balance in gas phase (%) | 98.4 | 98.5 | 100.4 | 91.0 |

[a] Product distribution (%) = (the carbon moles in the product)/(the sum of carbon moles in the product group) × 100 %.

[b] Product selectivity (%) = (the carbon moles in the product)/(the carbon moles in the converted $C_4$ olefins) × 100 %.

Table 2.2 shows the butene distribution with respect to reaction temperatures. As reaction temperature increased, the 2-butene selectivity decreased, whereas the isobutene selectivity increased. 1-Butene undergoes isomerization to produce *cis*-2-butene and *trans*-2-butene [35]. Thermodynamic equilibrium between *cis*-2-butene, *trans*-2-butene, and 1-butene was rapidly reached at all temperatures studied. This is consistent with the work of Sels and co-workers [24]. *trans*-2-Butene then undergoes skeletal isomerization to produce isobutene [35]. The ratio of *trans*-2-butene to *cis*-2-butene decreased from 2.2 to 1.7 as reaction temperature increased. Isobutene production, which involves skeletal alteration, was not in equilibrium with *trans*-2-butene. This is consistent with the work of Lemos et al. [49].

The product selectivity was strongly dependent on reaction temperature as shown in Table 2.2. The carbon balances were 96.9–99.2%. The gaseous products were $C_2$–$C_8$ olefins and $C_1$–$C_5$ paraffins along with butene isomers. A small amount of liquid products which included $C_5$–$C_{19}$ olefins, $C_7$–$C_{20}$ paraffins, aromatics, and cycloalkanes was collected at temperatures above 473 K. A trace amount of $C_2$ olefin was detected with a selectivity of less than 0.5%. Most of the olefins (75.6–90.0%) were $C_8$ olefins at temperatures below 423 K. We did not detect any $C_9$–$C_{20}$ olefins at temperatures below 423 K. The $C_8$ olefin selectivity decreased with increasing reaction temperature, while the $C_3$ and $C_5$–$C_7$ olefin selectivity increased.

The only paraffin products observed at temperatures below 423 K were $C_4$ products. Boronat et al. found that hydride transfer of olefin feedstock is a primary reaction in the presence of Brønsted acid sites [50]. The $C_4$ paraffin selectivity decreased 2.2 times with increased temperature from 473 K to 523 K. The hydrogen transfer of oligomerization products led to an

increase of the $C_8$–$C_{20}$ paraffin, aromatic, and cycloalkane selectivity with increasing reaction temperature.

The deactivation rate constant was calculated according to Levenspiel's model [51,52] for independent deactivation assuming a second-order deactivation via the power-law equation as shown by Eq. (2.1). Second-order deactivation was found to be the best fit of our data for all conditions tested.

$$-r_d = -da / dt = k_d a^2 \quad [2.1]$$

In Eq. (1), rd is the deactivation rate, a is the fractional remaining activity at time t, and $k_d$ is the deactivation rate constant. The deactivation rate constant decreased 25 times as the reaction temperature increased from 373 K to 523 K, as shown in Table 2.2. This is probably because higher temperatures are needed to desorb the butene oligomer products from the catalyst pores.

**2.3.2. Effect of hexane solvent**

The influence of co-feeding hexane solvent with 1-butene at 62.7 bar was investigated as shown in Figures. 2.3 and 2.4 and Table 2.3. Hexane was determined to be inert at the low temperatures studied in this chapter due to the absence of hexane-derived products (i.e., hexene) and the lack of any observable change in the oligomer product distribution. The physical state of 1-butene/hexane mixtures can be calculated using dew point curves, where 90–100% of the 1-butene was in the vapor phase at the reaction conditions (see in Figure S2.2). Data were collected after 6 h time on stream during which no $C_4$ olefins were detected. After this transient period, the $C_4$ olefin conversion obtained at 8 h time on stream and 423 K increased almost 4 times with increasing the feed molar ratio of hexane to 1-butene from 3.1 to 18.1. The $C_4$ olefin conversion did not change as the hexane to 1-butene ratio increased from 18.1 to 34.3. The catalysts

deactivated after this transient period under all conditions. The deactivation rate constant was calculated during 8–26 h time on stream, as shown in Table 2.3. The deactivation rate constant increased with increasing hexane flow rate at 423 K. The deactivation rate constant increased with increasing total feed flow rate at the same hexane to 1-butene ratio at 423 K. An increase of WHSV also shifted the product distribution from heavier to lighter species. The H-FER lost 94% of its activity during 22 h time on stream at 0.18 $h^{-1}$ and 423 K with a hexane to butene feed molar ratio of 23 (see Figure S2.3). The deactivation rates were similar for all hexane to butene ratios at 523 K. The deactivation rate constants at 523 K were lower than those at 423 K.

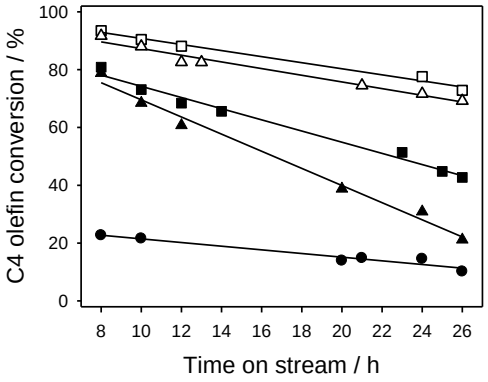


**Figure 2.3.** $C_4$ olefin conversion as a function of time-on-stream and hexane solvent co-feed at 423 K (filled) and 523 K (open). Reaction conditions: $P_{1\text{-butene}}$ = 1.2 bar, hexane to 1-butene molar ratio = 3.1 (●), $P_{1\text{-butene}}$ = 0.9 bar, hexane to 1-butene molar ratio = 18.1 (■,□), $P_{1\text{-butene}}$ = 0.8 bar, hexane to 1-butene molar ratio = 34.3 (▲,△). $WHSV_{1\text{-butene}}$ = 0.03 $h^{-1}$; $P_{total}$ = 62.7 bar.

The product distribution was a function of $C_4$ olefin conversion as shown in Figure 2.4. The olefin selectivity decreased and the paraffin selectivity increased with increasing $C_4$ olefin conversion. The aromatics and cycloalkanes selectivity was low (less than 2%) at 423 K. The aromatic and cycloalkane selectivity increased with increasing reaction temperature. At 523 K,

the selectivity toward aromatics and cycloalkanes increased with $C_4$ olefin conversion. The aromatic and cycloalkane selectivity decreased with increasing hexane flow rate at 523 K.

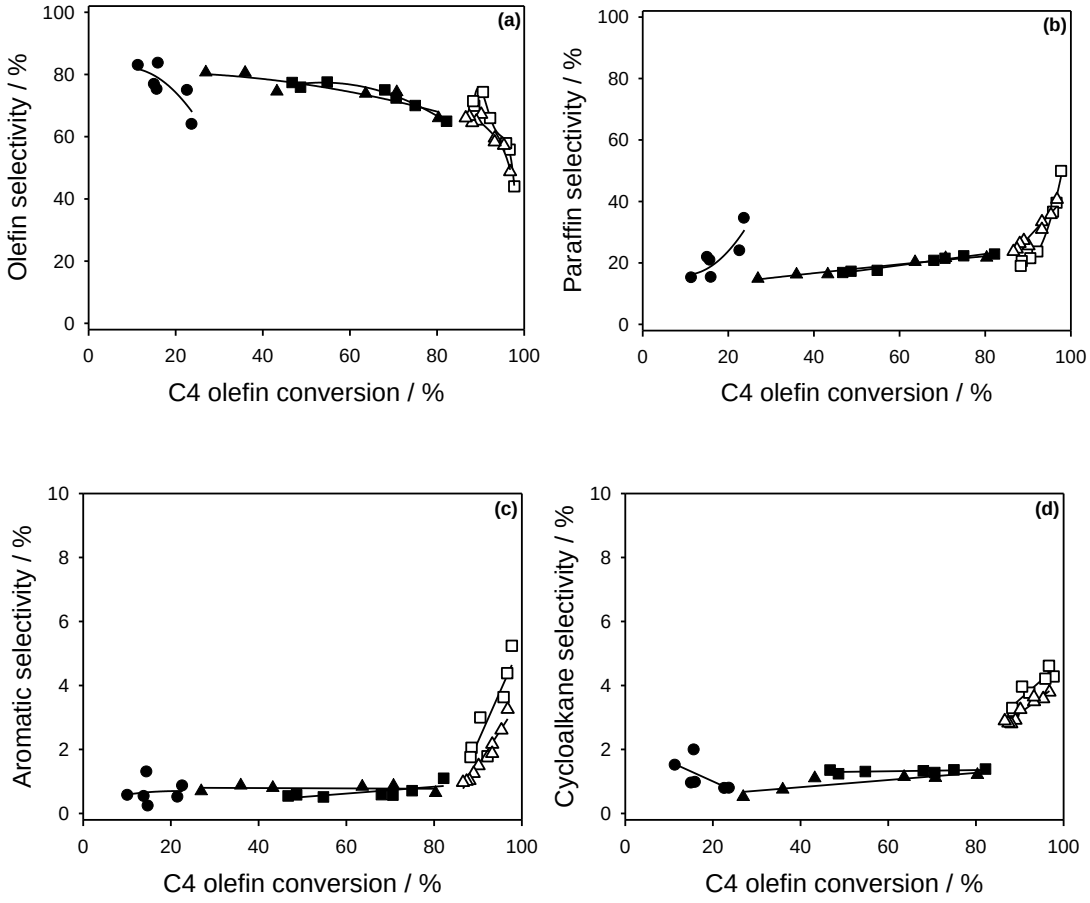


**Figure 2.4.** Product selectivities for (a) olefins, (b) paraffins, (c) aromatics, and (d) cycloalkanes as a function of $C_4$ olefin conversion at 423 K (filled) and 523 K (open). Reaction condition: $P_{1\text{-butene}}$ = 1.2 bar, hexane to 1-butene = 3.1 (●), $P_{1\text{-butene}}$ = 0.9 bar, hexane to 1-butene = 18.1 (■,□), $P_{1\text{-butene}}$ = 0.8 bar, hexane to 1-butene = 34.3 (▲,△).$WHSV_{1\text{-butene}}$ = 0.03 $h^{-1}$; $P_{total}$ = 62.7 bar.

The olefin and paraffin selectivity with different feed hexane to 1-butene ratios are shown in Table 2.3 and Figs. S2.4 and S2.5. In Table 2.3, we report the data at different time on stream

**Table 2.3.** Effect of hexane co-solvent on 1-butene oligomerization at high pressure (62.7 bar)[a,b]

| Reaction temperature (K) | 423 | 423 | 423 | 423 | 523 | 523 |
|---|---|---|---|---|---|---|
| Feed hexane to 1-butene ratio | 3.1 | 34.3 | 18.1 | 34.3 | 18.1 | 34.3 |
| Hexane physical state | Vapor | Liquid | Liquid | Liquid | Vapor | Vapor |
| $WHSV_{1\text{-butene}}$ ($h^{-1}$) | 0.03 | 0.18 | 0.03 | 0.03 | 0.03 | 0.03 |
| $P_{1\text{-butene}}$ (bar) | 1.2 | 0.8 | 0.9 | 0.8 | 0.9 | 0.8 |
| $P_{hexane}$ (bar) | 3.6 | 23.5 | 15.5 | 23.5 | 15.5 | 23.5 |
| Reaction time (h) | 20 | 12 | 8 | 8 | 24 | 21 |
| $C_4$ olefin conversion (%) | 14.0 | 15.4 | 80.8 | 78.7 | 92.1 | 90.1 |
| Apparent deactivation rate constant ($k_d$) | 0.57 | 1.30 | 0.52 | 1.01 | 0.20 | 0.23 |
| Butene distribution (%) | | | | | | |
| 1-butene | 13.1 | 13.3 | 12.5 | 12.3 | 7.4 | 8.1 |
| *cis*-2-butene | 27.6 | 27.9 | 26.0 | 26.0 | 9.9 | 11.1 |
| *trans*-2-butene | 57.9 | 58.1 | 54.6 | 54.4 | 17.6 | 19.5 |
| *iso*-butene | 1.4 | 0.7 | 7.0 | 7.3 | 65.2 | 61.3 |
| Olefin selectivity (%) | 74.4 | 83.1 | 64.4 | 65.3 | 65.3 | 64.5 |
| Olefin distribution (%) | | | | | | |
| C2-C3 | 0.8 | 0.0 | 1.6 | 0.6 | 13.3 | 15.2 |
| C5-C7 | 5.0 | 5.2 | 3.0 | 4.9 | 27.4 | 29.7 |
| C8 | 78.9 | 76.2 | 17.7 | 26.8 | 34.9 | 28.7 |
| C9-C11 | 4.6 | 4.9 | 14.0 | 15.9 | 15.2 | 18.8 |
| C12 | 10.6 | 13.7 | 13.8 | 19.3 | 7.5 | 6.1 |
| C13-C15 | 0.1 | 0.0 | 12.4 | 10.9 | 1.8 | 1.4 |
| C16 | 0.0 | 0.0 | 19.7 | 14.7 | 0.0 | 0.0 |
| C17-C19 | 0.0 | 0.0 | 0.6 | 1.4 | 0.0 | 0.0 |
| C20 | 0.0 | 0.0 | 17.2 | 5.5 | 0.0 | 0.0 |
| Paraffin selectivity (%) | 23.6 | 12.8 | 23.3 | 22.2 | 22.8 | 24.1 |
| Paraffin distribution (%) | | | | | | |
| C2-C4 | 41.8 | 67.2 | 11.6 | 30.8 | 54.0 | 54.5 |
| C5-C7 | 2.5 | 7.8 | 13.7 | 5.4 | 19.1 | 19.3 |
| C8 | 34.6 | 1.6 | 21.5 | 19.0 | 16.2 | 14.1 |
| C9-C11 | 16.5 | 22.7 | 33.9 | 33.5 | 8.8 | 10.3 |
| C12 | 4.2 | 0.0 | 11.2 | 6.3 | 1.5 | 1.0 |
| C13-C15 | 0.4 | 0.8 | 8.2 | 5.0 | 0.4 | 0.7 |
| C16 | 0.0 | 0.0 | 0.0 | 0.0 | 0.0 | 0.0 |
| C17-C19 | 0.0 | 0.0 | 0.0 | 0.0 | 0.0 | 0.0 |
| C20 | 0.0 | 0.0 | 0.0 | 0.0 | 0.0 | 0.0 |
| Aromatic selectivity (%) | 0.5 | 2.2 | 1.1 | 0.7 | 1.7 | 1.5 |
| Cycloalkane selectivity (%) | 1.0 | 0.3 | 1.4 | 1.2 | 3.8 | 3.2 |
| Carbon balance (%) | 99.0 | 98.5 | 92.5 | 91.6 | 95.4 | 94.4 |

[a] Product distribution (%) = (the carbon moles in the product)/(the sum of carbon moles in the product group) × 100 %.

[b] Product selectivity (%) = (the carbon moles in the product)/(the carbon moles in the converted $C_4$ olefins) × 100 %.

to compare the product selectivities at similar $C_4$ olefin conversions. The olefin and paraffin distributions were similar to those without co-feeding a hexane solvent over reaction temperatures (423–523 K) (Tables 2.2 and 2.3). The $C_5$–$C_7$ olefin selectivity increased with increasing reaction temperature, while the $C_{12}$–$C_{20}$ olefin selectivity decreased with increasing temperature. Similarly, the $C_2$–$C_7$ paraffin selectivity increased with increasing reaction temperature, while the $C_9$–$C_{11}$ paraffin selectivity decreased with increasing reaction temperature.

The feed hexane flow rate changed the olefin and paraffin selectivity at similar $C_4$ olefin conversions, as shown in Table 2.3. At 423 K, the $C_8$ and $C_{12}$ olefin selectivity increased while the $C_{16}$ and $C_{20}$ olefin selectivity decreased with increasing hexane to 1-butene ratio. At 523 K, the $C_5$–$C_7$ and $C_9$–$C_{11}$ olefin selectivity increased with increasing hexane to 1-butene ratio. An increase of total feed flow rate at the same hexane to 1-butene ratio also shifted product distribution from heavier to lighter species. The $C_8$ paraffin selectivity decreased from 34.6% to 1.6% with increasing hexane to 1-butene ratio from 3.1 to 34.3 at similar $C_4$ olefin conversions at 423 K. The $C_8$ paraffins were mainly composed of 4-methyl heptane, 3,3-dimethyl hexane, and 3,4-dimethyl hexane.

The TGA of the used catalysts under oxygen showed that different types of coke were deposited on the catalyst during the reaction, as shown in Figure 2.5. For comparison, TGA under nitrogen of the used catalysts was also examined, as shown in Figure S2.6. The derivative thermogravimetry (DTG) curves showed three peaks at 523–539 K, 613 K, and 769 K. A peak below 400 K was most likely due to physisorbed water. Control experiments showed hexane adsorbed on H-FER was removed at 352 K. The carbon species detected at 523–539 K under oxygen and nitrogen are similar for the catalysts tested at 423 K suggesting that the species

characteristic of these peaks can be thermally desorbed (see Figure 2.5 and Figure S2.6). We did not detect a peak in this temperature region for the used catalyst operated at 523 K when placed under oxygen. The peaks above 600 K under oxygen were most likely due to aromatic molecules based on FT-IR of the ZSM-5 catalysts after the $C_4$ olefin oligomerization at 493 K [23,24]. This peak above 600 K was larger for the spent catalyst run at 523 K than the spent catalysts run at 423 K. These results indicate that deposition of heavy hydrocarbons (peaks for TGA under oxygen at 523–539 K) is responsible for catalyst deactivation at 423 K.

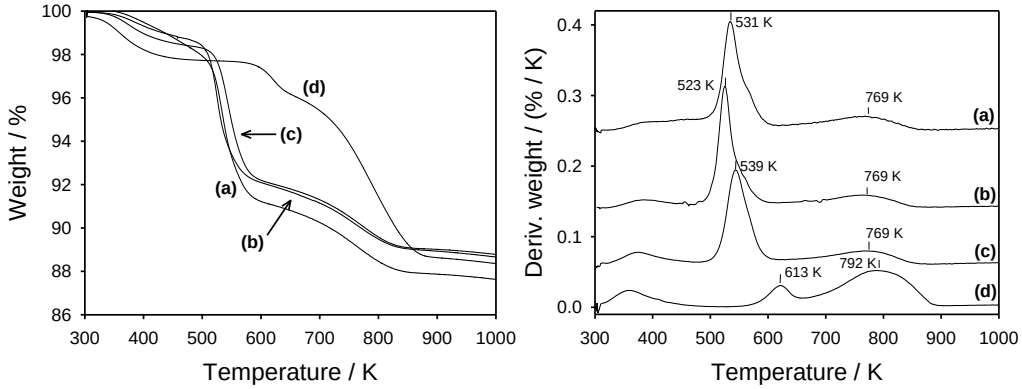


**Figure 2.5.** Thermogravimetric Analysis (TGA) under oxygen of spent H-FER catalysts; (a) 423 K, feed hexane to 1-butene molar ratio = 3.1, $WHSV_{1\text{-butene}}$ = 0.03 $h^{-1}$; $P_{1\text{-butene}}$ = 1.2 bar, $P_{total}$ = 62.7 bar, (b) 423 K, feed hexane to 1-butene molar ratio = 18.1, $WHSV_{1\text{-butene}}$ = 0.03 $h^{-1}$; $P_{1\text{-butene}}$ = 0.9 bar, $P_{total}$ = 62.7 bar, (c) 423 K, feed hexane to 1-butene molar ratio = 34.3, $WHSV_{1\text{-butene}}$ = 0.03 $h^{-1}$; $P_{1\text{-butene}}$ = 0.8 bar, $P_{total}$ = 62.7 bar, and (d) 523 K, 2.0 mol% 1-butene in helium, $WHSV_{1\text{-butene}}$ = 0.03 $h^{-1}$; $P_{1\text{-butene}}$ = 0.14 bar. $P_{total}$ = 6.9 bar.

The amount of carbon species present on the catalysts tested at 423 K, detected in the TGA under oxygen from 523 to 538 K, decreased with increasing hexane to 1-butene ratio. Hard coke is revealed through a difference between the amount of carbon lost under oxygen and nitrogen. The hard coke is expected to be composed of polynuclear aromatics containing four aromatics rings with methyl substituents [34,36,40,41]. Only sixty percent of the total carbon species was

thermally desorbed from the catalyst tested at 523 K under nitrogen flow revealing the presence of hard coke. Andy et al. studied molecular mechanics calculations of coke molecules formed during n-butene conversion at 623 K over H-FER and showed that hard coke was located in one or two intersections of 10- and 8-MR channels along the 10-MR channels [37]. The surface acid sites can be fully regenerated by treating the spent catalyst at 873 K under 10% oxygen (see Figure S2.7). Characterization revealed that all the catalysts lost most of their surface area and micropore volume under all reaction conditions, as shown in Table 2.1. The carbon content of the used catalysts was between 9.5 and 11.4 wt%. It has been reported that ca. 8 wt.% carbon species is enough to fully deactivate H-FER in the gas-phase butane isomerization reaction [36]

### 2.3.3. Effect of 1-butene partial pressure

The effect of butene partial pressure at 423 K is shown in Figs. 3.6–8. The inlet partial pressure of 1-butene was varied by using helium as a balance. The total pressure was held constant at 62.7 bar. The critical temperature and pressure of 1-butene are 419.6 K and 40.2 bar [53]. Thus, we are above the critical temperature and above the critical pressure at some of the conditions in Figure 2.6. The $C_4$ olefin conversion increased from 1.2 to 49.2 with increasing 1-butene partial pressure from 14.2 to 62.7 bar. At 14.2 bar, the catalyst deactivated rapidly during the first 10 h on stream. The rate of deactivation decreased with increasing 1-butene partial pressure.

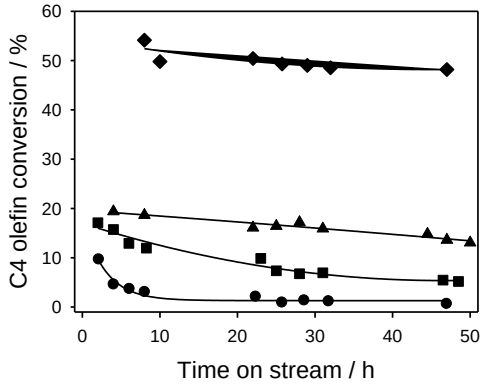


**Figure 2.6.** $C_4$ olefin conversion as a function of time on stream: Effect of 1-butene partial pressure; 14.2 bar (●), 32.2 bar (■), 42.9 bar (▲), 62.7 bar (◆). Reaction condition: $WHSV_{1\text{-butene}}$ = 3.17 $h^{-1}$; $P_{total}$ = 62.7 bar, T = 423 K.

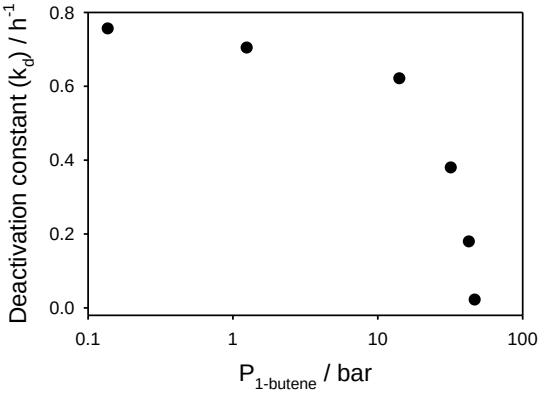


**Figure 2.7**. Apparent deactivation rate constants ($k_d$) for $C_4$ olefin oligomerization as a function of 1-butene partial pressure. Reaction condition: $P_{total}$ = 62.7 bar, T = 423 K.

The deactivation rate constant was inversely proportional to 1-butene (and thus total $C_4$) partial pressure as shown in Figure 2.7. For example, assuming second-order deactivation, the deactivation rate constant decreased 36.3 times (from 0.75 $h^{-1}$ to 0.02 $h^{-1}$) as the 1-butene partial pressure increased from 0.14 bar to 62.7 bar. Decreasing the temperature from 423 K to 373 K, where 1-butene is in the liquid phase, caused a 3.8-fold increase in the rate of deactivation, as shown in Figure 2.9. These results show that the transition from the butene subcritical to

supercritical state either removes coke or inhibits its formation. These results are consistent with those of Fan et al. [46] who observed that 90% of the initial activity of a spent H-ZSM-5 catalyst that had been used for ethylene oligomerization at 573 K and 55 bar was restored by treatment in supercritical n-pentane for 3 h.

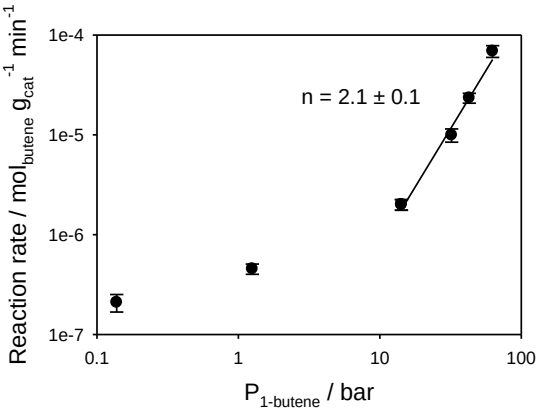


**Figure 2.8**. $C_4$ olefin reaction rate as a function of 1-butene partial pressure. Reaction condition: $P_{total}$ = 62.7 bar, T = 423 K

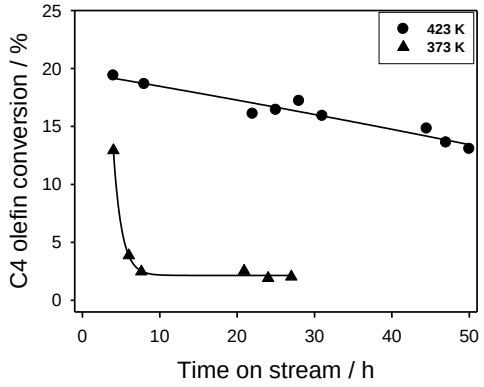


**Figure 2.9.** $C_4$ olefin conversion as a function of time-on-stream and temperature. Reaction condition: $P_{1\text{-butene}}$ = 42.9 bar, $WHSV_{1\text{-butene}}$ = 0.03 $h^{-1}$; $P_{total}$ = 62.7 bar.

The rate of butene conversion was second order with respect to 1-butene partial pressure in the near-critical region at 423 K as shown in Figure 2.8. This is consistent with the work of Gee and Williams who reported that the dimerization of linear olefins in the range of $C_8$ to $C_{18}$ was

second order in olefin [54]. For butene, partial pressure of 0.14–1.25 bar catalyst deactivation made it difficult to determine the exact order in butene. We can make a rough estimate of the reaction order to be approximately 0.4 with respect to butene (from the data Figure 2.8) assuming that we have made correct measurements of catalyst activity on the deactivating catalyst. As demonstrated in this section, one way of reducing the deactivation of the zeolite catalyst is to operate at a relatively low temperature (423 K) and at near-supercritical, which are the conditions slightly above or below the critical point, butene conditions. Under these conditions, butene has the appropriate transport properties to effectively extract heavy hydrocarbons from the catalyst pores [55,56]**.**

**2.3.4. Effect of space velocity**

The effect of weight hourly space velocity (WHSV) on 1-butene oligomerization at 423 K and 62.7 bar (supercritical conditions) is shown in Figure 2.10 and Tables 2.4 and 2.5. At least three samples were collected for each condition at regular intervals to ensure steady state was reached. The $C_4$ olefin conversion increased with decreasing space velocity. As the WHSV increased from 0.18 to 3.17 $h^{-1}$, the olefin selectivity increased from 76.8% to 92.4%. An olefin selectivity >90% was maintained at WHSV of 9.5 and 49.7 $h^{-1}$. The paraffin selectivity markedly decreased from 12.6% to 4.7% with increasing the WHSV from 0.18 to 1.06 $h^{-1}$ and continued to decrease with increasing WHSV reaching a minimum of 0.7% at 49.7 $h^{-1}$. Only trace quantities of aromatics and cycloalkanes were detected at a space velocity of 0.18 $h^{-1}$, but their selectivity increased to 2.4% and 1.7% as the WHSV increased to 50 $h^{-1}$.

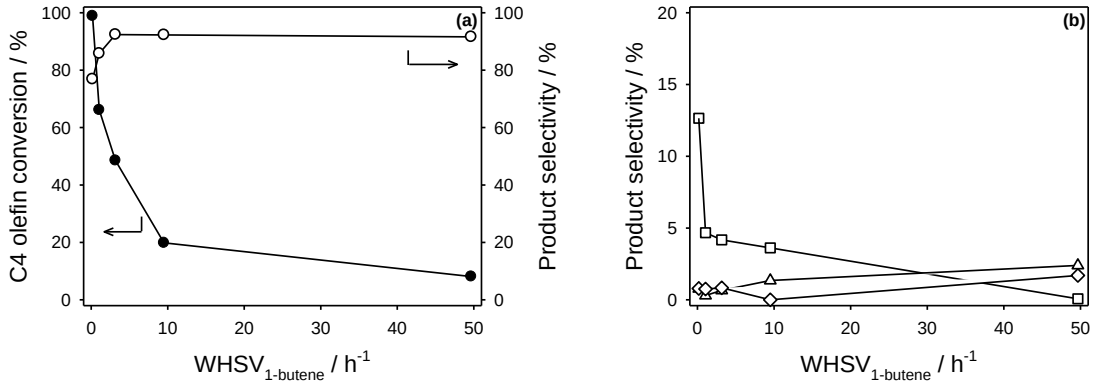


**Figure 2.10.** (a) $C_4$ olefin conversion (●) and olefin selectivity (○) as a function of weight hourly space velocity (WHSV). (b) Paraffins (□), aromatics (△), and cycloalkanes selectivity (◇) as a function of WHSV. Reaction condition: $P_{total}$ = 62.7 bar, $P_{1\text{-butene}}$ = 62.7 bar, T = 423 K.

The product selectivities as a function of WHSV are shown in Table 2.4. Only trace quantities of isobutene were detected at 98.9% $C_4$ olefin conversion. We did not detect $C_2$–$C_4$ olefins and $C_2$–$C_4$ paraffins under these reaction conditions. The $C_5$–$C_7$ olefin selectivity was 1.1–2.0%, indicating that cracking of $C_8$ olefins is minimized under supercritical conditions. At a space velocity of 49.7 $h^{-1}$, $C_8$ olefins were the predominant olefin product, representing 88.8% of total olefin production. As space velocity decreased from 49.7 $h^{-1}$ to 0.18 $h^{-1}$, the $C_8$ olefin selectivity decreased from 88.8% to 15.1%, whereas the $C_{12}$, $C_{16}$, and $C_{20}$ olefin selectivity increased from 9.0% to 59.6%. Similarly, the selectivity toward $C_9$–$C_{11}$, $C_{13}$–$C_{15}$, and $C_{17}$–$C_{19}$ olefins increased from 0.3% to 24.1% with decreasing WHSV. Similar patterns were also observed with $C_5$–$C_{15}$ paraffins. These results reveal a partial and increasing contribution of selective oligomerization–cracking–realkylation by H-FER with decreasing WHSV. Iglesia reported that high molecular weight olefins are more susceptible to cracking reactions than light olefins [57,58].

Figure 2.11 shows a semilog plot that represents the oligomerization and oligomerization–cracking–realkylation products in Table 2.4. These products followed the Schulz–Flory chain growth model [59–61], as shown in Eq. (2.2).

$$\frac{W_n}{n} = \alpha^{n-1}(1-\alpha)^2 \tag{2.2}$$

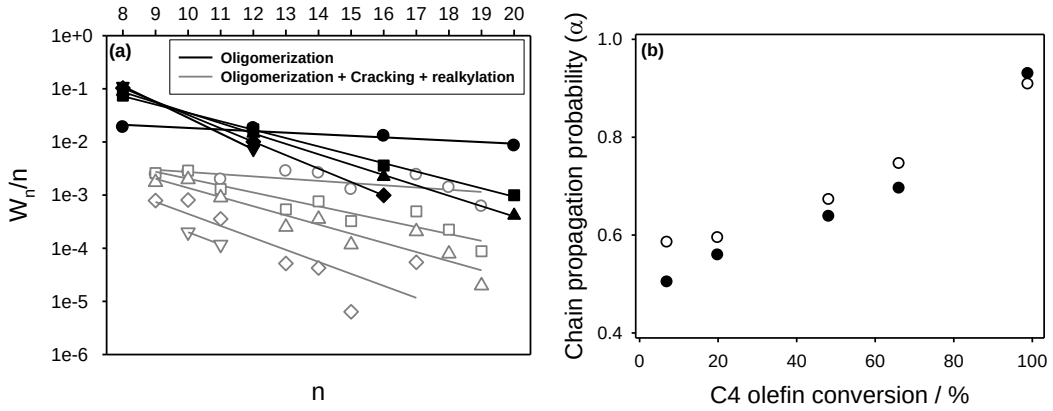


**Figure 2.11.** (a) Olefin molecular weight distributions at a $WHSV_{1\text{-butene}}$ of 0.18 $h^{-1}$ (●, ○), 1.06 $h^{-1}$ (■, □), 3.17 $h^{-1}$ (▲, △), 9.51 $h^{-1}$ (◆, ◇), and 49.7 $h^{-1}$ (▼, ▽) for oligomerization products ($C_8$, $C_{12}$, $C_{16}$, and $C_{20}$) (open) and oligomerization-cracking-realkylation products ($C_9$-$C_{11}$, $C_{13}$-$C_{15}$, $C_{17}$-$C_{19}$) (filled). (b) chain propagation probability (α) for oligomerization products ($C_8$, $C_{12}$, $C_{16}$, and $C_{20}$) (●) and oligomerization-cracking-realkylation products (C9-$C_{11}$, $C_{13}$-$C_{15}$, and $C_{17}$-$C_{19}$) (○) as a function of $C_4$ olefin conversion. Reaction condition: $P_{1\text{-butene}}$ = 62.7 bar, $P_{total}$ = 62.7 bar, T = 423 K.

In Eq. (2.2), n is the hydrocarbon chain length, $W_n$ is the weight fraction of hydrocarbon products of length n, and a is the chain growth probability. In this study, we have applied the Schulz–Flory chain growth model to the olefin products. Schulz–Flory distribution is commonly employed to model polymer and polyolefin chain distribution [62–64]. The oligomerization ($C_8$, $C_{12}$, $C_{16}$, $C_{20}$ olefins) and oligomerization–cracking–realkylation ($C_9$–$C_{11}$, $C_{13}$– $C_{15}$, and $C_{17}$–$C_{19}$ olefins) products also followed the Schulz–Flory model as shown in Figure 2.11. Oligomerization–cracking products such as $C_5$–$C_7$ olefins did not follow Schulz–Flory distribution and are not

reported. The chain growth probability increased from 0.50 to 0.93 with increasing the $C_4$ olefin conversion from 8.1% to 98.9%.

The amount of branching in the olefins was a function of the butene conversion as shown in Figure 2.12. Only trace amounts of straight-chain alkenes were produced irrespective of butene conversion. Over 80% of the oligomer products were di-branched olefins at conversions less than 20%. The amount of branching increased as the conversion increased. We did not individually identify each of the $C_{12}$–$C_{20}$ olefin isomers through GCxGC–MS due to lack of standard chemicals for these olefins. As the di-branched olefin selectivity decreased, the selectivity to highly branched olefins increased. The other branched olefins included >trimethyl- and methyl-ethyl-species. The mono-branched olefin selectivity decreased while higher branched olefin selectivity increased with increasing $C_4$ olefin conversion. The direct correlation between olefin branching and $C_4$ olefin conversion is consistent with a carbocation-based mechanism of oligomerization.

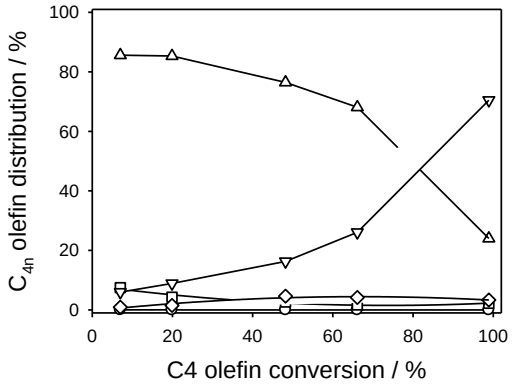


**Figure 2.12.** $C_{4n}$ (n=2-6) olefin distribution of linear- (○), mono-branched- (□), di-branched- (△), tri-branched- (◇), and greater than tri-branched-olefins (▽) a function of $C_4$ olefin conversion. Reaction condition: $P_{total}$ = 62.7 bar, $P_{1\text{-butene}}$ = 62.7 bar, T = 423 K.

**Table 2.4.** 1-Butene oligomerization at supercritical 1-butene conditions as a function of weight hourly space velocity (WHSV) (Reaction condition: $P_{total}$ = 62.7 bar, $P_{1\text{-butene}}$ = 62.7 bar, T = 423 K)[a,b]

| WHSV ($h^{-1}$) | 0.18 | 1.06 | 3.17 | 9.51 | 49.7 |
|---|---|---|---|---|---|
| Reaction time (h) | 51 | 50 | 47 | 4 | 1 |
| $C_4$ olefin conversion (%) | 98.9 | 66.1 | 48.5 | 19.3 | 8.1 |
| Butene distribution (%) | | | | | |
| 1-butene | 11.7 | 12.9 | 12.8 | 13.3 | 15.5 |
| *cis*-2-butene | 27.2 | 28.5 | 28.4 | 28.4 | 28.2 |
| *trans*-2-butene | 55.9 | 58.5 | 58.8 | 58.3 | 56.2 |
| *iso*-butene | 5.1 | 0 | 0 | 0 | 0 |
| Olefin selectivity (%) | 76.8 | 85.8 | 92.4 | 92.3 | 91.6 |
| Olefin distribution (%) | | | | | |
| C2-C3 | 0.0 | 0.0 | 0.0 | 0.0 | 0.0 |
| C5-C7 | 1.1 | 1.8 | 2.0 | 1.6 | 1.9 |
| C8 | 15.1 | 59.4 | 69.2 | 82.6 | 88.8 |
| C9-C11 | 7.1 | 6.6 | 4.9 | 1.9 | 0.3 |
| C12 | 21.8 | 20.7 | 17.7 | 12.0 | 8.7 |
| C13-C15 | 9.2 | 2.3 | 1.0 | 0.1 | 0.0 |
| C16 | 20.8 | 5.7 | 3.8 | 1.6 | 0.0 |
| C17-C19 | 7.8 | 1.4 | 0.6 | 0.1 | 0.0 |
| C20 | 17.0 | 2.0 | 0.8 | 0.1 | 0.3 |
| Paraffin selectivity (%) | 12.6 | 4.7 | 4.2 | 3.6 | 0.1 |
| Paraffin distribution (%) | | | | | |
| C2-C4 | 0.0 | 0.0 | 0.0 | 0.0 | 0.0 |
| C5-C7 | 6.7 | 4.5 | 5.6 | 4.7 | 0.0 |
| C8 | 53.8 | 76.0 | 73.3 | 60.7 | 100 |
| C9-C11 | 31.3 | 16.7 | 17.4 | 29.3 | 0.0 |
| C12 | 4.6 | 1.5 | 2.6 | 4.9 | 0.0 |
| C13-C15 | 3.6 | 1.3 | 1.2 | 0.3 | 0.0 |
| C16 | 0.0 | 0.0 | 0.0 | 0.0 | 0.0 |
| C17-C19 | 0.0 | 0.0 | 0.0 | 0.0 | 0.0 |
| C20 | 0.0 | 0.0 | 0.0 | 0.0 | 0.0 |
| Aromatic selectivity (%) | 0.8 | 0.3 | 0.7 | 1.3 | 2.4 |
| Cycloalkane selectivity (%) | 0.8 | 0.8 | 0.8 | 0 | 1.7 |
| Carbon balance (%) | 91.2 | 94.4 | 99.1 | 99.5 | 99.7 |

[a] Product distribution (%) = (the carbon moles in the product)/(the sum of carbon moles in the product group) × 100 %.

[b] Product selectivity (%) = (the carbon moles in the product)/(the carbon moles in the converted $C_4$ olefins) × 100 %.

The distribution of $C_8$ olefin isomers is summarized in Table 2.5. The $C_8$ olefin products included 91.9–94.7% dimethyl hexenes with $C_4$ olefin conversions. The methyl-heptene selectivity decreased from 8.1% to 2.7%, while the trimethyl-pentene selectivity increased from 0.1% to 2.6% with increasing $C_4$ olefin conversion. A trace of linear octenes was detected with a selectivity of less than 0.1%. Near equilibrium of the $C_8$ double-bond isomers was achieved, as shown in Figure S2.8.

Figure 2.13 shows the major reaction pathways for 1-butene oligomerization. This pathway involves acid-catalyzed reactions: (1) oligomerization, (2) (skeletal) isomerization, (3) hydrogen transfer, (4) cracking, and (5) alkylation [65]. According to the assumption that the heats of adsorption for olefin adsorption in zeolites vary linearly with carbon number [66], the products with larger carbon numbers are more likely to be re-adsorbed and undergo secondary reactions such as hydrogen transfer, cracking, and isomerization [56]. 1-Butene underwent double bond and skeletal isomerization to form *trans*-or *cis*-2-butene and isobutene, respectively. Based on Markovnikov's rule [39], reactions involving a primary carbocation were unlikely to take place; thus, the amount of linear octenes and 3-methyl-heptenes were minimal. Most of the products were formed through secondary carbocations. At a low $C_4$ olefin conversion, 3,4-dimethyl hexenes and 2,3-dimethyl hexenes were predominant products in the mixture of $C_8$ olefin products (Table 5). The dimerization products then underwent further methyl and hydride shift, thus forming additional $C_8$ isomers, which were in equilibrium at 423 K (Figure S2.9). As $C_4$ olefin conversion increased, the 3,4-dimethyl hexene selectivity decreased, whereas the selectivity toward 2,4-dimethyl hexenes and 2,5-dimethyl hexenes increased. The 2,3-dimethyl hexene selectivity increased a little with $C_4$ olefin conversions. The selectivity data illustrate that the formation of

2,3-dimethyl hexenes is favored over the 2,4 and 2,5 dimethyl hexene isomers during a skeletal alteration of 3,4-dimethyl hexenes, even at low $C_4$ butene conversions. Most of 2,2-dimethyl hexenes were probably formed from the initial skeletal isomerization of 2-butene to isobutene followed by addition of 1-butene to isobutene since the equilibrium composition of those compounds was significantly low for 2-butene conversion (see in Figure S2.9). The combination of isobutene and 2-butene yielded 2,4,4-trimethyl-pentene and 2,3,4-trimethyl-pentene which were observed in low selectivities.

**Table 2.5.** Distribution of octenes at supercritical 1-butene conditions as a function of WHSV. (Reaction condition: $P_{total}$ = 62.7 bar, $P_{1\text{-butene}}$ = 62.7 bar, T = 423 K)[a]

| WHSV ($h^{-1}$) | 0.18 | 1.06 | 3.17 | 9.51 | 49.7 |
|---|---|---|---|---|---|
| C8 olefin distribution (%) | | | | | |
| 2-methyl-1-heptene | 0.0 | 0.0 | 0.3 | 0.0 | 1.9 |
| 2-methyl-3-heptene | 0.9 | 0.0 | 0.5 | 0.8 | 1.4 |
| 3-methyl-2-heptene | 0.9 | 0.6 | 0.9 | 1.6 | 2.8 |
| 3-methyl-3-heptene | 0.9 | 0.8 | 0.8 | 1.0 | 2.0 |
| 5-methyl-2-heptene | 0.0 | 0.0 | 0.2 | 1.0 | 0.0 |
| 2,2-dimethyl-3-hexene | 3.5 | 4.9 | 3.8 | 1.8 | 1.1 |
| 2,3-dimethyl-2-hexene | 19.3 | 13.7 | 11.9 | 10.5 | 10.5 |
| 2,3-dimethyl-3-hexene | 7.0 | 12.7 | 13.9 | 13.8 | 12.5 |
| 2,4-dimethyl-2-hexene | 19.3 | 6.7 | 5.1 | 5.4 | 5.3 |
| 2,5-dimethyl-2-hexene | 19.3 | 7.5 | 6.4 | 5.5 | 4.6 |
| 2,5-dimethyl-3-hexene | 0.9 | 0.4 | 0.2 | 0.1 | 0.0 |
| 3,4-dimethyl-2-hexene | 14.9 | 37.3 | 41.2 | 43.7 | 42.8 |
| 3,4-dimethy-3-hexene | 7.0 | 13.3 | 13.6 | 14.4 | 15.1 |
| 5,5-dimethyl-2-hexene | 3.5 | 0.6 | 0.2 | 0.0 | 0.0 |
| 2,4,4-trimethyl-1-pentene | 0.0 | 0.0 | 0.5 | 0.0 | 0.1 |
| 2,3,4-trimethyl-2-pentene | 2.6 | 1.6 | 0.6 | 0.3 | 0.0 |

[a] Product distribution (%) = (the carbon moles in the product)/(the sum of carbon moles in the product group) × 100 %.

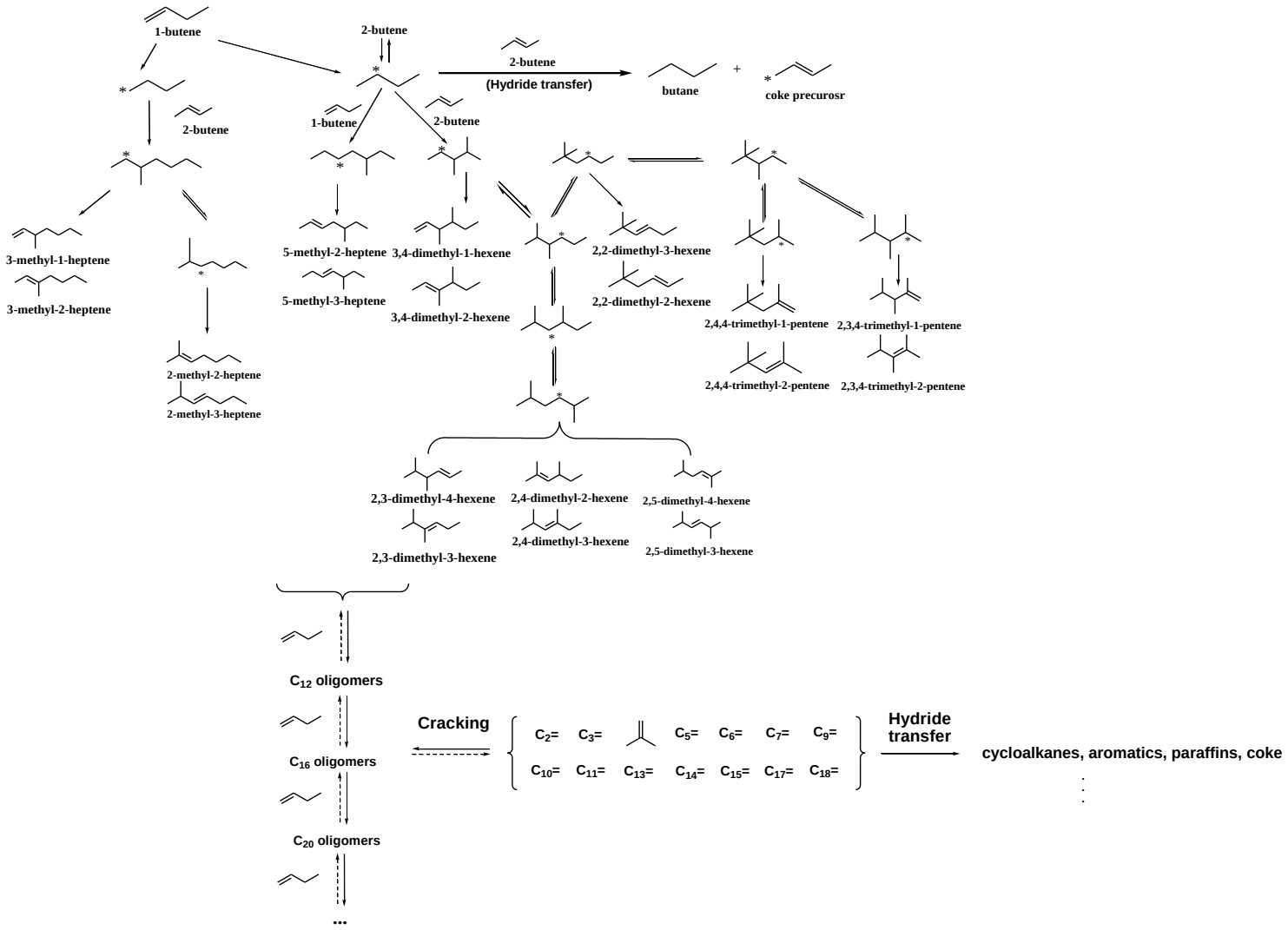


**Figure 2.13.** Major reaction pathways for oligomerization of 1-butene.

## 2.4 Conclusions

1-Butene was oligomerized over H-ferrierite at low temperatures (373–523 K). 1-Butene was in equilibrium with *trans*- and *cis*-2-butene under all reaction conditions. During the reaction, the catalyst deactivated due to the deposition of heavier hydrocarbons inside micropores. The deactivation rate was a function of temperature, solvent co-feeds, and butene partial pressure. The deactivation rate constant decreased 25 times with increasing temperature (373–523 K) at low butene partial pressure (0.14 bar). Twenty-four percent of the acid sites were lost after reaction at 523 K, while only 1.1–9.2% of acid sites were lost at 423 K. The $C_8$ olefin selectivity was maximized at low temperatures (below 473 K). At temperatures above 473 K, cracking and hydride transfer reactions occurred increasing the selectivity to paraffins, aromatics, and non-$C_4$ multiple olefins. Co-feeding of hexane with 1-butene slightly improved the catalyst stability and shifted the product selectivity from heavier to lighter species. Higher hexane to 1-butene ratios also decreased the paraffin selectivity.

The catalytic activity was proportional to 1-butene partial pressure with an apparent reaction order of 2.1 ± 0.1 at pressures from 14.2–62.7 bar. The deactivation rate constant decreased 36.3 times with increasing 1-butene partial pressure (0.14–62.7 bar). During the reaction at supercritical 1-butene conditions (62.7 bar and 423 K), the products followed a Schulz–Flory chain growth distribution. The chain growth probability decreased with increasing $C_4$ olefin conversion. Butenes initially underwent dimerization to produce 3,4-dimethyl-2-hexene and 3-methyl-heptene. Then, both $C_8$ olefins underwent a series of skeletal isomerizations (methyl shifting). The skeletal isomerization products were in equilibrium at 423 K. The isomerization of C=C bonds was in

equilibrium for $C_4$ olefins and $C_8$ olefins. Most of heavier olefins ($>C_{12}$) were highly branched (>trimethyl- and methyl-ethyl-species).

## 2.5 Supplementary Information

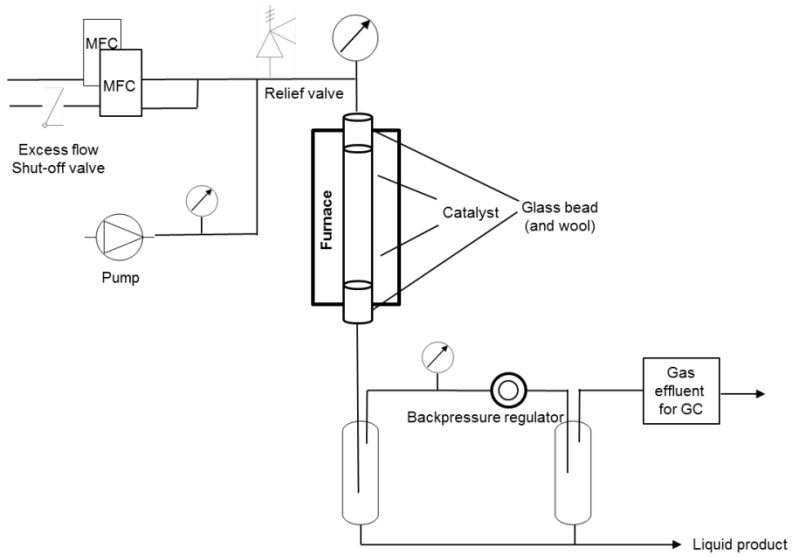


**Figure S2.1.** Schematic of fixed-bed reactor system.

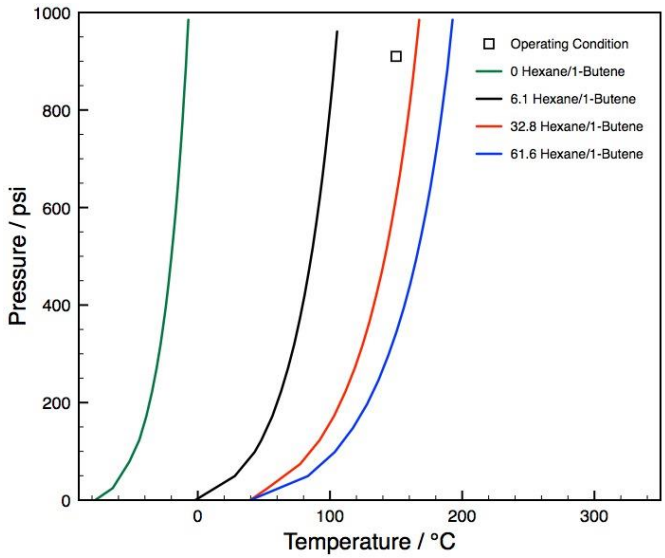


**Figure S2.2.** Dew point curve for various hexane to 1-butene feed ratios**.**

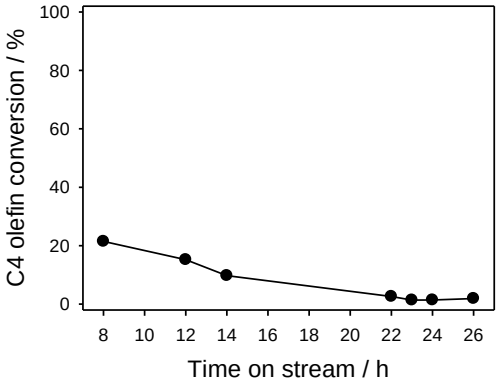


**Figure S2.3.** Butene conversion for oligomerization of butene with hexane as a function of time-on-stream at 423 K. Reaction condition: $P_{1\text{-butene}}$ = 0.9 bar, feed hexane to 1-butene = 34.3. $WHSV_{1\text{-butene}}$ = 0.18 $h^{-1}$; $P_{total}$ = 62.7 bar.

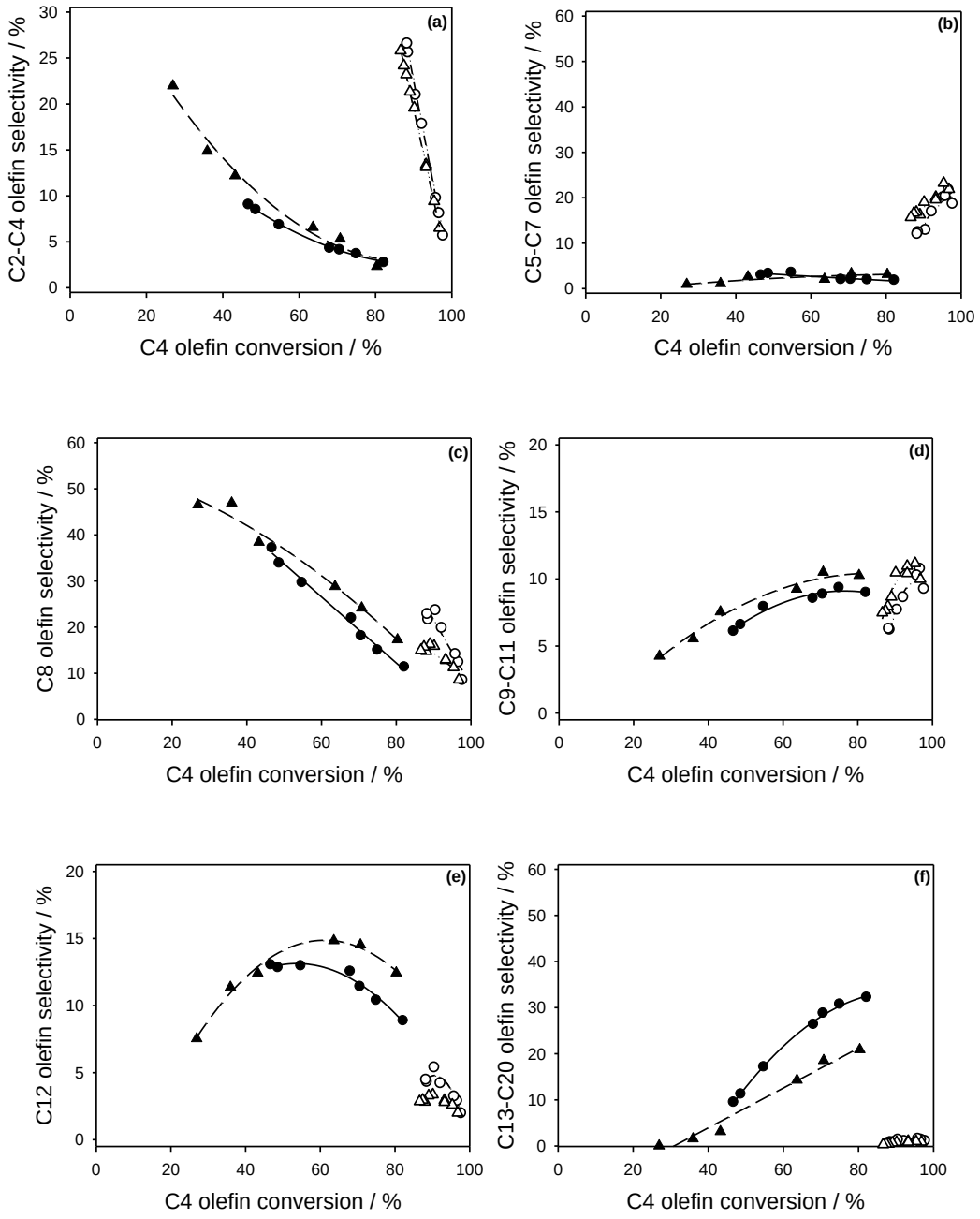


**Figure S2.4.** Selectivities for (a) C2-C3olefins, (b) C5-C7 olefins, (c) C8 olefins, (d) C9-C11 olefins, (e) C12 olefins and (f) C13-C20 olefins as a function of C4 olefin conversion at 423 K (closed) and 523 K (opened). Reaction condition: $P_{1\text{-butene}}$ = 0.9 bar, hexane to 1-butene = 16.9 (●,○),$P_{1\text{-butene}}$ = 0.8 bar, hexane to 1-butene = 31.2 (▲,△).$WHSV_{1\text{-butene}}$ = 0.03 $h^{-1}$; $P_{total}$ = 62.7 bar.

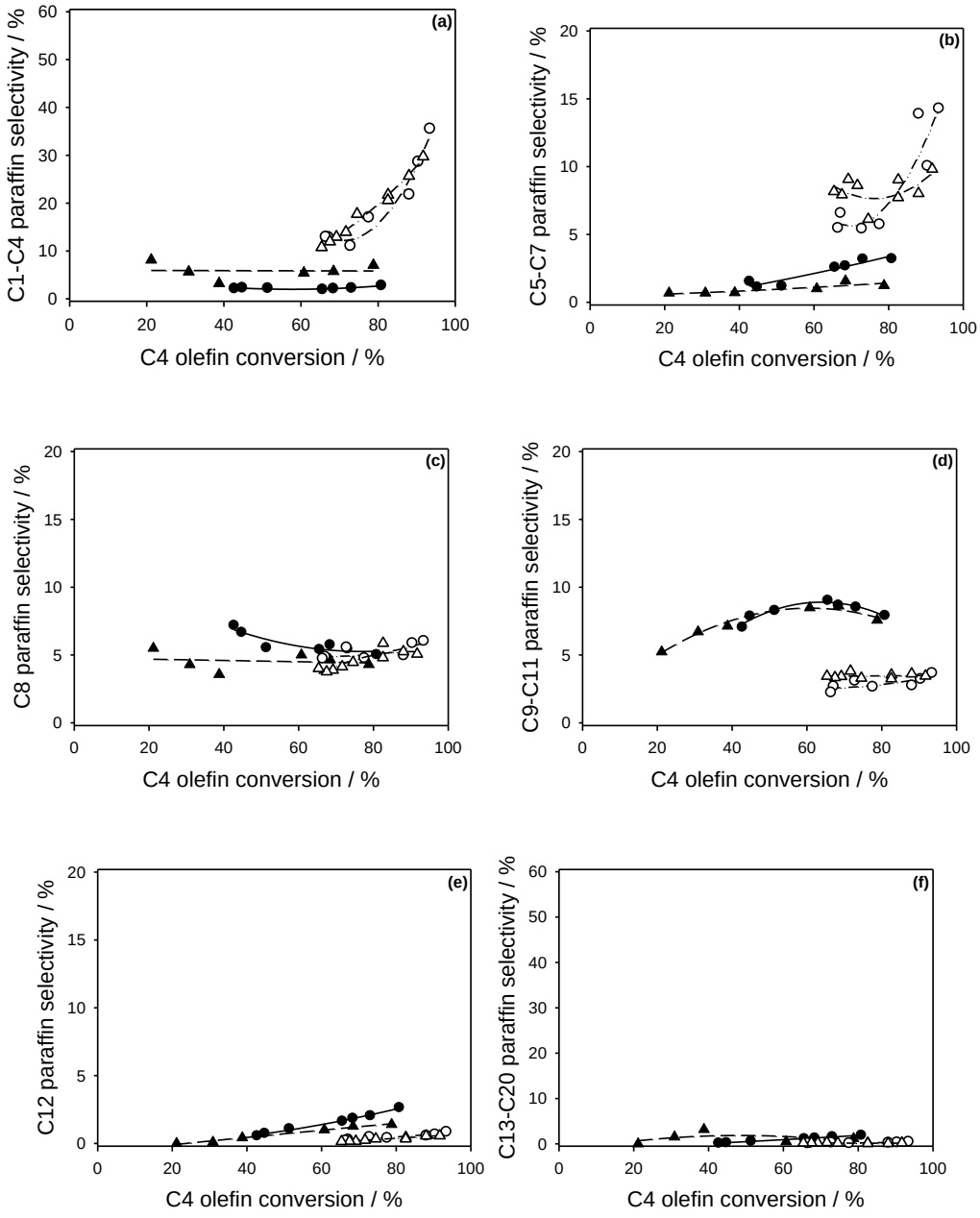


**Figure S2.5.** Selectivities for (a) C1-C4 paraffins, (b) C5-C7 paraffins, (c) C8 paraffins, (d) C9-C11 paraffins, (e) C12 paraffins and (f) C13-C20 paraffins as a function of butene conversion at 423 K (closed) and 523 K (opened). Reaction condition: $P_{1\text{-butene}}$ = 0.9 bar, hexane to 1-butene = 16.9 (●,○),$P_{1\text{-butene}}$ = 0.8 bar, hexane to 1-butene = 31.2 (▲,△).$WHSV_{1\text{-butene}}$ = 0.03 $h^{-1}$; $P_{total}$ = 62.7 bar.

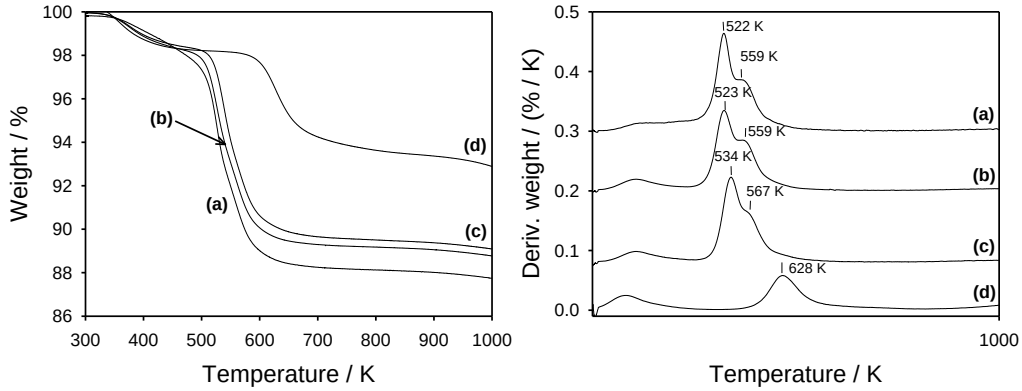


**Figure S2.6.** Thermogravimetric Analysis (TGA) under nitrogen of spent H-FER catalysts; (a) 423 K, feed hexane to 1-butene = 3.1, $WHSV_{1\text{-butene}}$ = 0.03 $h^{-1}$; $P_{1\text{-butene}}$ = 1.2 bar, $P_{total}$ = 62.7 bar, (b) 423 K, feed hexane to 1-butene = 18.1, $WHSV_{1\text{-butene}}$ = 0.03 $h^{-1}$; $P_{1\text{-butene}}$ = 0.9 bar, $P_{total}$ = 62.7 bar, (c) 423 K, feed hexane to 1-butene = 34.3, $WHSV_{1\text{-butene}}$ = 0.03 $h^{-1}$; $P_{1\text{-butene}}$ = 0.8 bar, $P_{total}$ = 62.7 bar, and (d) 523 K, 2.0 mol% 1-butene in helium, $WHSV_{1\text{-butene}}$ = 0.03 $h^{-1}$; $P_{1\text{-butene}}$ = 0.14 bar. $P_{total}$ = 6.9 bar.

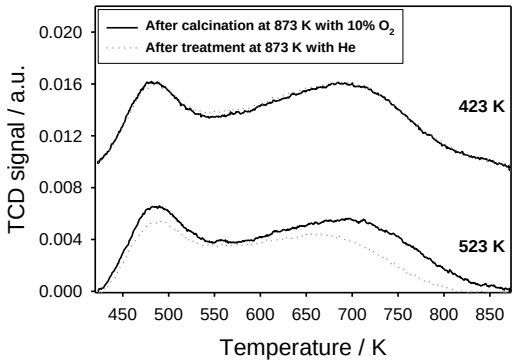


**Figure S2.7.** Temperature-programmed desorption of ammonia ($NH_3$-TPD) for H-FER after reaction at 423 K and 523 K. Reaction condition: 423 K: $P_{1\text{-butene}}$ = 0.9 bar, feed hexane to 1-butene = 18.1, $WHSV_{1\text{-butene}}$ = 0.03 $h^{-1}$; $P_{total}$ = 62.7 bar. 523 K: 2.0 mol% 1-butene in helium, $WHSV_{1\text{-butene}}$ = 0.03 $h^{-1}$; $P_{total}$ = 6.9 bar, $P_{1\text{-butene}}$ = 0.14 bar.

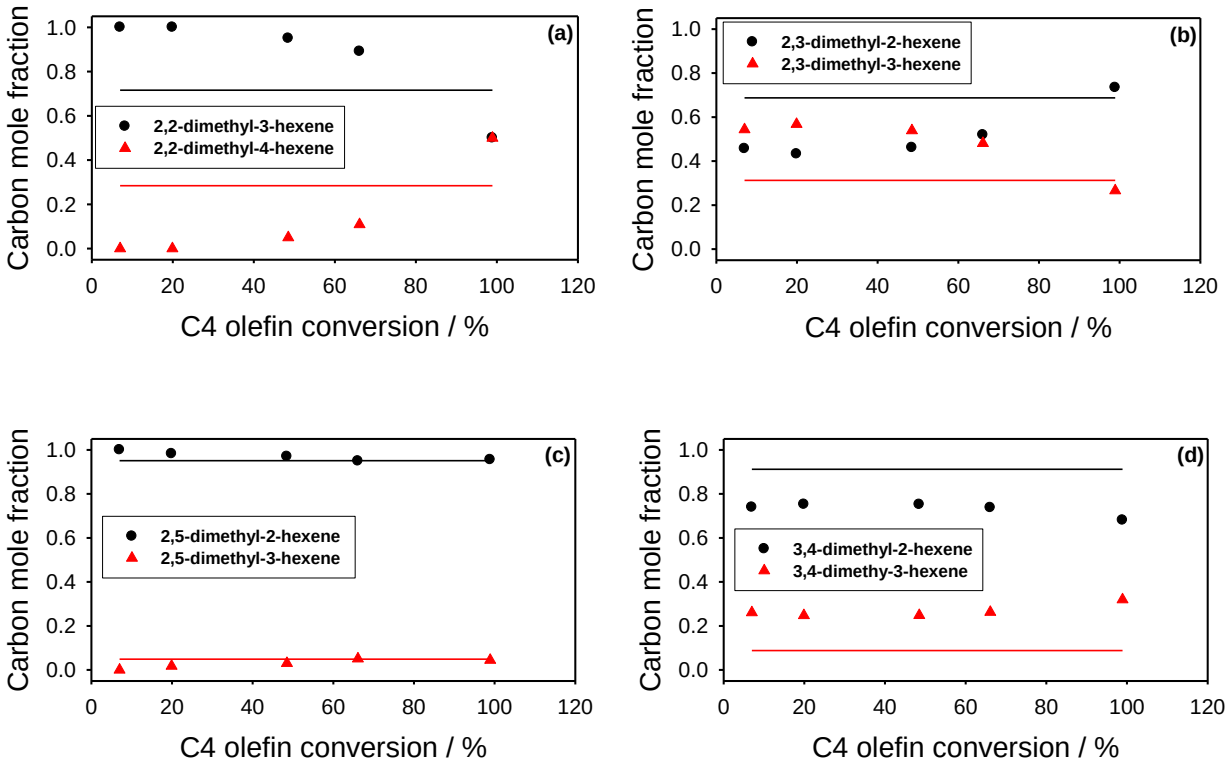


**Figure S2.8.** Carbon mole fraction (dotted) as a function of C4 olefin conversion and equilibrium composition (lined) of C8 olefins viz. (a) 2,2-dimethyl-3-hexene vs. 2,2-dimethyl-4-hexene, (b) 2,3-dimethyl-2-hexene vs. 2,3-dimethyl-3-hexene, (c) 2.5-dimethyl-2-hexene vs. 2,5-dimethyl-3-hexene, (d) 3,4-dimethyl-2-hexene vs. 3,4-dimethyl-3-hexene. Reaction condition: $P_{total}$ = 62.7 bar, $P_{1\text{-butene}}$ = 62.7 bar, T = 423 K.

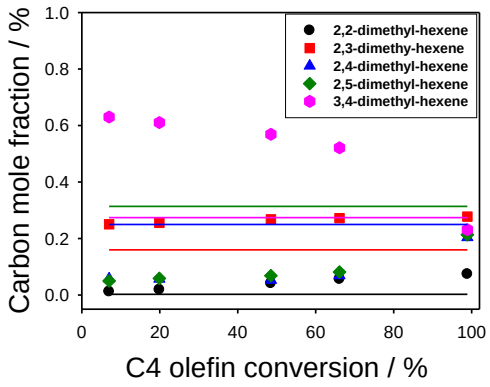


**Figure S2.9.** Carbon mole fraction (dotted) as a function of C4 olefin conversion and equilibrium composition (lined) of C8 olefins for 2-butene conversion. Reaction condition: $P_{total}$ = 62.7 bar, $P_{1\text{-butene}}$ = 62.7 bar, T = 423 K.

## 2.6 References


1. L. Cueto-Felgueroso, R. Juanes, P. Natl, Acad. Sci. USA 110 (2013) 19660–19661.
2. N. Rahimi, R. Karimzadeh, Appl. Catal., A: Gen. 398 (2011) 1–17.
3. W.F.H.K. Tanabe, Appl. Catal., A: Gen. 181 (1999) 399–434.
4. J. Skupin´ ska, Chem. Rev. 91 (1991) 613–648.
5. C.T. O'Connor, M. Kojima, Catal. Today 6 (1990) 329–349.
6. A.M. Al-Jarallah, J.A. Anabtawi, M.A.B. Siddiqui, A.M. Aitani, A.W. Al-Sa'doun, Catal. Today 14 (1992) 1–124.
7. K. Tanabea, W.F. Hölderich, Appl. Catal., A: Gen. 181 (1999) 399–434.
8. D.K.S. Albrecht, D. Maschmeyer, F. Nierlich, G. Wendt, Chem. Eng. Technol. 77 (2007) 695–709.
9. M. Bjørgen, K.-P. Lillerud, U. Olsbye, S. Bordiga, A. Zecchina, J. Phys. Chem. B 108 (2004) 7862–7870.
10. V.N. Ipatieff, J. Ind. Eng. Chem. 27 (1935) 1067–1069.
11. V.N. Ipatieff, G. Egloff, Oil Gas J. 33 (1934) 31.
12. J.P. van den Berg, J.P. Wolthuizen, J.H.C. van Hooff, J. Catal. 80 (1983) 139–144.
13. J.P. van den Berg, J.P. Wolthuizen, A.D.H. Clague, G.R. Hays, R. Huis, J.H.C. van Hooff, J. Catal. 80 (1983) 130–138.
14. S.A. Tabak, F.J. Krambeck, W.E. Garwood, AIChE J. 32 (1986) 1526–1531.
15. K.G. Wilshier, P. Smart, R. Western, T. Mole, T. Behrsing, Appl. Catal. 31 (1987) 339–359.
16. L.A.G.R.J. Quann, S.A. Tabak, F.J. Krambeck, Ind. Eng. Chem. Res. 27 (1988) 565–570.
17. Y. Chu, B. Han, A. Zheng, F. Deng, J. Phys. Chem. C 116 (2012) 12687–12695.
18. J.A. Martens, R. Ravishankar, I.E. Mishin, P.A. Jacobs, Angew. Chem., Int. Ed. 39 (2000) 4376–4379.
19. M.L. Occelli, J.T. Hsu, L.G. Galya, J. Mol. Catal. 32 (1985) 377–390.
20. A. Stepanov, M. Luzgin, S. Arzumanov, H. Ernst, D. Freude, J. Catal. 211 (2002) 165–172.
21. A. Coelho, G. Caeiro, M.A.N.D.A. Lemos, F. Lemos, F.R. Ribeiro, Fuel 111 (2013) 449–460.
22. J.W. Yoon, J.H. Lee, J.-S. Chang, D.H. Choo, S.J. Lee, S.H. Jhung, Catal. Commun. 8 (2007) 967–970.
23. M. Henry, M. Bulut, W. Vermandel, B. Sels, P. Jacobs, D. Minoux, N. Nesterenko, J.P. Dath, Appl. Catal., A: Gen. 437–438 (2012) 96–103.
24. M. Henry, M. Bulut, W. Vermandel, B. Sels, P. Jacobs, D. Minoux, N. Nesterenko, S. Van Donk, J.P. Dath, Appl. Catal., A: Gen. 413–414 (2012) 62–77.
25. J.A. Martens, W.H. Verrelst, G.M. Mathys, S.H. Brown, P.A. Jacobs, Angew. Chem., Int. Ed. 44 (2005) 5687–5690.
26. M.R. Apelian, J.R. Boulton, A.S. Fung, US Patent 5 284 989, to Mobil Oil Corporation.
27. S.W. Beadle, G.M.K. Mathys, C.M. Cheng-Guajardo, US Patent 7 345 212 B2, to ExxonMobil Chemical Patents, Inc.

28. A. Corma, C. Martinez, E.J. Doskocil, G. Yaluris, US Patent 2012 0 178 615.
29. J.S. Buchanan, J.C.-Y. Cheng, J.M. Dakka, J.E. Stanat, US Patent Application 2011 0 282 120, to BP Corporation North America, Inc.
30. M.E. Loescher, D.G. Woods, M.J. Keenan, S.E. Silverberg, P.W. Allen, US Patent 7 145 049 B2, to Exxonmobil Chemical Patents, Inc.
31. J.C. Cheng, S. Miseo, S.L. Soled, J.S. Buchanan, J.S. Feeley, 7 759 533 B2, to ExxonMobil Research.
32. J.P.G. Pater, P.A. Jacobs, J.A. Martens, J. Catal. 184 (1999) 262–267.
33. Y. Iwase, Y. Sakamoto, A. Shiga, A. Miyaji, K. Motokura, T.-R. Koyama, T. Baba, J. Phys. Chem. C 116 (2012) 5182–5196.
34. S. van Donk, E. Bus, A. Broersma, J.H. Bitter, K.P. de Jong, J. Catal. 212 (2002) 86–93.
35. B. Demenorval, P. Ayrault, N. Gnep, M. Guisnet, J. Catal. 230 (2005) 38–51.
36. P. Andy, N.S. Gnep, M. Guisnet, E. Benazzi, C. Travers, J. Catal. 173 (1998) 322– 332.
37. P. Andy, D. Martin, M. Guisnet, J. Phys. Chem. B 104 (2000) 4827–4834.
38. C.S.H. Chen, R.F. Bridger, J. Catal. 161 (1996) 687–693.
39. V.K. Ahluwalia, M. Goyal, A Textbook of Organic Chemistry, Narosa Publishing House, New Delhi, 2000.
40. W.-Q. Xu, Y.-G. Yin, S.L. Suib, J.C. Edwards, C.-L. O'Young, J. Phys. Chem. 99 (1995) 9443–9451.
41. H.S. Cerqueira, G. Caeiro, L. Costa, F. Ramôa Ribeiro, J. Mol. Catal. A: Chem. 292 (2008) 1–13.
42. J.P.G. Pater, P.A. Jacobs, J.A. Martens, J. Catal. 179 (1998) 477–482.
43. V. Hulea, F. Fajula, J. Catal. 225 (2004) 213–222.
44. J.M. Escola, R.V. Grieken, J. Moreno, R. Rodríguez, Ind. Eng. Chem. Res. 45 (2006) 7409–7414.
45. J. Wang, F. Hassan, P.I. Chigada, S.P. Rigby, B. Al-Duri, J. Wood, Ind. Eng. Chem. Res. 48 (2009) 7899–7909.
46. L. Fan, I. Nakamura, S. Ishida, K. Fujimoto, J. Chem. Eng. Jpn. 31 (1998) 585– 588.
47. I. Daems, P. Leflaive, A. Méthivier, J.F.M. Denayer, G.V. Baron, Microporous Mesoporous Mater. 82 (2005) 191–199.
48. J.F. Griffith, W.L. Winniford, K. Sun, R. Edam, J.C. Luong, J. Chromatogr., A 1226 (2012) 116–123.
49. C. Costa, J.M. Lopes, F. Lemos, F.R. Ribeiro, J. Mol. Catal. A: Chem. 144 (1999) 207–220.
50. M. Boronat, P. Viruela, A. Corma, J. Phys. Chem. B 101 (1997) 10069–10074.
51. O. Levenspiel, J. Catal. 25 (1972) 265–272.
52. O. Levenspiel, Chem. Eng. Sci. 35 (1980) 1821–1839.
53. J.A. Beattie, S. Marple, J. Am. Chem. Soc. 72 (1950) 1449–1452.
54. J.C. Gee, S.T. Williams, J. Catal. 303 (2013) 1–8.
55. M.C. Clark, B. Subramaniam, Ind. Eng. Chem. Res. 37 (1998) 1243–1250.
56. X. Liu, W. Linghu, X. Li, K. Asami, K. Fujimoto, Appl. Catal., A: Gen. 303 (2006) 251–257.
57. E. Iglesia, S.C. Reyes, R.J. Madon, J. Catal. 129 (1991) 238–256.
58. E. Iglesia, Appl. Catal., A: Gen. 161 (1997) 59–78.

59. G.V.Z. Schulz, Phys. Chem., Abt. B (1935) 379–398.
60. G.V.Z. Schulz, Phys. Chem., Abt. B (1939) 25–46.
61. P.J. Flory, J. Am. Chem. Soc. 62 (1940) 1561–1565.
62. A.N. MLinar, P.M. Zimmerman, F.E. Celik, M. Head-Gordon, A.T. Bell, J. Catal. 288 (2012) 65–73.
63. M. Lallemand, A. Finiels, F. Fajula, V. Hulea, Appl. Catal., A: Gen. 301 (2006) 196–201.
64. M. Lallemand, O.A. Rusu, E. Dumitriu, A. Finiels, F. Fajula, V. Hulea, Appl. Catal., A: Gen. 338 (2008) 37–43.
65. R.A. van Santen, Theory of Bronstead acidity in zeolites, in: M. Stöcker, H. Karge, J. Jansen, J. Weitkamp (Eds.), Studies in Surface Science and Catalysis, 1994, pp. 273–294.
66. M.A. Sanchez-Castillo, N. Agarwal, C. Miller, R.D. Cortright, R.J. Madon, J.A. Dumesic, J. Catal. 205 (2002) 67–85.

# Chapter 3. Production of linear octenes from oligomerization of 1-Butene over carbon-supported cobalt catalysts[2]

## 3.1 Introduction

In the next several years, new steam crackers are scheduled to be constructed in North America because of the increased production of low-cost shale gas [1,2]. These new olefin streams provide a valuable feedstock that can be used to make a variety of commodity chemicals including linear alpha olefins (LAOs). LAOs are important comonomers in the production of polyethylene, plasticizers, and surfactants [3]. The industrial production of linear alpha olefins is from the oligomerization of ethylene through organometallic catalysis, such as the Shell higher olefin process (SHOP) (Ni complex) and the catalytic Ziegler process (triethyl-aluminum) [4]. Complexes of Co, Fe, and Cr are reported to catalyze α-olefin oligomerization yielding a distribution of linear alpha olefins that range from $C_4$ to polyethylene from a highly-purified feed stream [3,5]. It is important to state that these catalysts produce mixtures that follow the Schultz−Flory distribution. Although several other systems have been studied for alpha olefin oligomerization, they tend to produce branched products. Solid heterogeneous catalysts have several advantages over homogeneous catalysts, including recyclability, the ability to handle

---

[2] This chapter was adapted with permission from: Zhuoran Xu, Joseph P. Chada, Dongting Zhao, Carlos A. Carrero, Yong Tae Kim, Devon C. Rosenfeld, Jessica L. Rogers, Steven J. Rozeveld, Ive Hermans, George W. Huber. Production of Linear Octenes from Oligomerization of 1-Butene over Carbon-Supported Cobalt Catalysts. ACS Catalysis, 2016, 6, 3815-3825.

Author contributions: Z.X., J.P.C, D.Z., I.H. and G.W.H designed research; Z.X. and J.P.C. collected reaction data and analyzed oligomerization products; Z.X. collected XRD diffractograms; J.P.C collected XAS data; D.Z. collected and analyzed Raman spectra; S.J.R collected HRTEM images; C.C., Y.T.K, D.C.R. and J.L.R. provided technical advice with regards to experiments; Z.X., J.P.C., D.Z., I.H. and G.W.H. wrote the paper.

olefins containing more impurities, the ability to better control the olefin chain growth, and the absence of a co-catalyst for activation.

Solid acid catalysts, including zeolites and solid phosphoric acids, have been investigated for olefin oligomerization [6]. These catalysts primarily produce branched olefin oligomers along with paraffins and cycloalkenes. Some researchers have observed low selectivities of linear octenes (31−37%) from butene oligomerization over Co, Na, Ca−Y, and HNaNi-ZSM-5 [7] at a conversion between 70 and 90% and 65%, respectively. However, the production of olefins over Brønsted acid catalysts primarily forms branched species due to the higher stability of the internal (secondary and tertiary) carbocation versus the primary carbocation required for linear olefin formation. Production of linear octene using acid catalysts requires the formation of primary carbocations. We have previously studied 1-butene oligomerization on H-ferrierite and observed that the predominant products are dimethyl-hexenes, which are derived from secondary carbocation transition states [6b].

Supported nickel oxide and cobalt oxide have also been used for oligomerization of short olefins such as ethylene, propylene, butene, and hexane into longer-chain olefins. Chauvin et al. reported that $NiCl_2/Al_2O_3$ after calcination at 500 °C in air was able to oligomerize propylene in the liquid phase with 97.4% conversion and 18% n-hexene selectivity with the rest of the products being mono- and dimethyl-branched dimers [8]. The low selectivity of linear hexenes were reported to be due to Lewis and Brønsted acid sites induced by the residual chloride ions [8]. A later patent reported that alkali-metal-doped NiO supported on metal oxides produced n-octenes at 25% selectivity from butene oligomerization between 180 and 210 °C [9].

Highly dispersed metallic nickel and cobalt supported on carbon supports synthesized with various techniques displayed a unique hierarchical structure and were demonstrated to have high

activity, selectivity, and stability in a variety of hydrogenation reactions, such as the hydrogenation of chloronitrobenzenes and nitroarenes, and the 1-octene hydroformylation [10].

Schultz et al. demonstrated that cobalt oxide on carbon catalysts were selective for dimerization of propylene, 1-butene, and 1-hexene at 150 °C into linear olefins with selectivity of 52, 65, and 83%, respectively [11]. The catalysts were prepared by impregnating activated carbon with cobalt nitrate solution, with the carbon wetted with $NH_4OH$ both before and after the impregnation. The authors hypothesized that the active site was a cobalt hydride (Co(II)-H) species, as determined by a chemical titration method using wet techniques, formed after the addition of $NH_4OH$ during catalyst synthesis. The authors reported that the cobalt hydride species are thermally sensitive and are destroyed by heating at moderate temperatures (275−350 °C). The authors used catalytic hydrogenation followed by gas chromatography (GC) to identify the compounds in the product mixture. Hydrogenation of these products prior to GC analysis removes the ability to confirm the formation of olefin products or to identify the location of the double bond.

In this report we study 1-butene oligomerization over cobalt on carbon catalysts, including the identification and quantification of all the products by two-dimensional (2D) GC, assessing catalyst stability in a continuous flow reactor and identifying the catalytically active site through the use of advanced characterization tools.

## 3.2 Experimental

### 3.2.1 Catalyst preparation.

Cobalt on carbon catalysts were prepared by impregnating 5 g of sieved activated carbon (Norit, Darco MRX m-1721; BET surface area 600−800 $m^2/g$; 250− 600 μm particle size) with a

cobalt nitrate solution composed of 4.7 g of $Co(NO_3)_2 \cdot 6H_2O$ (Sigma-Aldrich) in 5.8 mL of deionized (DI) water. 2A-Co/C-XXX was prepared by treating the carbon with 4.6 mL of 30% $NH_4OH$ solution at room temperature (RT) for 0.5 h prior to cobalt impregnation. After the cobalt impregnation, the sample was then dried overnight on a hot plate at 130 °C. Another 12.5 mL of 30% $NH_4OH$ solution was added dropwise onto the sample, and the sample was dried overnight on a hot plate at 130 °C. XXX represents the pretreatment temperature for the catalyst.

**3.2.2 Catalyst characterization.**

Powder X-ray diffraction (pXRD) patterns were collected with a Rigaku Rapid II diffractometer with a Mo Kα source from 2° to 45° using a total exposure time of 30 min. Samples were packed in glass capillaries with 0.8 mm diameter and 0.01 mm thickness. Phase identification and crystallite size estimation were carried out using JADE 9 software. The $Co_3O_4$ crystallite size was calculated from the broadness of the cobalt spinel (311) peak at $2\theta = 16.79°$. Samples for XRD were pretreated in flowing helium at 150 mL/min with 5.5 °C/min ramp rate and held at a specified temperature for 2 h before the XRD measurements. Atomic compositions for Co, H, C, and N of the pretreated catalysts were determined by Galbraith Laboratories (Knoxville, TN). Thermogravimetric analysis (TGA) of the catalysts was performed with a TA Instruments Q500 system. For these experiments, approximately 20 mg of the sample was loaded onto a Pt pan in 80 mL/min $N_2$ flow with 10 °C/min ramp rate from room temperature to 100 °C and held for 30 min, and then ramped to 800 °C. The Raman spectra were obtained with a dispersive Renishaw InVia Raman spectrometer equipped with 785, 514, and 325 nm (excitation) lasers. For this study, all measurements used a 2400 l $mm^{-1}$ approximately 100% at 514 nm. For in situ Raman studies, an Olympus LMPlanFLN objective with 50× magnification and a working distance of 10.6 mm was

used. The Raman was calibrated daily to an internal Si standard at 520.7 $cm^{-1}$. The spectra were taken with a range of 200−1200 $cm^{-1}$ and a dispersion of 1.36565 $cm^{-1}$ $pixel^{-1}$. In situ measurements were taken with a fully open aperture and a 20 s exposure time, with two accumulations. Typically, 5−10 mg of the sample was placed into a Linkam CCR1000 cell. The temperature was controlled by a Linkam T95-HT system, and the heating ramp was kept at 5.5 °C $min^{-1}$, which is the same as that during pretreatment in the continuous flow reactor. A flow rate of 10 mL $min^{-1}$ He (Airgas, UHP) was used for in situ pretreatment of the catalyst. The spectra used in this study were taken at various temperatures during the in situ pretreatment. Raman spectra of Co3O4, CoO, and $Co(NO_3)_2$ bulk materials were taken at room temperature using a Leica N Plan EPI objective with 20× magnification and a working distance of 1.15 mm. The background was first subtracted from each spectrum, and the resulting spectra were normalized to the area of the carbon signal at 1600 $cm^{-1}$.

X-ray absorption spectroscopy (XAS) measurements were taken at beamline 10-BM of the Advanced Photon Source (APS) at Argonne National lab (Lemont, IL). Co/C samples were crushed and diluted with boron nitride (Sigma-Aldrich). Self-supporting pellets were pressed inside a 4 mm I.D. stainless steel cylindrical sample holder. Sample weights were calculated to give an edge step of ∼1. To allow for measurement without exposure to atmospheric conditions, the stainless steel holder was sealed in a 1 in. O.D. Kapton-windowed quartz tube fitted with Swagelok valves. The sealed sample was pretreated in a tube furnace while the sample tube was continually purged with He. After pretreatment, valves on the pretreatment tube were sealed and the samples were placed in the X-ray beam. Samples pretreated at 230 and 270 °C were analyzed without exposure to air. Samples pretreated at 350 and 550 °C and cobalt standards were exposed to air at RT prior to analysis. XAS measurements of the Co K-edge (7.709 keV) were collected in

transmission mode. X-ray absorption was measured with gas ionization chambers before and after the sample holder. Energy calibration was performed with a Co reference foil after the sample chamber. Oxidation states were quantified by comparison of the X-ray absorption near edge structure (XANES) with the experimental standards. Co/C samples were fit with a linear combination of Co foil, CoO, and $Co_3O_4$ in the range of −30 to +20 eV from the Co edge energy. The TEM images were obtained using a JEOL 2010F field emission gun (FEG) transmission electron microscopy (TEM) instrument. The TEM instrument was operated at an accelerating voltage 200 keV. Conventional TEM images were recorded using a Gatan multiscan digital camera (Model Ultrascan 1000).

**3.2.3 Catalytic measurement.**

1-Butene oligomerization reactions were carried out in a down-flow fixed-bed reactor with the liquid product analyzed by comprehensive two-dimensional gas chromatography−mass spectrometry (2D-GC-MS) as described in our earlier work. [6b] The $C_4$ compounds in the liquid or gas products were analyzed via conventional gas chromatography (GC-FID, Shimadzu). Skeletal composition of the product mixture was separately verified by hydrogenating the liquid product prior to analysis by 2D-GC-MS. Approximately 100 mg of Pd/C catalyst was packed into the GC liner for hydrogenation. Only two $C_8$ products were observed after hydrogenation, which are 3-methyl-heptane and n-octane; all the detectable hydrogenated $C_{12}$ products were branched species. The thermodynamic equilibrium composition calculations were based on Benson group thermodynamic data from Alberty and Gehrig [12] by assuming that pressure has little effect on the change of the physical property of the compounds. The equilibrium concentrations were solved by setting the change of Gibbs free energy to zero (G353k(i) = 0) for isomerization reaction

between the isomers. The following standards were tested for our product analysis: 1-octene, *trans*-2-octene, *cis*-2octene, 2-methyl-1-heptene, 2-methyl-2-heptene, *trans*-2-methyl-3-heptene, *trans*-6-methyl-3-heptene, 2,3-dimethyl-2-hexene, 2,3-dimethyl-3-hexene, 2,3,4-trimethyl-2-pentene, 2,4,4-trimethyl-2-pentene (Sigma-Aldrich), *cis*-2,5-dimethyl-3-hexene (Pfaltz & Bauer), *cis*-3-octene, *trans*-3-octene, *cis*-4-octene, *trans*-4-octene, 3-methyl-2-heptene, 3-methyl-3-heptene, 5methyl-2-heptene, 5-methyl-3-heptene, and 3,4-dimethyl-2hexene (ChemSampCo). For all the catalytic testing, 0.5 g of the catalyst particles were packed into the tubular reactor without diluents. The catalysts were pretreated in a 150 mL/ min flow of helium with 5.5 °C/min ramp rate and held at the pretreatment temperature for 2 h before the reactor was cooled to reaction temperature. 1-Butene (99.9%, Matheson) was fed into the reactor at reaction pressure (450 psig) through a high-pressure syringe pump (500D, Teledyne Isco). The liquid samples were collected at atmospheric pressure in a 50 mL glass pressure tube prechilled in dry ice filled with approximately 10 g of 0.5 wt% heptane in hexane solvent. During liquid sample draining, the volatilization of a small amount of hydrocarbon products was inevitable, which could lead to a below 100% carbon balance. The variation of weight hourly space velocity [WHSV = hourly mass liquid feed flow rate (g/h)/catalyst mass (g)] was achieved by adjusting the butene flow rate at the inlet. After reaction, the spent catalysts were recovered from the reactor and exposed to the air before XRD characterization.

The butene conversion was calculated according to Eq 3.1. Butene consumption rate was calculated according to Eq 3.2. When calculating the kinetics values, butene isomers including 1-butene and *trans*- and *cis*-2-butene were grouped together and considered to be nonconverted feed. The number of chain branches (NCB) was calculated according to Eq 3.3. Total $C_4$ dimer distribution and total linear octene distribution were calculated using Eqs 3.4 and 3.5, respectively.

$$\text{Butene conversion (\%)} = \frac{\text{moles of carbon in the detected products}}{\text{moles of carbon in the feed butene}} x100\% \qquad \text{[Eq. 3.1]}$$

$$\text{Butene consumption rate } (\text{mol}_{butene}/\text{mol}_{Co}/\text{h}) = \frac{\text{butene inlet flow rate} \times \text{butene conversion}}{\text{moles cobalt in the catalyst}}$$

[Eq. 3.2]

$$NCB = 0 \times \text{linaer octene distribution (\%)} x100\% + 1 \times \text{methyl} - \text{heptene distribution (\%)} + 2 \times \text{dimethyl} - \text{hexene distribution (\%)}$$

[Eq. 3.3]

$$\text{Total } C_4 \text{ dimer distribution (\%)} = \frac{\text{carbon moles in the } C_8 \text{ olefins}}{\text{sum of carbon moles in all the detected products}} x100\%$$

[Eq 3.4]

$$\text{Total linear octene distribution (\%)} = \frac{\text{moles of linear octenes}}{\text{moles of total C8 olefins}} x100\% \qquad \text{[Eq 3.5]}$$

## 3.3 Results and Discussion

### 3.3.1 Oligomer product selectivity.

The 2D-GC revealed the cobalt-catalyzed butene oligomerization reactions produce only longer-chain olefins (Figure 3.1a). Over 94% of the non-C4 products were butene dimers for all catalysts used in this study, as shown in Figure 3.1 and Table 3.1. Additional products were branched $C_{12}$ olefins. A small amount of $C_{16}$ olefins (0.3% selectivity) was observed for the 2A-Co/C-230 catalyst run at the lowest WHSV (0.25 $h^{-1}$). $C_8$ isomer identification was carried out by matching the location of the product trace in the 2D-GC image with that of standards. The 2D-gas chromatogram of a typical product distribution is shown in Figure 3.1. Figure 3.1a shows the overall 2D-GC template, and Figure 3.1b shows the zoomed-in region for the $C_8$ olefins along with the assignment of each peak. Hydrogenation of our product mixture and analysis with Pd/C showed that our products contained only n-octenes and methyl-heptenes, corroborating our assignments made using 2D-GC. The trans and *cis* isomers of 3-octene and 4-octene were not

distinguishable. The only methyl-heptene isomers that we observed were 5-methylheptenes and 3-methyl-heptenes.

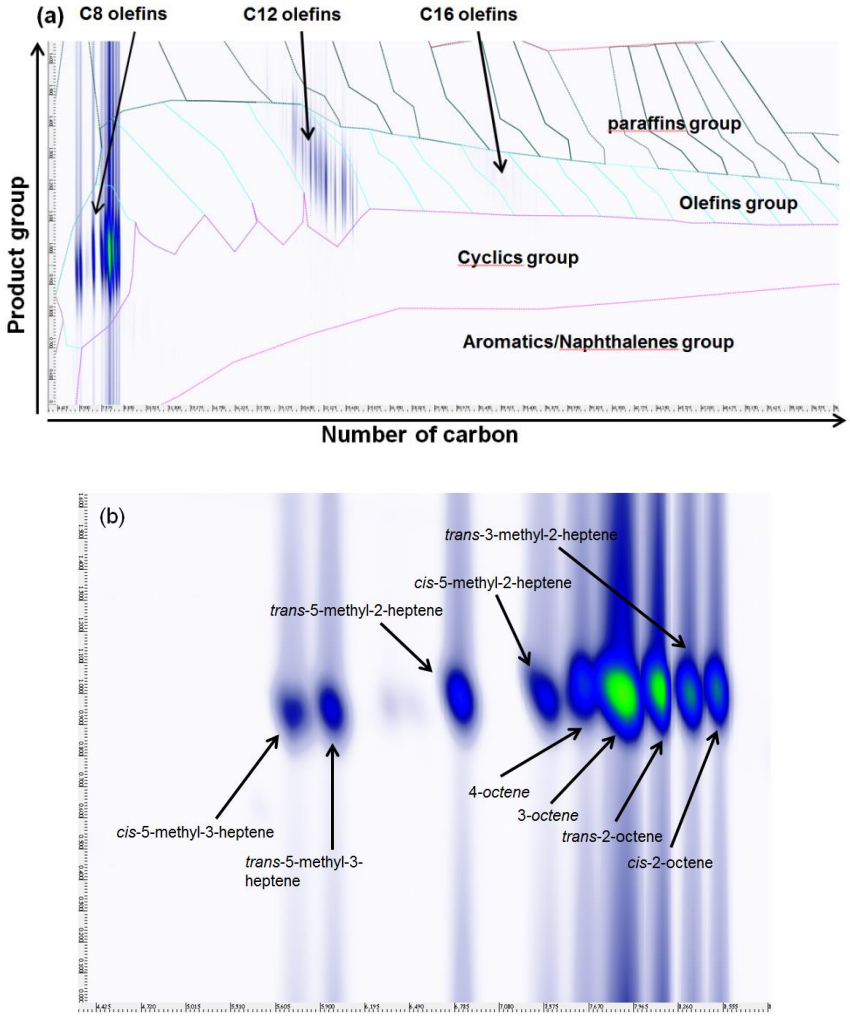


**Figure 3.1.** 2D-GC image of (a) all potential C8-C20 products and (b) butene dimerization products assignment for the run over 2A-Co/C-230 at 0.25 $h^{-1}$ WHSV and 27 h time on stream for 1-butene conversion at 80 ℃, 450 psig.

As shown in Table 3.1, between 77 and 90% of the products were linear octenes, which is higher than that reported in previous studies (about 65%) [11b]. Only minor amounts of 1-octene (less than 1%) were observed. At low WHSV, the linear octene products in decreasing abundance were 3-octene > *trans*-2-octene > *cis*-2-octene > 4-octene. The 3-octene and *cis*-2-octene distribution decreases, and the 4-octene distribution increases with conversion. It is likely that the

$C_8$ products tend to approach equilibrium of octene isomers (Table S4.2) at higher conversion. Aside from linear octenes, all four catalysts produced *trans*-3-methyl-2-heptene, *trans*- and *cis*-5-methyl-3-heptene, and *trans*- and *cis*-5-methyl-2-heptene. No alpha methyl-heptene products were detected. The octene product distribution is similar among the four different catalysts.

**Table 3.1.** Average product selectivity for butene oligomerization[a]

| catalyst | 2A-Co/C-230 | | | 2A-Co/C-270 | | | 2A-Co/C-350 | |
|---|---|---|---|---|---|---|---|---|
| WHSV($hr^{-1}$) | 14.14 | 0.71 | 0.25 | 14.14 | 0.71 | 0.25 | 14.14 | 0.71 |
| TOS/h | 40 | 94 | 37 | 40 | 91 | 35 | 40 | 75 |
| conversion (%) | 9.77 | 11.42 | 29.00 | 3.94 | 5.74 | 21.4 | 1.27 | 6.74 |
| total C4 dimer selectivity (%) | 98.5 | 96.6 | 94.4 | 98.7 | 96.6 | 97.6 | 99.6 | 97.6 |
| total C12 selectivity (%) | 1.5 | 3.4 | 5.3[b] | 1.3 | 3.4 | 2.3[c] | 0.4 | 2.4 |
| specific C4 dimer distribution (%) | | | | | | | | |
| *cis*-2-octene | 12.3 | 7.1 | 6.9 | 11.6 | 6.0 | 12.8 | 7.7 | 5.3 |
| *trans*-2-octene | 17.7 | 19.7 | 19.8 | 17.3 | 16.9 | 17.6 | 24.7 | 16.4 |
| *cis*/*trans*-3-octene | 52.9 | 45.4 | 43.9 | 52.5 | 42.5 | 54.7 | 46.1 | 39.6 |
| *cis*/*trans*-4-octene | 1.3 | 5.3 | 7.7 | 1.4 | 8.7 | 2.2 | 5.4 | 13.4 |
| *cis*-5-methyl-3-heptene | 1.7 | 2.2 | 1.8 | 2.2 | 2.7 | 1.5 | 1.6 | 1.0 |
| *trans*- 5-methyl-3-heptene | 1.9 | 2.5 | 2.7 | 2.0 | 2.9 | 2.2 | 2.0 | 3.2 |
| trans-3-methyl-2-heptene | 3.3 | 9.8 | 9.6 | 4.9 | 12.3 | 3.6 | 5.6 | 12.7 |
| *trans*-5-methyl-2-heptene | 2.6 | 4.0 | 4.3 | 3.2 | 4.6 | 2.7 | 3.4 | 5.0 |
| *cis*-5-methyl-2-heptene | 6.1 | 4.0 | 3.2 | 5.9 | 3.4 | 2.8 | 3.3 | 2.8 |
| NCB | 0.16 | 0.23 | 0.21 | 0.18 | 0.26 | 0.14 | 0.16 | 0.25 |
| total linear octene distribution (%) | 84.2 | 77.5 | 78.4 | 82.8 | 74.1 | 87.2 | 83.9 | 74.7 |
| carbon balance (%) | 90.4 | 103.2 | 98.3 | 89.4 | 90.3 | 104.2 | 96.5 | 103.6 |

[a]Reaction conditions: 80 °C, 450 psig. [b]$C_{16}$ olefin was also observed with 0.3% selectivity. [c]$C_{16}$ olefin was also observed with 0.1% selectivity.

Figure 3.2 shows the octene product distribution as a function of time on stream for 2A-Co/C-270. Similar trends were observed for all the other catalysts (Figure S3.1−S3.3). The octene distribution was nearly constant at 14.14 $h^{-1}$ WHSV even though the butene conversion was slightly decreasing during this time (see Figure 3.3a). At higher conversion (0.71 $h^{-1}$ WHSV), the selectivity of linear octenes, except *trans*-4-octene, decreases and the selectivity of *trans*-3-methyl-2-heptene increases with time on stream.

The hydrocarbon selectivity we determined is consistent with the analyses of Schultz et al., who reported a hydrogenated mixture composition of 65.3% n-octane, 34.4% 3-methyl-heptane,

and 0.3% 3,4-dimethyl-hexane at 13.6% 1-butene conversion [11b]. Key differences are that we did not observe the formation of dimethyl hexene and the selectivity to linear octene was 8.8−21.9% higher in our study. The observed linear octene selectivity was also higher compared to the ion-exchanged zeolites (below 40%) [7]. Unlike olefin oligomerization with homogeneous catalysts, no 1-octene was detected [3−5].

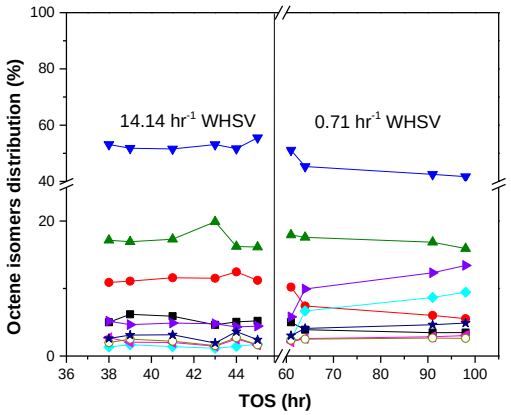


**Figure 3.2.** Octene isomers distribution with time on stream over 2A-Co/C-270, including: (▼) *trans*-3-octene, (▲) *trans*-2-octene, (●) *cis*-2-octene, (■) *cis*-5-methyl-2-heptene, (►) 3-methyl-2-heptene, (◆) *trans*-4-octene, (◄) *trans*-5-methyl-3-heptene, (○) *cis*-5-methyl-3-heptene and (★) *trans*-5-methyl-2-heptene at 80℃ and 450 psig.

### 3.3.2 Catalytic activity measurements.

The effect of pretreatment on the catalytic activity was studied by activating the catalyst at different temperatures in helium. Panels a and b of Figure 3.3 compare the butene consumption rate of 2A-Co/C-230, 2A-Co/C-270, 2A-Co/C-350, and 2A-Co/C-550 catalysts at 14.14 $h^{-1}$ and 0.71 $h^{-1}$ WHSV, respectively. All catalysts were tested by the following reaction sequence: 0.71 $h^{-1}$ WHSV (Figure 3.3b) for approximately 36 h, then 10 h of operation at 14.14 $h^{-1}$ WHSV,

followed by 40 h of operation at 0.71 $h^{-1}$. Faster catalyst deactivation was observed if the catalyst was tested starting at the higher WHSV (Figure S3.4).

Average butene conversion, deactivation rate, and average butene consumption rate for each catalyst are summarized in Table 3.2 at both space velocities. At 14.14 $h^{-1}$ WHSV, the activity of the catalysts decreased with increasing pretreatment temperature. It is worth noting that by lowering the pretreatment temperature from 270 to 230°C, the reaction rate doubled. A steady catalytic performance was observed for each catalyst after the first sampling point. The average rate for each catalyst decreased at a lower WHSV of 0.71 $h^{-1}$ (Figure 3.3b). 2A-Co/C-230 is the most active catalyst at both 14.14 and 0.71 h−1 WHSV. A slow deactivation was observed at the higher WHSV with 2A-Co/C-230, while no deactivation was observed with the other catalysts. At the lower WHSV, a much slower deactivation rate was observed.

**Table 3.2.** Average Reaction Rates and Deactivation Rates for 1-Butene Oligomerization[a]

| | 14.14 $h^{-1}$ WHSV | | | 0.71 $h^{-1}$ WHSV | | |
|---|---|---|---|---|---|---|
| catalyst | average butene conversion (%)[b] | deactivation rate at steady state ($h^{-2}$)[c] | average rate ($mol_{butene}/mol_{Co}/h$)[d] | average butene conversion (%)[b] | deactivation rate ($h^{-2}$)[c] | average rate ($mol_{butene}/mol_{Co}/h$)[d] |
| 2A-Co/C-230 | 10.11 | 0.19 ± 0.07 | 10.78 | 13.10 | $(3.20 \pm 0.89) \times 10^{-3}$ | 0.73 |
| 2A-Co/C-270 | 5.08 | – | 5.08 | 6.06 | $(1.26 \pm 0.23) \times 10^{-3}$ | 0.35 |
| 2A-Co/C-350 | 1.50 | – | 1.71 | 6.02 | N.A. | 0.33 |
| 2A-Co/C-550 | 0.36 | – | 0.39 | 2.20 | $(3.53 \pm 1.51) \times 10^{-3}$ | 0.12 |

[a]Reaction conditions: 1-butene feed, 450 psig, 80°C, 14.14 $h^{-1}$ WHSV, and 0.71 $h^{-1}$ WHSV. [b]Mathematical average of the data taken with TOS shown in Figure 3.3a (14.14 $h^{-1}$) and Figure 3.3b (0.71 $h^{-1}$). [c]The value of the slope calculated from Figure 3.3a except for the first sample. [d]The value of the slope calculated from Figure 3.3b, accounting for all the data points collected.

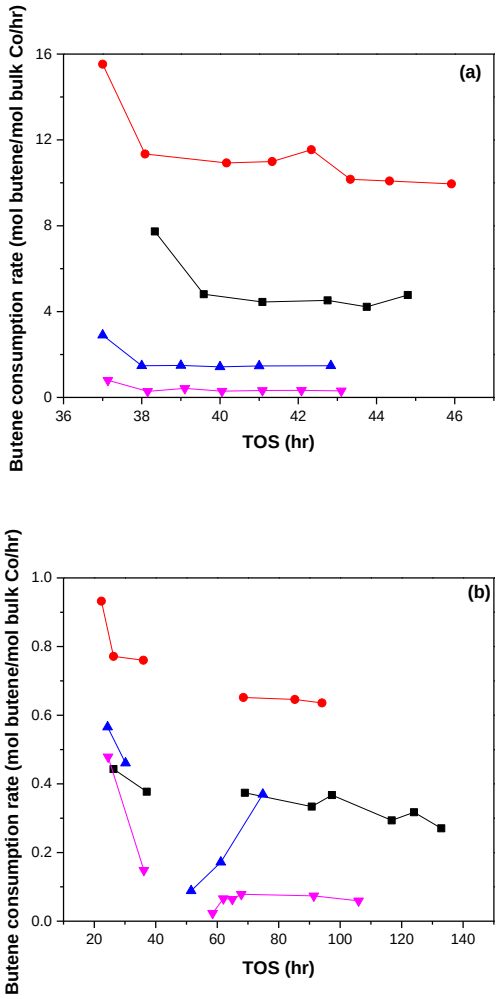


**Figure 3.3.** Butene consumption rate as a function of time on stream for (●) 2A-Co/C-230, (■) 2A-Co/C-270, (▲) 2A-Co/C-350 and (▼) 2A-Co/C-550, at (a) 14.14 $h^{-1}$ WHSV and (b) 0.71 $h^{-1}$ WHSV. Reaction condition: 1-butene feed, 450 psig, 80℃.

The butene distribution is shown in Figure 3.4 for 2A-Co/C230. At the higher WHSV, these products were not in thermodynamic equilibrium with 1-butene being the main butene isomer. The three butene isomers deviate further from their equilibrium compositions with increasing time-on-stream. At 0.71 $h^{-1}$ WHSV, the butene isomers were in thermodynamic equilibrium as shown in Figure 3.4b. Schultz et al. also observed isomerization of 1-butene to *cis*- and *trans*-2-butene during 1-butene dimerization in a batch reactor [11b], with the butene isomer

compositions close to their equilibrium (10.6% 1-butene, 31.1% *cis*-2-butene, and 58.2% *trans*-2-butene).

The absence of heat and mass transport limitations were verified by commonly accepted calculations for heterogeneous catalysts systems [13]. Heat effects due to interphase, interparticle, and intraparticle heat transport were evaluated. The heat of reaction (42 kJ/mol) was determined from the heat of formation of reactants and products at reaction temperature. An activation energy (Ea) of 70 kJ/mol was used based on the work of Toch et al. for ethylene oligomerization [14]. The heat transfer coefficient (300 W $m^{-1}$ $K^{-1}$) for the liquid phase was determined by assuming a stagnant hydrocarbon film. The thermal conductivity of the catalyst was estimated to be the same as the carbon support (0.1 W $m^{-2}$ $K^{-1}$). An energy balance on the heat generated and removed showed a negligible temperature rise between the bulk phase and the catalyst surface.

For mass transfer effects, it was assumed that diffusion within the porous support or interparticle mass transport would be the limiting regime. The Weisz−Prater criteria was evaluated to ensure the absence of concentration gradients within the catalyst particles. In the absence of an absolute value for the diffusivity of liquid-phase 1-butene through its oligomer products, the diffusivity was estimated to be within the range of liquid systems ($8 \times 10^{-6}$ $cm^2/s$). The concentration of 1butene at the surface of the particle was conservatively estimated to be 80% of the concentration in the unreacted stream. Based on the calculations (Table S3.1), the reaction is not limited by transport phenomena for the data collected in this chapter [15].

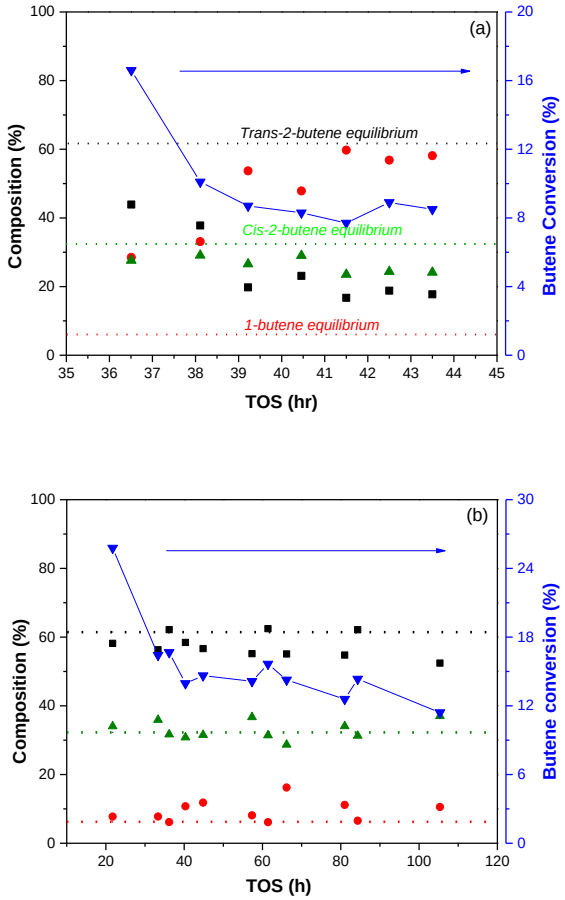


**Figure 3.4.** Total butenes conversion (▼) and C4 olefin distribution as a function of time on stream: (■) *trans*-2-butene, (●) 1-butene, (▲) *cis*-2-butene, and butene distribution equilibrium (dotted lines) at 80℃, 450 psig, 1-butene feed at (a) 14.14 $h^{-1}$ WHSV (b) at 0.71 $h^{-1}$ WHSV over 2A-Co/C-230.

### 3.3.2 Catalyst characterization.

Table 3.3 shows the elemental analysis and $Co_3O_4$ crystallite size for the fresh and spent catalysts. All catalysts and the activated carbon contained nitrogen. The nitrogen comes from three potential sources: undecomposed cobalt nitrate, activated carbon support, and $NH_4OH$. Similar amounts of nitrogen are observed on the spent catalyst (2A-Co/C-270), demonstrating that nitrogen is not lost from the catalyst during reaction.

**Table 3.3.** Elemental Analysis and Crystallite Size Estimation of Fresh and Spent Catalysts[a]

| | elemental analysis wt % | | | |
|---|---|---|---|---|
| catalyst code | Co | C | N | $Co_3O_4$ crystallite size (nm) by XRD[b] |
| 2A-Co/C-230 | 13.20 | 51.83 | 1.24 | 7.2 ± 0.2 (6.2 ± 0.2) |
| 2A-Co/C-270 | 12.30 (13.20) | 63.41 (56.90) | 1.64 (1.76) | 6.4 ± 1.6 (5.4 ± 0.2) |
| 2A-Co/C-350 | 12.3 | 54.61 | 1.37 | 5.7 ± 0.2 (5.8 ± 0.2) |
| 2A-Co/C-550 | 15.4 | 58.31 | 1.41 | N.A. |
| A-C-270 | – | 71.22 | 0.96 | – |
| activated carbon | – | 65.59 | 0.60 | – |

[a]Spent catalyst values are shown in parentheses if available. [b]The number in the parentheses specifies the particle size for the corresponding spent catalyst. The errors were estimated by JADE software.

X-ray diffraction identified three phases on all catalysts (except for 2A-Co/C-550) as shown in Figure 3.5: graphite (largest 2θ peak at 12.15°), $Co_3O_4$ (largest 2θ peak at 16.79°), and CoO (largest 2θ peak at 19.26°). An extra high-intensity peak was observed over 2A-Co/C-550 at 2θ = 19.90°. This peak is metallic cobalt. The $Co_3O_4$ crystallite size calculated by Scherrer's equation with the peak at 16.79° was shown to be between 5 and 8 nm (Table 3.3). The $Co_3O_4$ crystallite size for 2A-Co/C-550 could not be obtained from this data. High-resolution TEM (HRTEM) images of 2A-Co/C-270 (Figure 3.6) exhibit overlapping cobalt oxide particles supported on carbon, with a particle size ranging from 5 to 10 nm. The $Co_3O_4$ particle size was not measured using HRTEM because of the overlapping cobalt oxide particles. The $Co_3O_4$ crystallite size calculated by XRD showed a slight decrease with increasing pretreatment temperature. The XRD results of the used catalysts showed similar cobalt phase composition, with no distinguishable change in $Co_3O_4$ crystallite size (Figure S4.5) compared to the fresh catalysts. Some of the changes of crystallite size may not be observable with XRD because small (<4 nm) $Co_3O_4$ crystallite sizes are not detected with this method [16]. No leaching occurred with the spent catalyst as there was no change in the XRD patterns or the cobalt weight loading for the fresh and spent catalysts.

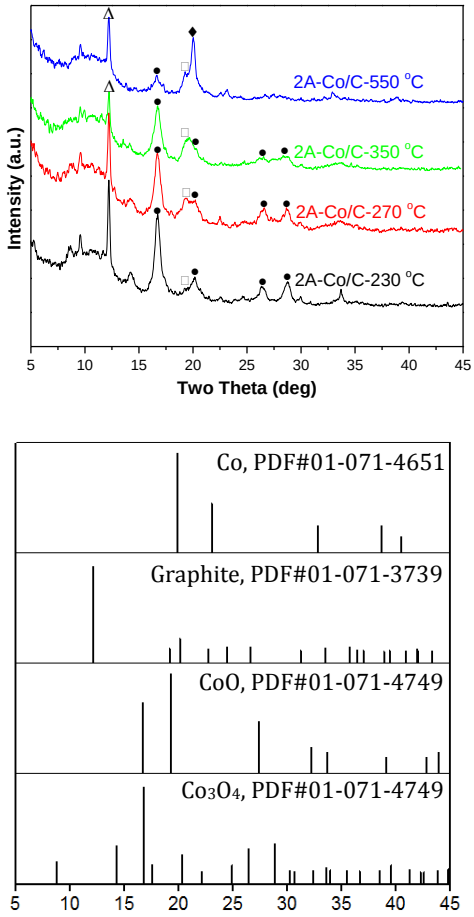


**Figure 3.5.** Mo-XRD of 2A-Co/C catalyst pretreated at different temperatures, with characteristic peaks of ∆graphite, ●$Co_3O_4$, □CoO, ◆Co.

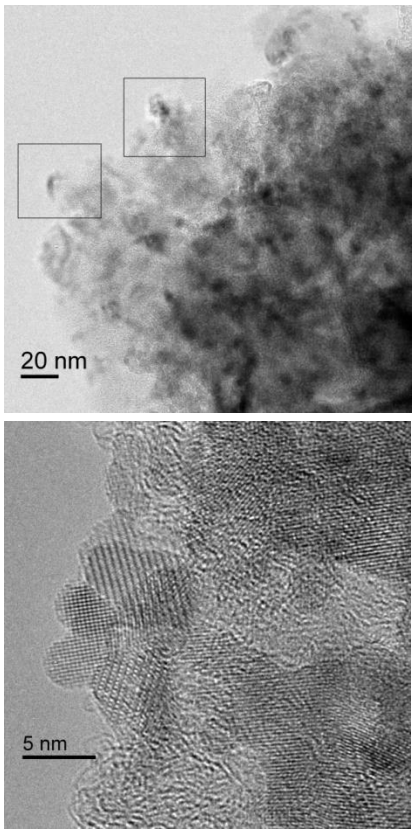


**Figure 3.6.** HRTEM image for 2A-Co/C-270. Top: overlapping cobalt oxide particles. Bottom: Zoomed-in image showing the lattice fringes of the cobalt particles.

The in situ Raman spectra of the 2A-Co/C catalyst during pretreatment are shown in Figure 3.7. Spectrum a shows characteristic peaks of $Co_3O_4$ bulk material at 481, 519, 621, and 690 $cm^{-1}$, whereas spectrum b shows CoO bulk material characteristic peaks at 517 and 684 $cm^{-1}$. Characteristic peaks of bulk $Co(NO_3)_2$ at 740, 1034, 1321, and 1442 $cm^{-1}$ are present in spectrum c. Because of the highly intense Raman spectra for the bulk materials, spectra a and c are divided to 1/2 intensity. Spectrum d shows that at room temperature, before pretreatment, a mixture of $Co(NO_3)_2$ and cobalt oxides coexist on the catalyst surface. Raising the temperature from 25 to 150 °C leads to a decrease in the intensity of the $Co(NO_3)_2$ peaks at 740 and 1034 $nm^{-1}$ (d−f) and to the emergence of new Raman signals at 481 and 690 cm−1 (g), indicating the decomposition of the $Co(NO_3)_2$ precursor and the formation of $Co_3O_4$ and CoO. The decomposition temperature of

the precursor observed by Raman (f) is about 50 °C lower than that obtained by TGA (Figure 3.8). This indicates that cobalt oxides on the catalyst surface reduce at a lower temperature than in the bulk [17]. Because the characteristic peaks of CoO (broad signal at 517 and 684 cm−1) and $Co_3O_4$ (481, 519, and 690 $cm^{-1}$) overlap, the precise composition of cobalt oxide on the catalyst surface cannot be determined. The signal intensity of CoO at 684 $cm^{-1}$ is much lower and broader than that of $Co_3O_4$ [18]. By monitoring the decrease and, more importantly, the broadening of the peak (Figure S3.6), the change of the CoO content can be qualitatively observed. As temperature increases from 150 to 550 °C (f−n), the peak at 690 $cm^{-1}$ decreases and broadens, suggesting less $Co_3O_4$ and an increased CoO content.

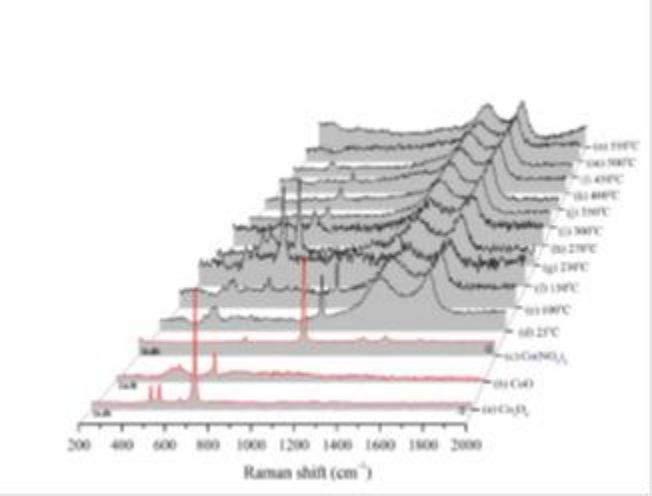


**Figure 3.7.** *In situ* Raman spectra of cobalt nitrate, $Co_3O_4$, CoO, and 2A-Co/C pretreated at different temperatures. He flow = 20 mL/min.

The composition of the cobalt phases was further investigated with XANES. Figure 3.8 shows the XANES spectra of 2A-Co/C pretreated in helium at different temperatures. The catalysts pretreated at 230 and 270 °C were analyzed immediately after helium pretreatment without being exposed to the air. The cobalt standards and the catalysts pretreated at 350 and 550 °C were exposed to air at room temperature before analysis. The phase compositions of these

different catalysts after linear combination fitting are summarized in Table 3.4. 2A-Co/C-230 and 2A-Co/C-270 showed XANES similar to a $Co_3O_4$ standard (Figure S3.7), while 2A-Co/C-350 and 2A-Co/C-550 curves clearly shifted to a lower edge energy, as shown in Figure 3.8. The gradual reduction to metallic cobalt is apparent with samples pretreated at higher temperatures and observable as a large pre-edge feature and decreasing edge peak or "white line". There is a clear trend of decreasing oxidation with increasing pretreatment temperature.

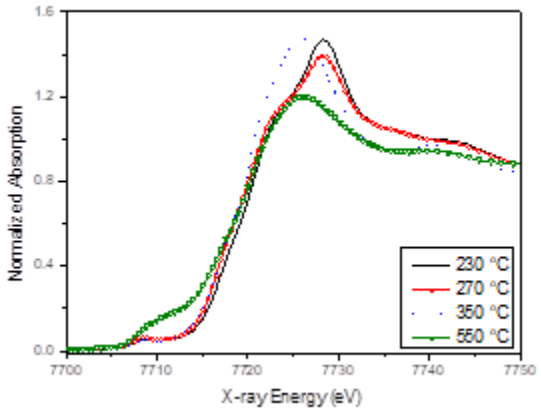


**Figure 3.8.** XANES spectra of fresh 2A-Co/C catalysts pretreated at different temperatures.

The ratio of Co(III)/Co(II) for each sample was calculated based on XANES fitting results and is summarized in Table 3.4. $Co_3O_4$ contains both Co(II) and Co(III) in the molecular formula of $Co_2O_3 \cdot CoO$. The $Co_3O_4$ content decreases with an increasing pretreatment temperature. Metallic cobalt starts to form when the pretreatment temperature is 550 °C. As shown in Table 3.2, the catalyst activity decreases with increasing pretreatment temperature, suggesting the $Co_3O_4$ phase is probably the more active phase.

Figure 3.9 shows the TGA analysis of the non-pretreated catalysts in flowing $N_2$. The 2A-Co/C catalyst showed two weight loss peaks at 208 and 621 °C. The peak at 208 °C can be

assigned to the complete decomposition of cobalt nitrate [19]. The weight loss at 621 °C is caused by the reduction of $Co_3O_4$ to a lower oxidation state (metallic cobalt or CoO), as indicated by XRD and XAS.

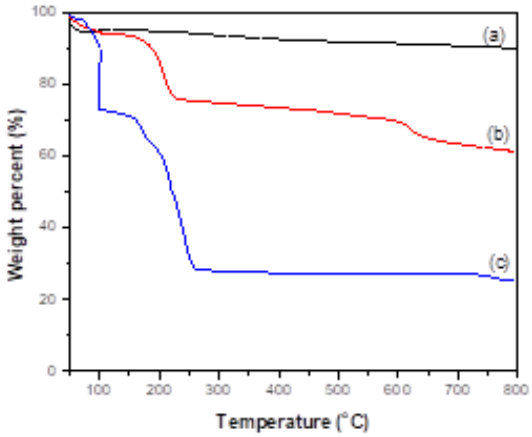


**Figure 3.9.** TGA analysis of (a) ammoniated carbon (no weight loss); (b) 2A-Co/C (18.61 wt% loss at 208℃, 6.11 wt% loss at 621℃); (c) cobalt precursor: $Co(NO_3)_2 \cdot 6H_2O$ (total 73.76 wt% loss between 100 and 254℃) in $N_2$ with 10℃/min ramp rate.

**Table 3.4.** XANES fitting results.

| sample | edge energy (eV) | XANES fit wt % | | | Co(III)/ Co(II) |
|---|---|---|---|---|---|
| | | CoO | Co | $Co_3O_4$ | |
| 2A-Co/C-230 | 7720.7 | 27.5 | – | 72.5 | 1.64 |
| 2A-Co/C-270 | 7720.1 | 32.0 | – | 68.0 | 1.32 |
| 2A-Co/C-350 | 7720.5 | 61.7 | – | 38.3 | 0.39 |
| 2A-Co/C-550 | 7720.5 | 40.1 | 36.2 | 23.7 | 0.37 |
| CoO | 7720.1 | – | – | – | |
| $Co_3O_4$ | 7724.2 | – | – | – | |
| Co | 7708.2 | – | – | – | |

From the analysis of XRD, in situ Raman, TGA, and XAS results, a cobalt phase change occurs with an increasing pretreatment temperature in an inert gas. The first step is the complete

decomposition of $Co(NO_3)_2 \cdot 6H_2O$ to $Co_3O_4$, which occurs at around 208 °C [20]. However, $Co_3O_4$ is not the only cobalt oxide being formed even at a temperature as low as 230°C. CoO could be formed either as a byproduct from cobalt nitrate decomposition or from the reduction of $Co_3O_4$ by the carbon support. With an increasing pretreatment temperature, more $Co_3O_4$ is converted to CoO, followed by a further reduction of CoO to Co when the temperature reaches 550 °C. We plan on exploring the nature of cobalt oxide formation and subsequent high-temperature reduction in the future.

### 3.3.3 Discussion of reaction pathway.[3]

A proposed reaction pathway for butene dimerization over cobalt on carbon catalyst is shown in Figure 3.10. Schultz et al. proposed that a cobalt hydride species is the active catalytic site and mediates the olefin oligomerization [11]. Our methods of analysis of the catalyst show that the cobalt particles (surface and bulk) are principally composed of CoO and $Co_3O_4$. Demonstrating the presence of Co−H through direct characterization has thus far remained elusive. However, as suggested by recent studies on homogeneous cobalt complex catalysts for olefin oligomerization, cobalt hydride was frequently described as the active center generated upon activation of a Co(II) species [21]. Our proposed pathway is based upon our spectroscopic

---

[3] Since the time of publication, the proposed mechanism in this chapter is no longer believed to be the most accurate for olefin oligomerization over cobalt oxide on carbon. After revisiting product distributions, we believe the high linear composition can be explained by a Cossee-Arlman mechanism not oxidative coupling. Details on our revised prediction can be found in another publication:

Zhuoran Xu, Dongting Zhao, Joseph P. Chada, Devon C. Rosenfeld, Jessica L. Rogers, Ive Hermans, George W. Huber, Olefin Conversion on Nitrogen-doped Carbon-Supported Cobalt Catalysts: Effect of Feedstock, Journal of Catalysis, Volume 354, October 2017, pp 213-222.

characterization, catalytic performance, and kinetic data, especially the olefin product mixture. While the potential role of cobalt hydride species cannot be neglected and could be responsible for olefin isomerization, the classical Cossee olefin coordination, insertion, and β-H elimination pathway for 1-butene dimerization would produce 3-methylidene heptane and 3methylidene-4-methyl-hexane, which we do not observe [22]. Additionally, it would be expected that under high olefin concentration or fast kinetics for coordination and insertion, a Cossee pathway would produce a Schultz−Flory distribution of oligomers. The active site in our current study is thereby described as a Co oxide phase in general without further clarification, and the investigation of the active site would be a subject of future study.

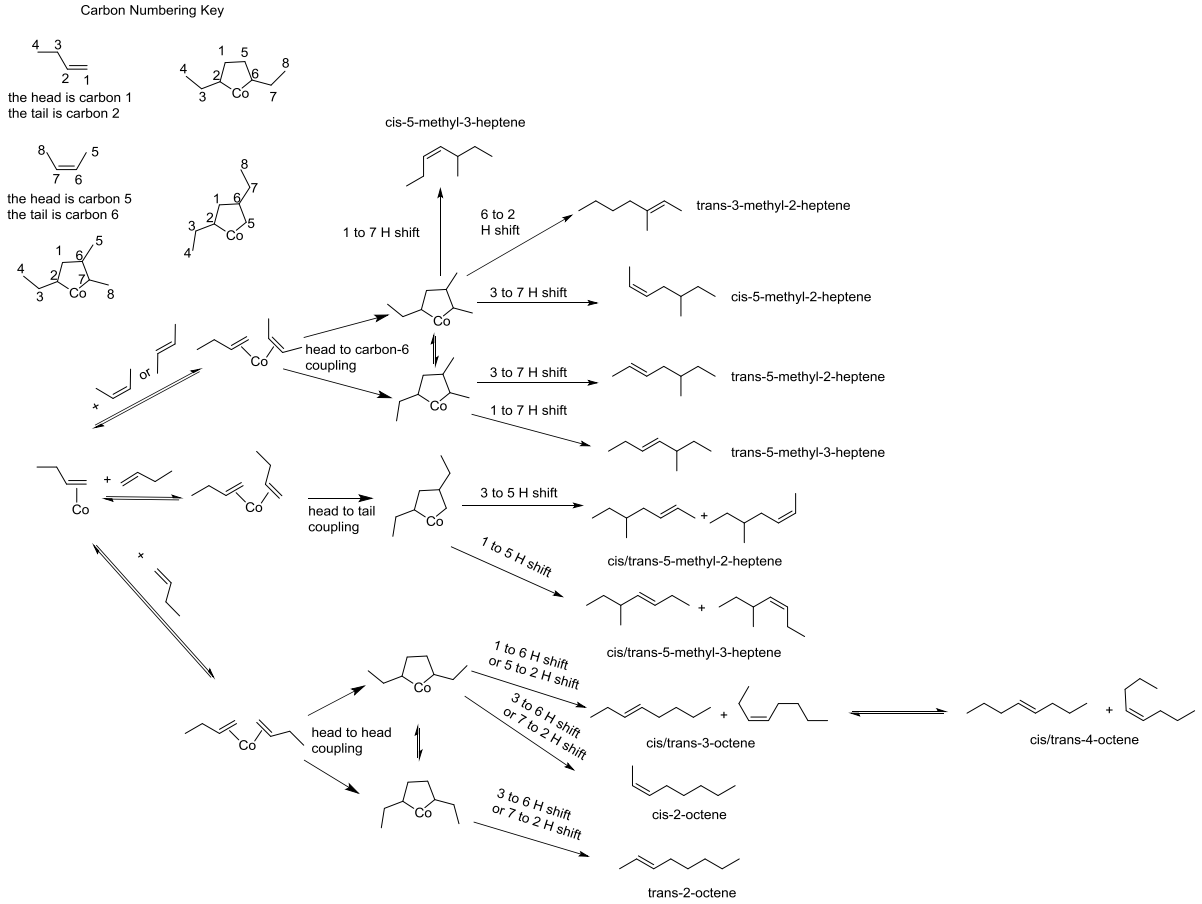


**Figure 3.10.** Proposed reaction pathway for butene coupling on cobalt oxide on carbon catalyst.

The first step in this mechanism is 1-butene adsorption onto the cobalt site. The adsorbed 1-butene can then undergo double-bond isomerization to form adsorbed *cis*-2-butene or *trans*-2-butene. As demonstrated in Figure 3.4, the distribution of 1-butene, *trans*-2-butene, and *cis*-2-butene is in equilibrium at longer residence times. Both 1-butene and 2-butene can be bonded to the cobalt center through σ-donating and π-accepting interactions between the olefin ligand and the metal, forming a stable metal−olefin complex [23]. Dimerization occurs via olefin oxidative coupling, forming a metallacyclopentane. Our cobaltacyclopentane-based pathway has precedence in selective ethylene trimerization and tetramerization mediated by chromium [24]. The dimerization can take place in the manner of either head-to-head or head-to-tail coupling, thus generating different $C_8$ olefin isomers. The metallacyclopentane then undergoes β-hydrogen shift followed by reductive elimination, yielding the corresponding $C_8$ olefins products, while recovering cobalt in its original oxidation state.

Linear octenes including cis/*trans*-3-octene and cis/*trans*-2-octene can be formed via head-to-head coupling of two 1-butenes. cis/*trans*-4-Octene can then be formed by double-bond shift from cis/*trans*-3-octene. Table S4.2 shows the experimental and equilibrium linear octene distribution. The equilibrium distribution of 1-octene is less than 0.83%, and no 1-octene could be detected in our product. The 3-octene and *cis*-2-octene are greater than their equilibrium composition at the lowest conversion, suggesting that these are the primary products produced by dimerization of the 1-butene. The *cis*-2-octene/*trans*-2-octene ratio is greater than the equilibrium calculated ratio. As residence time increases, the products move toward the equilibrium distribution but did not reach equilibrium.

It is proposed that the branched butene dimers including cis/*trans*-5-methyl-2-heptene and cis/*trans*-5-methyl-3-heptene can be produced in two ways: head-to-carbon-6 coupling between 1-

butene and 2-butene and head-to-tail coupling between two 1-butenes. We are currently unable to determine the extent to which the two pathways are operational. *trans*-3-Methyl-2-heptene, however, is exclusively produced from head-to-carbon-6 coupling between 1-butene and 2-butene. Table S3.3 shows the experimental and equilibrium distribution of the methylheptene species. The thermodynamic terminal-methyl-heptene distribution was less than 1%, and none of these species were detected in our experiments. The thermodynamic distribution of 3-methyl-3-heptene was 11.5%, and no 3-methyl-3-heptene was observed. This indicates that the catalyst cannot isomerize the double bond of the 3-methyl-2-heptene product. The ratio of cis/*trans*-5-methyl-3-heptene was 3 times higher than the equilibrium composition, but this ratio went toward equilibrium as residence time increased. The ratio of cis/*trans*-5-methyl-2heptene was 10 times higher than the equilibrium ratio but decreased to 3 times with increasing residence time. The ratios of *cis*-5-methyl-3-heptene/*cis*-5-methyl-2-heptene and *trans*-5-methyl-3-heptene/*trans*-5-methyl-2-heptene were 30% and 60% higher than their equilibrium values at the highest conversion, respectively.

The abundance of linear octene isomers in the product mixture and the low abundance of 1-butene in the product gas indicate that the reaction between two terminal olefins is faster than the reaction between an internal olefin and a primary olefin. The equilibrium ratio between a primary and internal olefin decreases with increasing size of the olefin. For example, the equilibrium concentration of 1-butene in butene isomers is 6.2% while the equilibrium concentration of 1-heptene is less than 0.8%. The absence of $C_{16}$ and longer olefin products further suggests that the extended chain growth after butene dimerization is prohibited because of the low 1-octene concentration in the mixture and that the coupling between two internal olefins does not occur. Such features imply that cobalt oxide on carbon catalyst is highly selective for terminal

olefin coupling and could be used as a potential catalyst to make internal linear oligomers with a targeted carbon chain length. Additional studies are underway to enhance our understanding of the active site and transient species.

## 3.4 Conclusions

Cobalt oxide on carbon catalysts have greater than 80% selectivity toward linear octenes for 1-butene oligomerization. The 1-butene undergoes double-bond isomerization to form an equilibrium mixture with *trans*- and *cis*-2-butene at high conversion. The main linear oligomers from butene conversion with a decreasing order of distribution are 3-octene > 2-octene > 4-octene. These internal linear octenes are formed from head-to-head coupling of two 1-butene molecules. The linear octenes approach equilibrium with increasing conversion. All the methyl-heptene products can be formed through head-to-tail coupling of two 1-butene molecules. trans/*cis*-5-Methyl-2-heptene and trans/*cis*-5-methyl-3-hetptene can also be formed through the coupling between 1-butene and 2-butene molecules. The activity of the catalyst increases with increasing $Co_3O_4$ content. The cobalt composition change was monitored by in situ Raman and TGA, which shows that cobalt nitrate fully decomposes at about 200°C and forms overlapped $Co_3O_4$ and CoO particles, as shown in the XANES, XRD, and HRTEM results. XANES results confirm that high pretreatment temperature (550°C) in helium partially reduced the cobalt oxide to metallic cobalt, with a decreasing $Co_3O_4$ content. The cobalt oxide on carbon catalysts reported in this chapter are highly selective for terminal olefin coupling and can be used to make internal linear oligomers with a targeted carbon chain length.

## 3.5 Supporting Information

**Table S3.1.** Mass and heat transfer evaluation.

| | Formula | Computed Values | | Target |
|---|---|---|---|---|
| | | 14.14 $h^{-1}$ WHSV | 0.71 $h^{-1}$ WHSV | |
| Interphase heat | $\frac{\lvert\Delta H\rvert r''' r_p}{hT_b} < 0.15\ \frac{RT_b}{E}$ | $7.8\times10^{-3}$ | $1.0\times10^{-4}$ | $<1.1\times10^{-2}$ |
| Interparticle heat | $\frac{\lvert\Delta H\rvert r''' r_p^2}{k_e T_w} < 0.4\ \frac{RT_w/E}{\left[1+8\left(\frac{r_p}{R_0}\right)Bi_w\right]}$ | $1.4\times10^{-2}$ | $1.8\times10^{-4}$ | $<1.6\times10^{-2}$ |
| Intraparticle heat | $\frac{\lvert\Delta H\rvert r''' r_p^2}{\lambda T_s} < 0.75\ \frac{RT_s}{E}$ | $1.4\times10^{-2}$ | $1.8\times10^{-4}$ | $<3.1\times10^{-2}$ |
| Interphase mass | $\frac{r_{obs} R_p}{C_B k_D}$ | $1.1\times10^{-5}$ | $1.4\times10^{-7}$ | <0.15 |
| Intraparticle mass | $\frac{r_{obs} R_p^2}{C_s D_{eff}}$ | 0.4 | $5.3\times10^{-3}$ | <0.6 |

**NOMENCLATURE**

$\Delta H$-heat of reaction
$r'''$-rate per catalyst volume
$r_p$-radius of particles
$T_b$-bulk fluid temperature
$h$-convective heat transfer coefficient
$k_e$-effective thermal conductivity
$\lambda$-effective thermal conductivity
$Bi$-Biot number
$E$-activation energy
$R_p$-radius of particles
$C_B$-concentration in bulk fluid
$C_S$-concentration at catalyst surface
$k_D$-mass transfer coefficient
$D_{eff}$-effective diffusivity

**Table S3.2.** Experimental and equilibrium linear octene distribution (Reaction condition: 80°C, 450 psig).

| | 2A-Co/C-230 | | | Equilibrium |
|---|---|---|---|---|
| **WHSV($h^{-1}$)** | 14.14 | 0.71 | 0.25 | |
| Conversion (%) | 9.77 | 11.42 | 29 | |
| 1-octene | 0 | 0 | 0 | 0.83 |
| *cis*-2-octene | 14.61 | 9.16 | 8.81 | 8.49 |
| *trans*-2-octene | 21.02 | 25.42 | 25.29 | 35.25 |
| cis/*trans*-3-octene | 62.83 | 58.58 | 56.07 | 34.76 |
| cis/*trans*-4-octene | 1.54 | 6.84 | 9.83 | 20.67 |
| *cis*-2-octene/*trans*-2-octene | 0.69 | 0.36 | 0.35 | 0.24 |

**Table S3.3.** Experimental and equilibrium methyl-heptene distribution (Reaction condition: 80°C, 450 psig).

| | 2A-Co/C-230 | | | Equilibrium |
|---|---|---|---|---|
| **WHSV($hr^{-1}$)** | 14.14 | 0.71 | 0.25 | |
| Conversion (%) | 9.77 | 11.42 | 29 | |
| *cis*-5-methyl-3-heptene | 10.9 | 9.8 | 8.3 | 3.4 |
| *trans*- 5-methyl-3-heptene | 12.2 | 11.1 | 12.5 | 14.4 |
| *trans*-3-methyl-2-heptene | 21.2 | 43.6 | 44.4 | 33.0 |
| *trans*-5-methyl-2-heptene | 16.7 | 17.8 | 19.9 | 29.4 |
| *cis*-5-methyl-2-heptene | 39.1 | 17.8 | 14.8 | 7.0 |
| 3-methyl-3-heptene | 0 | 0 | 0 | 11.5 |
| 4-methyl-1-heptene | 0 | 0 | 0 | 0.7 |
| 3-methyl-1-heptene | 0 | 0 | 0 | 0.5 |
| *cis*/*trans* -5-methyl-3-heptene | 0.89 | 0.88 | 0.67 | 0.24 |
| *cis*/*trans* -5-methyl-2-heptene | 2.35 | 1.00 | 0.74 | 0.24 |
| *cis*-5-methyl-3-heptene/*cis*-5-methyl-2-heptene | 1.85 | 0.41 | 0.33 | 0.21 |
| *trans*-5-methyl-3-heptene/*trans*-5-methyl-2-heptene | 0.73 | 0.63 | 0.63 | 0.49 |

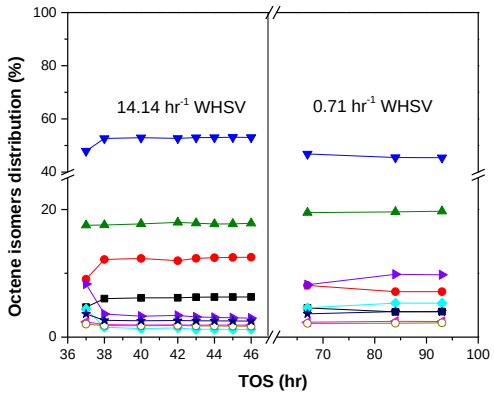


**Figure S3.1.** Octene isomers distribution with time on stream over 2A-13%Co/C-230, including: (▼) *trans*-3-octene, (▲) *trans*-2-octene, (●) *cis*-2-octene, (■) *cis*-5-methyl-2-heptene, (►) 3-methyl-2-heptene, (◆) *trans*-4-octene, (◄) *trans*-5-methyl-3-heptene, (○) *cis*-5-methyl-3-heptene and (★) *trans*-5-methyl-2-heptene at 80℃ and 450 psig.

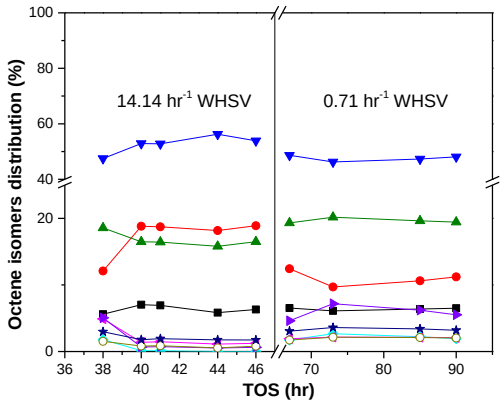


**Figure S3.2.** Octene isomers distribution with time on stream over 2NaOH-13%Co/C-230, including: (▼) *trans*-3-octene, (▲) *trans*-2-octene, (●) *cis*-2-octene, (■) *cis*-5-methyl-2-heptene, (►) 3-methyl-2-heptene, (◆) *trans*-4-octene, (◄) *trans*-5-methyl-3-heptene, (○) *cis*-5-methyl-3-heptene and (★) *trans*-5-methyl-2-heptene at 80℃ and 450 psig.

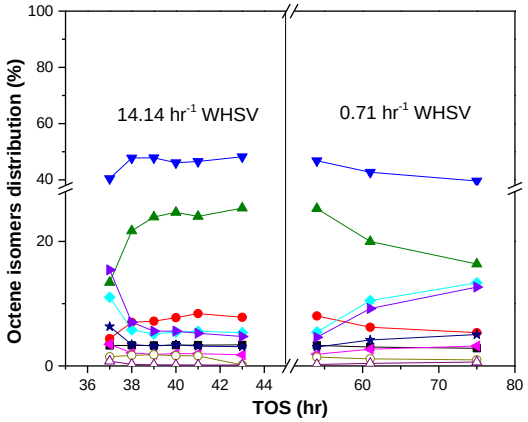


**Figure S3.3.** Octene isomers distribution with time on stream over 2A-13%Co/C-350, including: (▼) *trans*-3-octene, (▲) *trans*-2-octene, (●) *cis*-2-octene, (■) *cis*-5-methyl-2-heptene, (►) 3-methyl-2-heptene, (◆) *trans*-4-octene, (◄) *trans*-5-methyl-3-heptene, (○) *cis*-5-methyl-3-heptene and (★) *trans*-5-methyl-2-heptene at 80℃ and 450 psig.

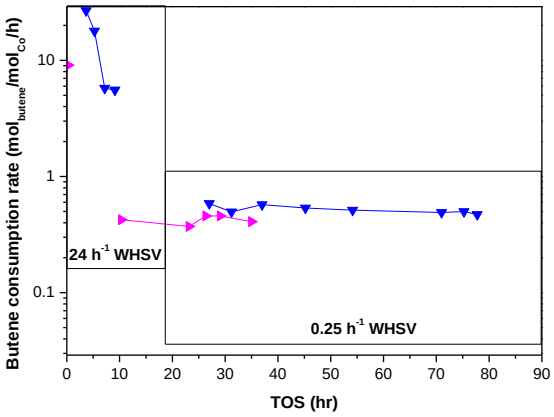


**Figure S3.4.** Catalyst activity for (▼) 2A-Co/C-230 and (►) 2A-Co/C-270 vs TOS at 24 $h^{-1}$ and 0.25 $h^{-1}$ WHSV.

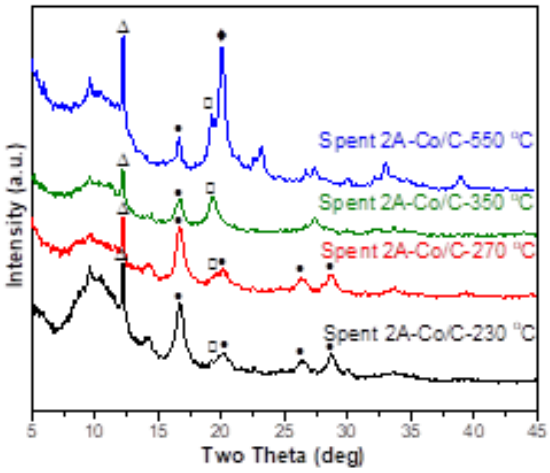


**Figure S3.5.** Mo-XRD patterns of the spent catalysts, with characteristic peaks of ∆graphite, ●$Co_3O_4$, □CoO, ◆Cubic Co.

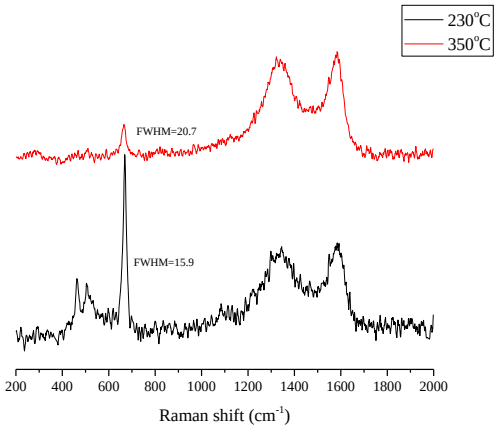


**Figure S3.6.** Comparison of CoOx signal at 690 $cm^{-1}$ during pretreatment at 230ºC and 350ºC.

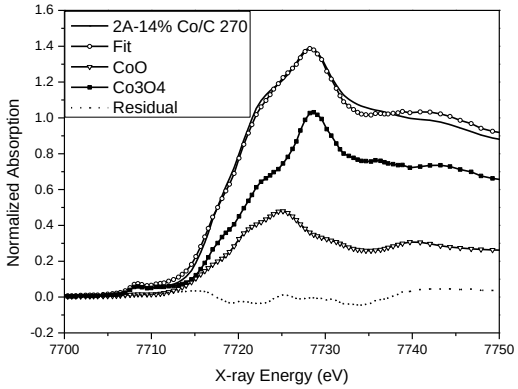


**Figure S3.7.** Fitted XANES spectra for 2A-13% Co/C-270 showing weighed spectra, linear combination fit, and residual difference between the fit and data.

## 3.6 References


1. Gas Technology Institute. Pipeline Gas J. 2013, 240 3.
2. Benardo Fallas, P. P. Platts Special Report: Petrochemicals; Platts, 2013.
3. Bollmann, A.; Blann, K.; Dixon, J. T.; Hess, F. M.; Killian, E.; Maumela, H.; McGuinness, D. S.; Morgan, D. H.; Neveling, A.; Otto, S.; et al. J. Am. Chem. Soc. 2004, 126, 14712−14713.
4. (a) Keim, W. Angew. Chem., Int. Ed. 2013, 52, 12492−12496.
5. (b) Sinn, H.; Kaminsky, W. Adv. Organomet. Chem. 1980, 18,99−149.
6. (a) Broene, R. D.; Brookhart, M.; Lamanna, W. M.; Volpe, A. F. J.
7. Am. Chem. Soc. 2005, 127, 17194−17195. (b) Small, B. L.; Brookhart, M. J. Am. Chem. Soc. 1998, 120, 7143−7144.
8. (a) Zhang, J.; Yan, Y.; Chu, Q.; Feng, J. Fuel Process. Technol. 2015, 135,2−5. (b) Kim, Y. T.; Chada, J. P.; Xu, Z.; Pagan-Torres, Y. J.; Rosenfeld, D. C.; Winniford, W. L.; Schmidt, E.; Huber, G. W. J. Catal. 2015, 323,33−44. (c) Bjørgen, M.; Lillerud, K.-P.; Olsbye, U.; Bordiga, S.; Zecchina, A. J. Phys. Chem. B 2004, 108, 7862−7870. (d) Quann, R. J.; Green, L. A.; Tabak, S. A.; Krambeck, F. J. Ind. Eng. Chem. Res. 1988, 27, 565−570. (e) Knifton, J. F.; Sanderson, J. R.; Dai, P. E. Catal. Lett. 1994, 28, 223−230. (7) (a) Franken, J.; Kirschhock, C. E.; Mathys, G. M.; Martens, J. A. ChemCatChem 2012, 4, 1245−1248. (b) Beltrame, P.; Forni, L.; Talamini, A.; Zuretti, G. Appl. Catal., A 1994, 110,39−48.
9. Chauvin, Y.; Commereuc, D.; Hugues, F.; Thivolle-Cazat, J. Appl. Catal. 1988, 42, 205−216.
10. Neuhofen, F. M.; Weinheim, P. P. U.S. Patent 5849972, 1998.
11. (a) Qiu, J.; Zhang, H.; Liang, C.; Li, J.; Zhao, Z. Chem. - Eur. J. 2006, 12, 2147−2151. (b) Xing, L.; Qiu, J.; Liang, C.; Wang, C.; Mao, L. J. Catal. 2007, 250, 369−372. (c) Zhang, P.; Yu, C.; Fan, X.; Wang, X.; Ling, Z.; Wang, Z.; Qiu, J. Phys. Chem. Chem. Phys. 2015, 17, 145− 150. (d) Wang, C.; Qiu, J.; Liang, C.; Xing, L.; Yang, X. Catal. Commun. 2008, 9, 1749−1753.
12. (a) Schultz, R. G.; Schuck, J.; Wildi, B. J. Catal. 1966, 6, 385− 396. (b) Schultz, R. G.; Engelbrecht, R. M.; Moore, R. N.; Wolford, L. T. J. Catal. 1966, 6, 419−424.
13. Alberty, R. A.; Gehrig, C. A. J. Phys. Chem. Ref. Data 1985, 14,
14. 803−820.
15. Shabaker, J.; Davda, R.; Huber, G.; Cortright, R.; Dumesic, J. J. Catal. 2003, 215, 344−352.
16. Toch, K.; Thybaut, J.; Marin, G. Appl. Catal., A 2015, 489, 292− 304.
17. Perry, H. R.; Green, D. W.; Maloney, J. O. In Perry's Chemical Engineers' Handbook, 7th ed.; The McGraw-Hill Companies, Inc.: New York, 2008; Vol. 796, pp 5-48−5-54.
18. Carrero, C. A.; Keturakis, C. J.; Orrego, A.; Schomäcker, R.; Wachs, I. E. Dalton Transactions 2013, 42, 12644−12653.
19. Lee, J.; Burt, S. P.; Carrero, C. A.; Alba-Rubio, A. C.; Ro, I.;
20. O'Neill, B. J.; Kim, H. J.; Jackson, D. H.; Kuech, T. F.; Hermans, I.; et al. J. Catal. 2015, 330,19−27.

21. Tang, C.-W.; Wang, C.-B.; Chien, S.-H. Thermochim. Acta 2008,
22. 473,68−73.
23. (a) Keely, W.; Maynor, H. W. J. Chem. Eng. Data 1963, 8, 297− 300. (b) Makhlouf, M. Th.; Abu-Zied, B. M.; Mansoure, T. H. J. Nanopart. 2013, 2013, 384350.
24. Cseri, T.; Bekassy, S.; Kenessey, G.; Liptay, G.; Figueras, F. Thermochim. Acta 1996, 288, 137−154.
25. (a) Tellmann, K. P.; Gibson, V. C.; White, A. J.; Williams, D. J. Organometallics 2005, 24, 280−286. (b) Sun, W.-H.; Hao, P.; Zhang, S.; Shi, Q.; Zuo, W.; Tang, X.; Lu, X. Organometallics 2007, 26, 2720− 2734.
26. Small, B. L.; Schmidt, R. Chem. - Eur. J. 2004, 10, 1014−1020.
27. Hartwig, J. F. In Organotransition Metal Chemistry: From Bonding to Catalysis; Edwards Brothers, Inc.: Sausalito, CA, 2010; p 47.
28. Agapie, T. Coord. Chem. Rev. 2011, 255, 861−880.

# Chapter 4. Oligomerization of 1-butene over carbon-supported $CoO_x$ and subsequent isomerization/ hydroformylation to n-nonanal[4]

## 4.1 Introduction

Light olefins ($C_2$-$C_4$) are precursors for numerous chemicals in the petrochemical industry. Recent increases in the supply of ethane from natural gas extraction has stimulated research in processes for the conversion of light olefins towards fuels and value-added chemicals. Oligomerization represents one potential route for valorising these light olefins to produce longer-chain oligomers such as linear alpha olefins (LAOs) or transportation fuels [1,2]. LAOs have significantly higher value than fuels due to their application as co-monomers for linear low-density plastics production and as precursors for the lubricant, surfactant and detergent industry. Several efforts have focused on identifying selective heterogeneous catalysts for oligomerization to compete with homogeneous catalysts [3,4]. One major limitation of current heterogeneous oligomerization catalysts is the limited uses for reaction side products, which include branched and internal olefin isomers. The ability to employ a heterogeneous oligomerization catalyst to selectively upgrade light olefins to value-added chemicals would be desirable. Common catalysts for commercial

---

[4] This chapter was adapted with permission from: Joseph P. Chada, Zhuoran Xu, Dongting Zhao, Rick B. Watson, Mick Brammer, Marinus Bigi, Devon C. Rosenfeld, Ive Hermans, and George W. Huber, Oligomerization of 1-butene over carbon-supported $CoO_x$ and subsequent isomerization/ hydroformylation to n-nonanal, Catal. Commun., 114 (2018) 93-97.

Author contributions: J.P.C., D.C.R. and G.W.H designed research; J.P.C performed oligomerization reactions and catalyst characterization; R.B.W., M.B., and M. Bigi performed hydroformylation reactions; J.P.C. and G.W.H. wrote the paper; and Z.X, D.Z., and I.H. aided in cobalt oxide catalyst discovery.

oligomerization processes include homogeneous systems such as a nickel-phosphine complex used in the Shell Higher Olefin Process (SHOP) process [5], or triethyl aluminum Ziegler catalysts used in the INEOS and Gulf process [6]. Known heterogeneous olefin oligomerization catalysts include many forms of solid acids and supported metals and metal oxides [7]. It is well known that Brønsted acids can be used to produce gasoline-range fuels, but the rapid skeletal isomerization leads to a highly-branched product distribution [8,9]. Recently, many authors have identified Ni-based catalytic systems as potential candidates for the heterogeneous oligomerization of ethylene. A few examples include Ni-exchanged $SiO_2$-$Al_2O_3$ [10,11], zeolites [12-14] and MOF frameworks [15,16]. While these Ni-based systems produce linear oligomers from 1-butene oligomerization, the highest reported yields were approximately 10% [11].

A series of publications by Schultz et al. [17,18] highlighted the exceptional linear selectivity of a "doubly-ammoniated cobalt oxide on carbon" catalyst for the oligomerization of light olefins. Recently, our group has reported on a heterogeneous, ammonia-treated carbon-supported cobalt oxide catalyst (2A-$CoO_x$/N-C) based on the work of Schultz et al. [19-21] that is capable of oligomerizing 1-butene to straight-chain dimers with high selectivity (82.9%) with the remainder of the dimerization products consisting entirely of mono-branched olefins. To the best of our knowledge, 2A-$CoO_x$/NC is the most selective heterogeneous catalyst for the dimerization of light olefins into linear oligomers. While selectivity towards straight-chain oligomers is high, double-bond isomerization is facile and oligomerization products approach thermodynamic equilibrium

with internal $C_8$ olefins being the primary oligomers and only trace amounts of terminal $C_8$ olefin produced.

In this chapter, we demonstrate how the oligomers produced from the 2A-CoOx/N-C[5] catalyst can be selectively converted into linear $C_9$ aldehydes with a tandem isomerization/hydroformylation catalyst as shown in Figure 4.1 [22-24]. We expect that this technology could be combined with other olefins ($C_nH_{2n}$, where n=2-6) [25] to produce the corresponding linear aldehyde ($C_{2n+1}$+$H_{4n}$+O) of the dimerization product. The analyzed route from light olefins to longer-chain aldehydes could be further coupled with other reactions such as hydrogenation, oxidation or reductive amination to produce alcohols, carboxylic acids or amines of different functionalities, respectively [26]. Specifically, $C_8$ and $C_9$ oxo alcohols are used in plasticizers for polyvinylchloride (PVC) production [7].

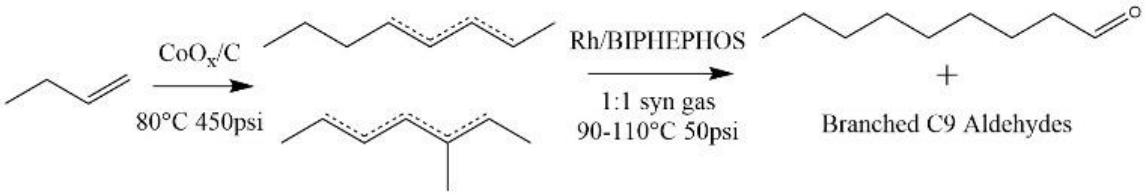


**Figure 4.1.** Catalytic reaction route to produce n-nonanal from 1-butene by first oligomerizing the terminal olefin to an equilibrium mixture of linear and mono-branched isomers followed by the tandem isomerization/hydroformylation to the corresponding aldehyde. Double-bond positions of the major $C_8$ products are shown as dotted lines. Branched C9 aldehydes were not drawn for simplicity but reported in the Supporting Information (SI) (see Table S4.1).

[5] The catalyst naming convention for Chapter 4, "2A-CoOx/N-C" represents the same ammonia-treated catalyst "2A-Co/C" originally described in Chapter 3. The change in terminology in our published articles after 2016 was made for clarity and consistency amount all published works.

## 4.2 Experimental

Relevant information about instrumental analysis of reaction products and catalyst characterization is provided in the Supporting Information (Section 5.5).

### 4.2.1 Catalyst preparation

Oligomerization catalysts were prepared by the incipient wetness impregnation (IWI) of 4.2M cobalt nitrate solution on an activated carbon support (Norit Darco MRX) to obtain a loading of ~12 wt.% cobalt. Detailed synthesis and characterization of this catalyst are reported elsewhere [20]. After IWI, the catalyst was dried at 125°C in air.

Hydroformylation catalyst solutions were prepared in a nitrogen glove box with Schlenk techniques. Anhydrous solvents and BIPHEPHOS (Sigma-Aldrich) were used as received. For each reaction, rhodium dicarbonyl acetylacetonate (0.0178 g; 250 ppm Rh) and BIPHEPHOS (0.1623 g, 3 moles/mole Rh) are combined with the solvent (30 mL); 1 mL tetraglyme (≥99%) was added as internal standard for GC analyses.

### 4.2.2 Catalytic measurement

Catalytic oligomerization reaction studies were carried out in a fixed bed up-flow reactor. Details of the experimental setup are described elsewhere [20]. Prior to reaction, the catalyst was pre-treated in flowing helium (100 mL/min) at 230°C (5°C/min ramp, 2 h hold). The reactor was then cooled to reaction temperature, pressurized to 450 psig with He, then 1-butene (99.9%) was flowed via a high-pressure syringe pump (Teledyne Isco). Liquid-phase reaction products were collected and drained from a chilled collection vessel placed after the reactor into a chilled n-hexane solution with a n-heptane internal standard. Products were analyzed by 2D-GC-MS system. $C_4$ isomerization products were analyzed by sampling a He sweep gas flowing through the

headspace of the collection vessel at the exit of the reactor with GC (Figure S4.1, SI). The skeletal composition of the $C_8$ isomers products was determined by GC analysis of the hydrogenated liquid products. Reaction mixtures were hydrogenated with the H2 carrier gas of the GC passed over a Pd/C catalyst packed in the GC liner. Reaction products collected for hydroformylation experiments were distilled to produce a feed that consisted of primarily C8 olefins (4% C4, 94.2% C8, 1.8% C12). GC conditions can be found in Table S5.2 (SI).

For hydroformylation reaction studies, catalyst solutions were charged to the reactor and heated to the reaction temperature with stirring under a ~ 50 psig gaseous mixture of H2 and CO with a molar ratio of 1:1 (syngas) for 30 min. The mixed C8 olefin was then added via pressurelok syringe (3 mL). A charge sample was taken for GC and target reaction pressure was established with 1:1 syngas (CO/H2). The pressure was held constant by using Brooks 5150 mass flow meters. Gas uptake was measured with a Brooks totalizer. Samples were taken periodically for GC analysis to determine conversion and product selectivity. The total reaction time was set to 6 h.

### 4.2.3 Scanning transmission electron microscopy (STEM)

STEM images were obtained with an aberration-corrected FEI Titan microscope. Catalyst samples were suspended in ethanol with sonication then deposited on a carbon-coated copper grid (EMS) and plasma cleaned for 15 min prior to analysis with an aberration-corrected FEI Titan STEM.

## 4.3 Results and Discussion

### 4.3.1 Oligomerization process step

In the first step of this process, 1-butene was converted in a flow reactor over 2A-$CoO_x$/N-C catalyst. This catalyst is active for both the isomerization of 1-butene to its internal double-bond

stereoisomers and for the oligomerization to longer chain lengths without the addition of a co-catalyst. The ability to operate without a co-catalyst activator, such as methylaluminoxane (MAO), represents a significant processing advantage as both homogeneous and heterogeneous catalytic oligomerization systems commonly employ these pyrophoric materials in stoichiometric excess to alkylate the active metal sites and initiate the catalytic cycle [27]. Figure 4.2A shows the rate of isomerization, oligomerization and linear octene distribution as a function of time. The 1-butene conversion to oligomers in these experiments was between 2-10%. An analysis of the detailed dimerization product composition as a function of conversion can be found elsewhere [19]. At the chosen reaction conditions, catalyst deactivation resulted in the simultaneous decrease in isomerization and oligomerization activity. We suspect that both isomerization and oligomerization occur on the same catalytic site, as the deactivation profile is identical for each reaction regardless of WHSV. From surface area measurements, Xu et al. [21] proposed that deactivation can be attributed to either pore filling of the carbon support or accumulations of heavy oligomers on the active sites. Nanoparticle sintering and leaching were ruled out by small-angle x-ray scattering (SAXS) and elemental chemical analysis (ICP) of the fresh and spent catalysts. Control experiments showed minimal isomerization activity (<5%) and no oligomerization activity on the ammonia-treated carbon support. Regeneration in an inert atmosphere was tested and partially recovers some of the lost activity. The investigation of additional methods for reducing catalyst deactivation, such as removal of oligomers from the spent catalyst or support pore modification in order to increase the transport of heavy oligomers out of the catalyst pore system, remains an important topic for future studies.

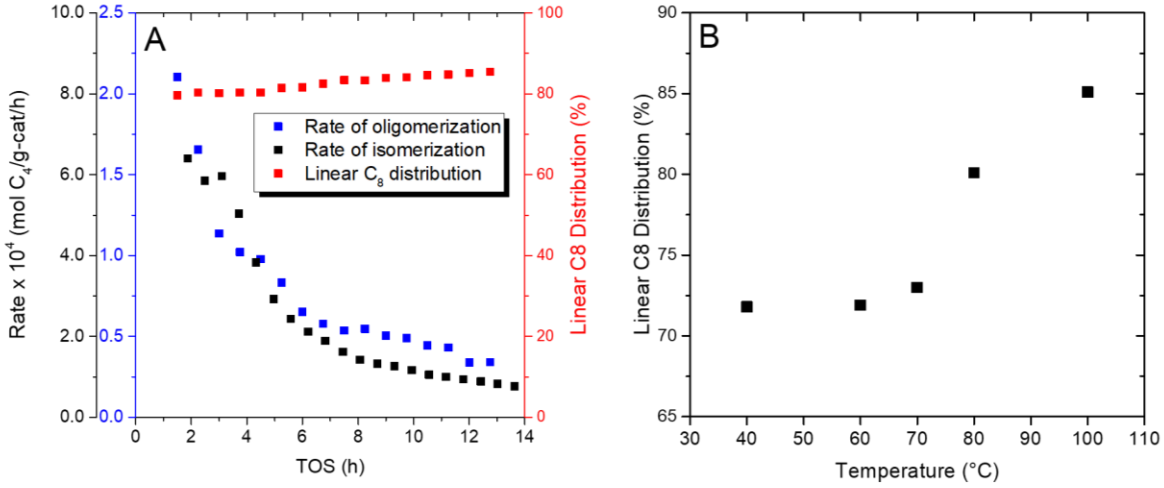


**Figure 4.2.** Catalytic performance of A-CoOx/N-C for A) 1-butene isomerization and oligomerization as a function of time on stream (TOS) at 80˚C and B) Linear octene distribution of dimerization products as a function of temperature. Reaction conditions: 450 psi; WHSV1-butene=5 h-1; 15 mL He sweep gas.

Work by Xu et al. [21] which analyzed product compositions from various starting molecules suggested that oligomerization over 2A-$CoO_x$/N-C occurs via a Cossee-Arlman mechanism, where the catalytic cycle is characterized by an initial insertion step of the olefin into a metal hydride followed by successive olefin insertion steps. The active metal hydride is regenerated by β-hydride elimination. Double-bond isomerization of both 1-butene and the oligomer products occurs concurrently through the reversible insertion/elimination into the metal hydride bond. It is noteworthy that no activation period was observed with our system. Recently, a DFT study by Brogaard and Olsbye [12] analyzed the most probable mechanisms for oligomerization and active site formation in Ni-containing aluminosilicates. From an analysis of free-energy profiles, they concluded that a Cossee-Arlman mechanism was the most probable pathway starting with a $[Ni(II)\text{-ethylene-H}]^+$ species. Similar to our study, the systems studied [12] did not require a co-catalyst to induce catalytic activity. The authors were also able to show

that the initial Ni alkyl formation would have reasonable barriers of 100 kJ/mol or less and proposed several plausible pathways [12]. A recent work by Moussa et al. [14] proposed that the active site for ethylene oligomerization on Ni-Beta can be attributed to $Ni^{2+}$ cations grafted to acidic silanols, which they were carefully characterized via temperature-resolved FTIR and simultaneous mass spectroscopy. They propose the formation of nickel vinyl hydride intermediates which form a catalytic cycle similar to the Cossee-Arlman mechanism. Experimental studies by Mlinar et al. [15] on propylene oligomerization using Ni-MOF materials showed consistent results as the activity was increased during the first 50 min on TOS, which were attributed to the propylene molecules migrating to and coordinating with isolated Ni(II) species.

The distribution of linear dimerization products is nearly constant even with the loss of more than 80% of the initial isomerization and oligomerization activity (Figure 4.2A). As activity declines, the average 1-butene molar concentration over the catalyst bed increases from 73.9% to 96.5%. The production of both linear dimers (formed from 2,1 insertion of 1-butene into a cobalt n-alkyl) and 2-butene (formed from β-hydride elimination of a cobalt iso alkyl) provides evidence that both n-alkyl and iso-alkyls are present on the catalyst surface. The exceptional linear selectivity of this catalyst can potentially be explained by differences in the relative stabilities of the surface alkyl intermediates (Figure 4.3). Metzger et al. [16] was able to show with DFT calculations that the primary alkyl is more stable than the secondary alkyl by 3.5 kcal/mol for 1,6-heptadiene insertion into a Ni-H bond of a Ni-MFU-4l ethylene oligomerization catalyst. The stability of the cobalt alkyl can be expected to affect either the relative ratio of primary as opposed to secondary alkyls or the relative rate of 2,1-insertion into the metal n-alkyl bond vs secondary reactions.

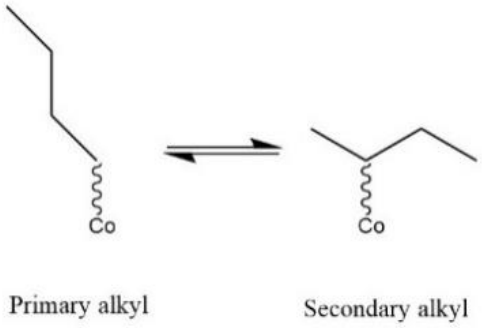


**Figure 4.3.** Surface cobalt butyl isomers.

Another notable observation was the effect of reaction temperature on the selectivity to linear products (Figure 4.2B). The linear dimer distribution (compared to mono-branched dimers) increases with increasing temperature at the expense of decreased reaction rate (Figure S4.2, SI). At 100°C, an average linear dimer selectivity of 85.1% was achieved. To our knowledge, this is the highest selectivity reported for the oligomerization to linear octenes over a heterogeneous catalyst. The decrease in reactivity at higher temperatures can be explained by the increased rates of deactivation, assumed to be due to heavy hydrocarbon accumulation during the first few hours' time on stream. Even though it was found that C8 linear olefin oligomerization product was the most abundant and stable at 70°C (Figure S4.2), oligomer products were collected for upgrading at 80°C (due to the amount collected at that temperature in previous work on this system) [19-21]. At all temperatures tested, there was no evidence for cracking or other side reactions. Two explanations for the observed increase in linear selectivity are: i) the ratio of primary vs secondary metal alkyl intermediates increases with temperature, or ii) the reaction step for 2,1-insertion into n-butyl species (the mechanism for linear oligomer formation) is associated with a higher activation energy than the undesired branched-oligomer forming steps, and thus increases at higher

temperatures. Without a method of quantifying surface metal butyl species or estimating the individual rates of 2,1 vs 1,2 insertion, it is not possible to distinguish between these possibilities.

As shown by Xu et al. [19] with the use of x-ray absorption spectroscopy (XAS), 2A $CoO_x$/N-C consists of a mixture of $Co^{2+}$ and $Co^{3+}$ metal oxidation states. From scanning transmission electron microscopy images (STEM) shown in Figure 4.31, the $CoO_x$ particles are present as 2-10 nm particles. We have found that compared to other support materials ($Al_2O_3$, $SiO_2$, $TiO_2$), carbon favors the formation of the smallest cobalt oxide particles. It has been shown by several sources that metallic cobalt particle size is influenced by the pore structure and interaction with the support material [28]. The carbon support used in this study was reported to have a wide distribution of pore sizes ranging from 0.4-100 nm [29]. It appears that the support interactions resulting in the formation of the smallest metal particles may also play an important role in the formation of the proposed cobalt hydride species, as cobalt oxide catalysts supported on other materials do not show any appreciable oligomerization activity. However, the possibility of an electronic effect between the metal and support cannot be excluded. With the heterogeneity of metal nanoparticles it is plausible that the number of active sites is significantly less than the amount of surface cobalt species.

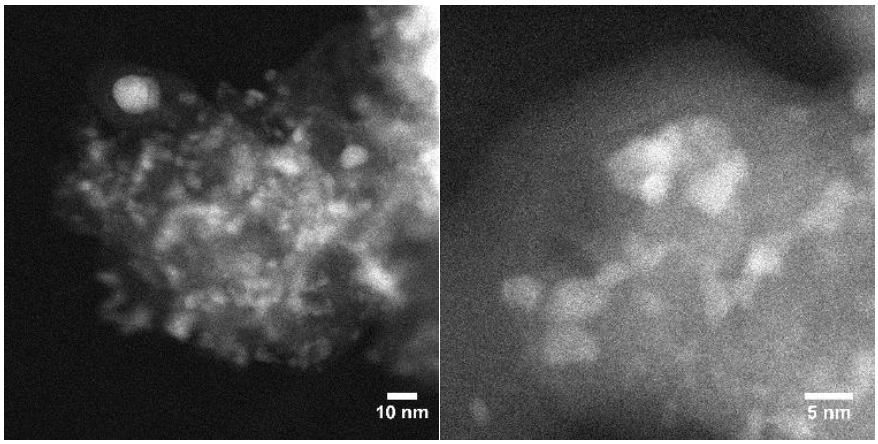


**Figure 4.45.** STEM-HAADF of 2A-$CoO_x$/N-C.

As mentioned above, oligomerization product distributions are consistent with a Cossee-Arlman mechanism in which the probability of chain growth can be predicted by a Schulz-Flory distribution, assuming the probability of monomeric addition is not a function of chain length. Like most industrial processes, this catalyst produces a broad range of molecular weights which limits the maximal yield of a desired chain length. Ideally, a process optimized for dimerization would operate at low conversions to minimize the production of unwanted long-chained oligomers. The rapid double-bond isomerization and constant linear oligomerization selectivity of the 2A-$CoO_x$/N-C catalyst (Fig 5.1A) could potentially be used to process impure C4 streams commonly available at refineries such as raffinate-3 (mixture of n-butane, 1- and 2-butenes).

### 4.3.2 Hydroformylation process step

The second step of the process involves the isomerization-hydroformylation of the olefinic product mixture over a homogeneous catalyst. Prior to reaction, the oligomerized product was distilled to isolate a mixture consisting primarily of $C_8$ olefins to simplify hydroformylation product analysis. To date, complexes of rhodium and cobalt remain the only two industrially-relevant systems. A mononuclear $Rh(CO)_2(acac)$ catalyst combined with a chelating bisphosphite

ligand (BIPHEPHOS) (Figure 5), originally patented by Union Carbide Corporation (UCC) [24], was chosen since Rh catalysts are significantly more active than cobalt and benefit from reduced reaction pressure and temperature requirements.

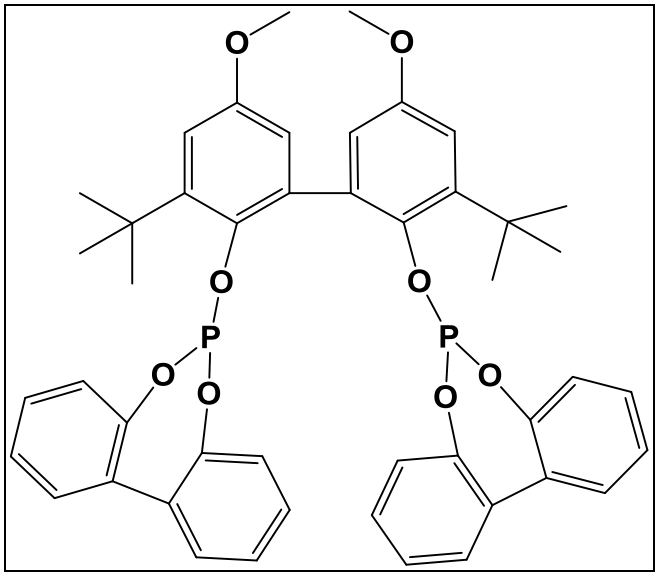


**Figure 4.5.** BIPHEPHOS chelating ligand for hydroformylation reaction.

The sterically-hindered BIPHEPHOS ligand was designed in the 1980s to enhance the regioselectivity of propene hydroformylation and has since been demonstrated to selectively convert (E/Z)-2-pentene to n-hexanal with a yield of 79% and a linear selectivity of 99% [23,26]. Additionally, Behr et al. [22] was able to convert *trans*-4-octene to n-nonanal with a yield of 88%. Isomerization-hydroformylation results (Table 4.1) confirm that the oligomerization products can be converted to linear aldehydes, while maintaining high regioselectivity towards normal vs isoaldehyde products, typical represented as the ratio N:I. A detailed analysis of the hydroformylation feed and product mixture can be found in Table S4.1 (SI). The isomerization-hydroformylation conditions presented in this chapter were not optimized due to the limited quantities of olefinic mixtures produced in lab-scale reactors for the oligomerization reaction. The

combined oligomerization/hydroformylation results presented here serve as a proof-of-concept that the production of primarily linear internal olefins with 2A-$CoO_x$/N-C catalyst could be combined with other technologies to produce high added-value products. It is expected that further optimization of solvents, catalyst concentration and operating conditions could produce even higher yields than those demonstrated here.

**Table 4.1.** Hydroformylation reaction conditions and yields from olefinic oligomerization mixture

| Solvent | Reaction Temperature (˚C) | 1:1 Syngas (psig) | Total Conversion (%)[c] | Branched Aldehydes Yield (%) | n-Nonanal Yield (%) | N:I |
|---|---|---|---|---|---|---|
| Toluene[a] | 90 | 150 | 17.5 | 3.6 | 13.9 | 3.8 |

[a] Reaction carried out for 6 h.
[c] Only $C_9$ aldehydes detected.

## 4.4 Conclusions

Heterogeneously catalyzed oligomerization of light olefins over carbon-supported cobalt oxide followed by the hydroformylation of the straight-chain oligomerization product is a commercially-relevant process for the selective upgrading and functionalization of olefinic feeds to primary aldehydes. Even though the first oligomerization step of the reaction experienced deactivation, the system exhibited constant linear oligomer selectivity as a function of time. The effect of reaction temperature presented shows the opportunity to increase overall selectivity of this system even further through the optimization of reaction conditions.

## 4.5 Supporting Information

**Table S4.1.** Oligomerization and hydroformylation product analysis.

| Species | Oligomerization Product Mixture (rel. GC area) | Hydroformylation Product Mixture (rel. GC Area) |
|---|---|---|
| **$C_8$ Olefins** | | |
| 5-methyl-3-heptene (isomer 1) | 0.82 | |
| 5-methyl-3-heptene (isomer 2) | 1.68 | 0.879 |
| 5-methyl-2-heptene (isomer 1) | 1.9 | 1.25 |
| 5-methyl-2-heptene (isomer 2) | 1.45 | 0.53 |
| 2-ethyl-1-hexene | 4.48 | 2.296 |
| 1-octene | 0.28 | 0.3 |
| t-4-octene | 0.58 | 6.7 |
| 3-methyl-3-heptene (isomer 1) | 0 | 0 |
| 3-methyl-3-heptene (isomer 2) | if present, co-elutes | |
| t-3-octene, c-4-octene | 29.69 | 20.58 |
| c-3-octene | 22.24 | 3.81 |
| t-2-octene | 13.53 | 11.85 |
| 3-methyl-2-heptene | 1.16 | 0.86 |
| c-2-octene | 12.92 | 4.47 |
| **$C_9$ Aldehydes** | | |
| 2-propylhexanal | | 0.09 |
| 2-ethylheptanal/3-ethylheptanal | | 1.04 |
| 2-methyloctanal | | 0.36 |
| 4-methyloctanal | | 0.25 |
| 6-methyloctanal | | 0.63 |
| n-nonanal | | 9.03 |
| total aldehydes | | 11.40 |
| **Other Products** | | |
| n-octane | | 0.38 |

**Additional Experimental Details**

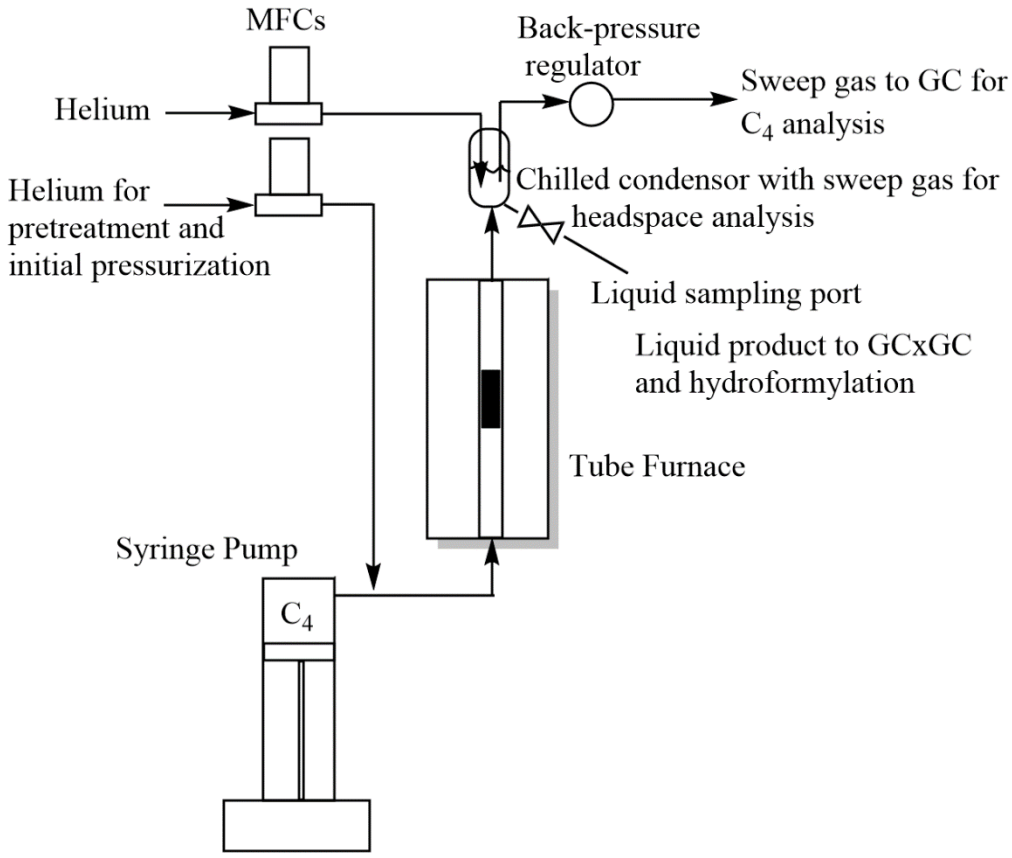


**Figure S4.1.** Diagram of oligomerization reactor and sampling scheme.

Rates of reaction were determined by quantification of oligomerization product GC areas.

For STEM images, a FEI Titan microscope was operated at 200 keV with a Cs probe aberration corrector (CEOS, GmbH). High-angle annular dark field (HAADF) images were obtained in the range of 54 to 270 mrad using a 0.8 nm probe and 24.5 mrad probe convergence semi-angle.

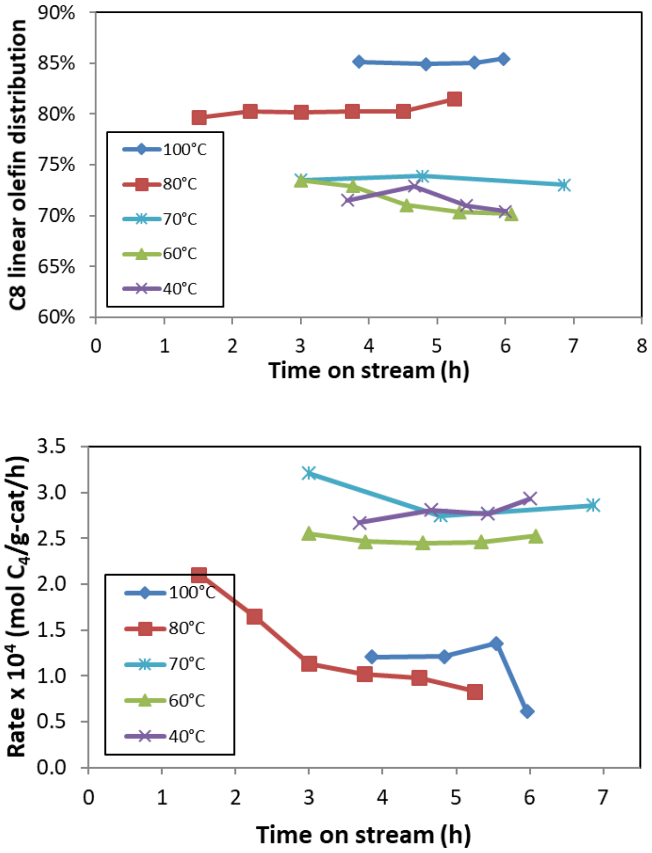


**Figure S4.2.** Time-on-stream performance of 2A-$CoO_x$/N-C as a function of temperature in terms of A) linear octene distribution of dimerization products and B) reaction rate. Reaction conditions: 450 psi; $WHSV^{1\text{-butene}}$=5 $h^{-1}$; 15 mL He sweep gas.

**Table S4.2.** GC operating conditions.

| | Gas-Phase Oligomerization Analysis | Liquid-Phase Oligomerization Analysis | Hydroformylation |
|---|---|---|---|
| Instrument | Shimadzu GC-2014 with Flame Ionization Detector | Agilent Technologies Model 7890B with Flame Ionization Detector and 5977A Mass Selective Detector | Agilent Technologies Model 6890 with Flame Ionization Detector |
| Data System | Shimadzu Lab Solutions | GC Image by Zoex Corporation | Agilent OpenLab A.02.01 |
| Injector Inlet | 200ºC using split/splitless liner with glass wool PN 221-75195 | 200ºC using 4mm split/splitless liner with glass wool PN 5190-2295 or the same liner packed with a ~4mm bed of 5% Pd/C. | 230ºC using 4mm split/splitless liner with glass wool PN 092002 |
| Column mode | Constant Pressure: 65.8 kPa, 11.25 mL/min column flow | Constant Flow: A flow modulator (CFP; Agilent, G3487A) was installed to make a GC×GC system. The first dimension column flow rate was 0.7 mL min−1 with H2 carrier gas. The second dimension column flow rate was 25 mL min−1 with H2 carrier gas. | Ramped Flow: 1 mL/min flow (hold for 151 min.), followed by 0.2 mL/min ramp to a flow of 2 mL/min (hold for 74 min.) |
| Mode | Split | Split | Split |
| Split Ratio | 10:1 | 20:1 | 175:1 |
| Injection Volume | 500µL gas injection | 1µL | 1µL |
| Column | Rt-QS-Bond 30 m X 20 micron X 0.52 mm | Two capillary columns, DB-17 20m X 0.3 micron X 0.18 mm and CP-Sil 5 CB 10 m X 0.12 micron X 0.25 mm CP Sil 5 CB, were coupled in series with the CFP. | Supelco Petrocol DH 100 m x 0.25 mm i.d. x 0.5 µm, followed by DB Wax 60 m x 0.32 mm x 0.1 µm; 2 columns in series |
| Oven Ramp. | 45ºC (hold 2 min.), ramp at 10ºC/min. to 250ºC (hold 8 min.) | 35ºC (hold 4 min.), ramp at 4ºC/min. to 250ºC (hold 5 min.) | 40ºC (hold 1 min.), ramp at 0.5ºC/min. to 85ºC (hold 0 min.), ramp at 0.25ºC/min. to 100ºC (hold 0 min.), ramp at 15ºC/min. to 190ºC (hold 0 min.), ramp at 20ºC/min to 235ºC (hold 70.75 min) |
| Run Time | 30 minutes | 64 minutes | 230 minutes |
| Detector | FID set at 250ºC | FID set at 250ºC | FID set at 300ºC |

## 4.6 References


1. C. T. O'Connor and M. Kojima, Catal. Today, 1990, 6, 329-349.
2. A. Finiels, F. Fajula and V. Hulea, Catalysis Science & Technology, 2014, 4, 2412.
3. R. D. Andrei, M. I. Popa, F. Fajula and V. Hulea, J. Catal., 2015, 323, 76-84.
4. A. Martínez, M. A. Arribas, P. Concepción and S. Moussa, Appl. Catal. A: Gen., 2013, 467, 509-518.
5. W. Keim, Angew. Chem. Int. Ed., 2013, 52, 12492-12496.
6. Y. V. Kissin, in Kirk-Othmer Encyclopedia of Chemical Technology, John Wiley & Sons, Inc., 2000, DOI: 10.1002/0471238961.1615122511091919.a01.pub3.
7. C. P. Nicholas, Appl. Catal. A: Gen., DOI: https://doi.org/10.1016/j.apcata.2017.06.011.
8. Y. T. Kim, J. P. Chada, Z. Xu, Y. J. Pagan-Torres, D. C. Rosenfeld, W. L. Winniford, E. Schmidt and G. W. Huber, J. Catal., 2015, 323, 33-44.
9. A. V. Lavrenov, T. R. Karpova, E. A. Buluchevskii and E. N. Bogdanets, Catalysis in Industry, 2016, 8, 316-327.
10. K. Toch, J. W. Thybaut and G. B. Marin, Appl. Catal. A: Gen., 2015, 489, 292-304.
11. J. Rabeah, J. Radnik, V. Briois, D. Maschmeyer, G. Stochniol, S. Peitz, H. Reeker, C. La Fontaine and A. Brückner, ACS Catalysis, 2016, 6, 8224-8228.
12. R. Y. Brogaard and U. Olsbye, ACS Catalysis, 2016, 6, 1205-1214.
13. A. N. Mlinar, G. B. Baur, G. G. Bong, A. B. Getsoian and A. T. Bell, J. Catal., 2012, 296, 156-164.
14. S. Moussa, P. Concepcion, M. A. Arribas, and A. Martinez, ACS Catal., 2018, 8, 3903-3912
15. A. N. Mlinar, B. K. Keitz, D. Gygi, E. D. Bloch, J. R. Long and A. T. Bell, ACS Catalysis, 2014, 4, 717-721.
16. E. D. Metzger, C. K. Brozek, R. J. Comito and M. Dincă, ACS Central Science, 2016, 2, 148-153.
17. R. G. Schultz, J. Catal., 1966, 6, 385-396.
18. R. G. Schultz, J. Catal., 1966, 6, 419-424.
19. Z. Xu, J. P. Chada, D. Zhao, C. A. Carrero, Y. T. Kim, D. C. Rosenfeld, J. L. Rogers, S. J. Rozeveld, I. Hermans and G. W. Huber, ACS Catalysis, 2016, 6, 3815-3825.
20. D. Zhao, Z. Xu, J. P. Chada, C. A. Carrero, D. C. Rosenfeld, J. L. Rogers, I. Hermans and G. W. Huber, ACS Catalysis, 2017, 7, 7479-7489.
21. Z. Xu, D. Zhao, J. P. Chada, D. C. Rosenfeld, J. L. Rogers, I. Hermans and G. W. Huber, J. Catal., 2017, 354, 213-222.
22. A. Behr, D. Obst, C. Schulte and T. Schosser, J. Mol. Catal. A: Chem., 2003, 206, 179-184.
23. C. Vogl, E. Paetzold, C. Fischer and U. Kragl, J. Mol. Catal. A: Chem., 2005, 232, 41-44.
24. E. Billing, A. G. Abatjoglou, and D. R. Bryant, US Pat., 4,668,651, 1987.
25. Olefin oligomerization experimentally tested with ethylene, propylene, 1-butene, and 1-hexene. It is expected that this catalyst could be extended to other alpha olefins or as a co-dimerization between unequal chain lengths.
26. R. Franke, D. Selent and A. Borner, Chem Rev, 2012, 112, 5675-5732.

27. H. S. Zijlstra and S. Harder, European Journal of Inorganic Chemistry, 2015, 2015, 19-43.
28. A. Y. Khodakov, W. Chu and P. Fongarland, Chemical Reviews, 2007, 107, 1692-1744.
29. I. T. Ghampson, C. Sepúlveda, R. Garcia, L. R. Radovic, J. L. G. Fierro, W. J. DeSisto and N. Escalona, Appl. Catal. A: Gen., 2012, 439-440, 111-124.

# Chapter 5. Olefin oligomerization on carbon-supported cobalt oxide catalysts: Effect of the support[6]

## 5.1 Introduction

The carbon-supported cobalt oxide catalyst ($CoO_x$/C) highlighted in Chapter 3 and 4 has been demonstrated to be one of the most selective heterogeneous materials to produce n-octenes. In this chapter, we further investigate the role of the carbon support during synthesis and reaction conditions. The influence of carbon on the formation of high concentrations of $Co^{2+}$, originally suggested in Chapter 3, is further investigated using temperature-programmed techniques. For comparison, we also evaluated combinations of common cobalt precursors on alternative catalyst carriers ($SiO_2$, $\gamma$-$Al_2O_3$, and $SiO_2$-$Al_2O_3$) to explain their lack of activity for linear olefin oligomerization.

Many common oxide carriers such as $SiO_2$, $Al_2O_3$, and $TiO_2$ are known to have metal-support interactions with cobalt at elevated temperatures [1]. Carbon materials can act as ideal catalyst supports for many reactions since they have large surface areas and are usually chemically inert. Nevertheless, the insufficient mechanical strength (i.e. high attrition) and the inability to regenerate them in oxidizing atmospheres are some of the disadvantages that should be considered

---

[6] This chapter was adapted from: Joseph P. Chada, Alvin Jonathan, Zachary M. Konz, Bradley D. Maccoux, Zhuoran Xu, Dongting Zhao, Ive Hermans, James A. Dumesic, George W. Huber, Olefin oligomerization on carbon-supported cobalt oxide catalysts: Effect of the support., *manuscript in preparation.*

Author contributions: J.P.C. and J.A.D., G.W.H designed research; J.P.C and A.J. performed oligomerization reactions and catalyst characterization; B.D.M. and Z.M.K aided in catalyst characterization; J.P.C. and G.W.H. wrote the paper; and Z.X, D.Z., and I.H. aided in cobalt oxide catalyst discovery.

when choosing a carbon-based material [2]. Although inert to many reaction, activated carbon is a diverse material which can contain numerous surface functionalities, complex pore structures, and varying amounts heteroatoms such as H, O, and N [3]. There are numerous reports in the literature on the effect of the support on catalytic activity [1, 2, 4]. Even within the realm of carbon materials, distinct types of carbon can have a large effect on the dispersion and activity of transition metals. Karanjkar et al [4], showed that Rh and Re supported on either carbon black or activated carbon for the hydrogenolysis of tetrahydopyran-2-methanol can cause as much as a two order-of-magnitude difference in activity due to the interactions of both metals and the carbon support.

In Chapter 3, we presented XAS, XRD, and Raman characterization of carbon-supported cobalt catalysts as a function of pretreatment temperature. All the characterization methods consistently showed evidence of a dynamic autoreduction of cobalt oxide with increasing temperature. Chen et al. [5] first reported a similar autoreduction behavior for $Fe_2O_3$ supported on carbon nanotubes (CNTs). In their study, they synthesized $Fe_2O_3$ particles both on the inside and outer wall of CNTs. With high-resolution transmission electron microscopy, they observed a phase change from $Fe_2O_3$ to Fe at 600°C in a helium atmosphere. Interestingly, the encapsulated $Fe_2O_3$ particles were reduced at temperatures as much as 200°C lower than particles supported on the outside of the CNTs. They attributed the reductive behavior to the interaction with the carbon wall of the CNT rather than reactions with surface functional groups. In 2010, Xiong et al. [6] observed the same autoreductive behavior for the first time with cobalt oxide supported on nitrogen-doped carbon spheres. Similar to our observations, they demonstrated a complete reduction of Co in an inert atmosphere by 480°C. When tested for Fisher-Tropsch synthesis (FTS), the autoreduced samples had a higher performance than the same samples reduced in a

$H_2$-atmosphere. They rationalized that the reductive behavior was due to the interaction of oxygen from cobalt oxide with the edges of graphite flakes which are ideal sites for adsorbing oxygen [6]. Ultimately, the reaction with carbon rather than $H_2$ led to higher Co dispersion and explained the increase catalytic performance.

Similar to our studies on $CoO_x$/C, several groups have shown that Ni-based aluminosilicates are active for oligomerization without the use of an activator [7-12]. It is typical for homogeneous catalysts and MOF-supported Ni catalysts to use an alkylaluminum activator such as methylaluminoxane (MAO) to form the initial metal-carbon bond which initiates the catalytic cycle [13, 14]. With DFT studies, Brogaard and Olsbye [7] suggested that the charge of the support is important balancing in the formation of an agostically bound $[Ni(II)\text{-ethylene-H}]^+$ for Ni supported on SSZ-24. They also found that ethylene dimerization over Ni/SSZ-24 would most likely proceed via a Cossee-Arlman mechanism which is the accepted mechanism over many homogeneous catalysts. We have previously proposed that oligomerization over $CoO_x$/C also likely follows a Cossee-Arlman mechanism (Figure 5.1) [15]. It is not yet known what function the support material has on the formation of Co active sites for olefin coordination.

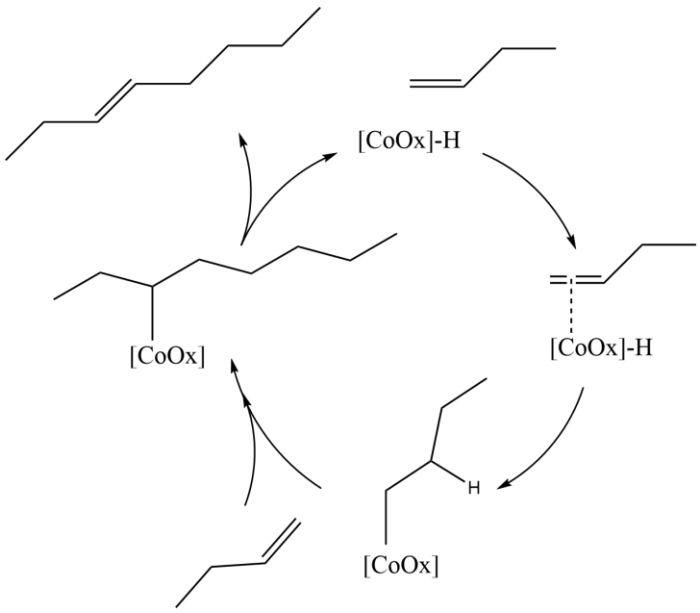


**Figure 5.1.** Proposed Cossee-Arlman mechanism for 1-butene oligomerization.

## 5.2 Experimental

### 5.2.1 Catalyst synthesis

Activated carbon (Norit Darco MRX, Cabot), $SiO_2$ (Davicat 1404, Grace), $\gamma$-$Al_2O_3$ (Strem), $SiO_2$-$Al_2O_3$ (Support-grade 135, Sigma-Aldrich), and functionalized multi-walled carbon nanotubes (CTI) were used as support materials for catalyst synthesis. Multi-walled carbon nanotubes were functionalized with either OH, $NH_2$, or COOH surface groups and used without further modification. Catalysts were prepared by incipient wetness impregnation (IWI) of either $Co(NO_3)_2 \cdot 6H_2O$, $Co(CH_3CO_2)_2 \cdot 4H_2O$, or $[Co(NH_3)_6]Cl_3$ in deionized water (DI). Only catalysts synthesized with cobalt nitrate were found to be active. All catalytic materials in the text refer were synthesized with cobalt nitrate precursors unless otherwise noted. Theoretical cobalt weight loading for all materials were 12%. Synthesized materials in this chapter were dried at room temperature. Drying at elevated temperatures was avoided as temperatures as low as 100°C is

known to affect cobalt agglomeration on some supports [16]. 2A-$CoO_x$/N-C was synthesized by treating the carbon support with ammonium hydroxide before and after cobalt impregnation.

Graphite-coated $Al_2O_3$ was synthesized based on the method of Xiong et al. [17]. 2 g of γ-$Al_2O_3$ (Strem) was packed in a ½" quartz tube and supported by quartz wool plugs. The atmosphere was purged with helium and the temperature was ramped to 900°C at 20°C/min. Once at temperature, the gas flow was switched to 10% $CH_4$ in $N_2$ and held isothermally for 30 min to coat the surface with a few layers of graphite. The graphite coated support was denoted GC-$Al_2O_3$. Cobalt impregnation was performed similar to other supports except that the DI water was replaced with 50:50 DI water:ethanol (99.9%) mixture due to the hydrophobic nature of the graphite coating.

**5.2.2 Catalyst characterization**

Temperature-programmed desorption (TPD) was performed with a Micromeritics Autochem II 2920. The evolution of gaseous products was simultaneously monitored via a connected mass spectrometer (MS, MKS Cirrus 2). 50-100 mg of sample was supported by quartz wool in the U-tube reactor without any pretreatment or calcination step and heated at 5 °C/min in 50 mL/min He flow. Mass-to-charge assignments were based on the most probable decomposition products of the known species added during synthesis. The major products observed include $H_2$ (m/z=2), $H_2O$ (m/z=18), CO (m/z=28), NO (m/z=30), $O_2$ (m/z=32), $CO_2$ (m/z=44), $NO_2$ (m/z=46), and $SO_2$ (m/z=64).

Surface area and pore size analysis were performed with a Micromeritics 2020. Prior to analysis samples were degassed at 120°C for 6 h. $N_2$ isotherms were collected at 77 K. BET plots

were analyzed between 0.05 and 0.3 $P/P_0$. Pore size distributions were calculated from the desorption branch based on the BJH method.

Powder x-ray diffraction measurements (XRD) were collected on a Rigaku D/Max Rapid II diffractometer with a two-dimensional imaging plate and Mo $K_\alpha$ x-ray source. A molybdenum source was chosen to minimize x-ray fluorescence from cobalt.

### 5.2.3 Catalytic measurements

Reactivity measurements were carried out in a ¼" fixed-bed up-flow reactor. Details of the experimental setup can be found in Section 4.2. 0.5 g of catalyst was loaded as synthesized without any drying or calcination step. Prior to reaction, the catalyst was pretreated in Ar (UHP, 100 mL/min) at 230°C (1°C/min ramp, 2 h hold). The reactor was then cooled to reaction temperature, pressurized to 450 psig with Ar, then 1-butene (99.9%) was flowed via a high-pressure syringe pump (Teledyne Isco). $C_4$ isomerization products were analyzed by sampling a Ar sweep gas flowing through the headspace of a chilled collection vessel after the reactor with a GC (Shimadzu). Liquid-phase reaction products were collected and drained from the same collection vessel into a chilled n-hexane solution and analyzed by a GCxGC-MS system (Agilent). The skeletal composition of the $C_8$ isomers products was determined by GCxGC-MS analysis of the hydrogenated liquid products. Reaction mixtures were hydrogenated with the $H_2$ carrier gas of the GC when passed over a Pd/C catalyst packed in the GC liner held at 200°C. Details on the GC parameters for the analysis of isomerization and oligomerization products can be found in Table S4.2. Overall 1-butene conversion was calculated based on Equation 5.1. The linear selectivity was based on the hydrogenated $C_8$ reaction products according to Equation 5.2. The selectivity to oligomer products was calculated based on Equation 5.3.

$$\boldsymbol{Conversion}\ (\%) = \frac{mol_{1-butene,inlet} - mol_{1-butene,outlet}}{mol_{1-butene,inlet}} \quad [5.1]$$

$$\boldsymbol{C_8\ Linear\ Selectivity} = \frac{mol_{linear\ C_8}}{mol_{total\ C_8}} \quad [5.2]$$

$$\boldsymbol{Oligomerization\ Selectivity} = \frac{mol_{total\ oligomers}}{mol_{total\ oligomers} + mol_{C_4\ isomers}} \quad [5.3]$$

### 5.2.4 Isotopic transient experiments

A reactor system was constructed to perform multi-product steady-state isotopic kinetic analysis (SSITKA) based on the design of Goodwin and co-workers [18] and Davis and co-workers [19, 20]. Comprehensive reviews by Shannon and Goodwin [18] and Ledesma et al. [21] summarize of the mathematical derivations, experimental techniques, and limitations. A diagram of the reactor system can be found in Figure S5.1. Multi-product SSITKA of ethylene oligomerization was used to measure the intrinsic activity and dispersion of $CoO_x$/C active sites. We have previously shown that $CoO_x$/C produces similar linear distributions for ethylene and 1-butene oligomerization [15]. For SSITKA experiments, 250 mg of catalyst was used such that the conversion was sufficiently low <10% and liquid products were not formed. Ethylene was diluted in either He or a mixture of 5% Ar in He. Gas-phase $C_4$ and $C_6$ products were analyzed by the same GC (Shimadzu) mentions previously.

After reaching pseudo-steady state (5 h TOS), an isotopic switch was made between $^{12}C_2H_4$ (Airgas) and $^{13}C_2H_4$ (Isotec) with a rapid 4-port switching valve (Valco). Multi-product SSITKA experiments were ran at low pressure (16 psig) to minimize the amount of labelled gas used. Care was taken to match the pressure of each $C_2H_4$ steam so that reaction conditions were not disturbed during the isotopic switch. The $C_2H_4$ flowrate was varied from 5-9 mL/min (30-54 mL/min total flow) to investigate effects of product re-adsorption. The multi-product SSITKA system consisted

of a 34-port sampling valve equipped with 500 µl sample loops which were used to collect samples during isotopic transients. The collected samples were later separated by a Restek Alumina-Bond capillary column (0.53 mm ID, 50 m length) placed in the same GC oven. The separated products were diluted in $H_2$ and methanized over 2 g of 5% $Pt/Al_2O_3$ (Strem) maintained at 400°C. The concentration of $^{12}C$ in each separated reaction product was determined by the amounts of $^{12}CH_4$ (m/z = 15) and $^{13}CH_4$ (m/z = 17). The contribution from $^{13}CH_4$ to the $^{12}CH_4$ fragmentation pattern was corrected by calibrating the signal from $^{13}C_2H_4$.

The average surface residence time of reaction intermediates ($\tau_i$) was measured by integrating the area between the normalized transient response of $^{12}C$ for each separated product ($F_i$) and the inert tracer Ar ($F_{Ar}$) according to Equation 5.4.

$$\tau_i = \int_0^\infty (F_i - F_{Ar})\, dt \qquad [5.4]$$

The number of surface intermediates ($N_i$) leading to each specific product was determined from the material balance over the reactor as shown in Equation 5.5.

$$N_i = \tau_i R_i \qquad [5.5]$$

where $R_i$ is the rate of formation of product $i$ at steady-state.

## 5.3 Results and Discussion

### 5.3.1 Reactivity

1-Butene is an effective probe molecule to study oligomerization catalysts as it is the simplest olefin that can be used to study both oligomerization and isomerization (undesired) of the feed molecule simultaneously. It is challenging to extract isomerization rate information for smaller feedstocks as oligomerization products are often in thermodynamic equilibrium. A unique feature of $CoO_x/C$ is its selectivity towards linear oligomers in the $C_8$-product range. A comparison

between the product selectivity of $CoO_x$ supported on different support materials for 1-butene oligomerization is presented in Figure 5.2. Figure 5.2a compares the selectivity toward oligomerization as a function of conversion. $CoO_x/SiO_2$, $CoO_x/\gamma\text{-}Al_2O_3$, were not included as they did not have any measurable activity (<0.1% 1-butene conversion). $CoO_x/C$, $2A\text{-}CoO_x/C$ and $CoO_x/SiO_2\text{-}Al_2O_3$ showed high conversions of the 1-butene feed but $CoO_x/SiO_2\text{-}Al_2O_3$ had a significantly lower oligomer selectivity (i.e. high rates of isomerization). Data in Figure 5.2 was collected at equivalent intervals from 2-10 h TOS. The rapid deactivation of this catalyst can be visualized from the widely-spaced data points. The smaller grouping of data points for both carbon supports shows their relative stability compared to $CoO_x/SiO_2\text{-}Al_2O_3$. The results are analogous to reports on the bifunctional nature of Ni-based aluminosilicates [10, 11]. Martínez et al. [11] demonstrated that $H^+$ ion exchange positions were necessary to exchange with $Ni^{2+}$ cations in Ni-Beta for ethylene oligomerization. After all sites were exchanged (2.5 wt% Ni), additional Ni formed inactive NiO clusters.

Figure 5.2b compares the selectivity toward linear dimers as a function of conversion. Linearity calculations are limited to the $C_8$ product region since the number of potential isomers increases exponentially as chain length increases and complicates GC analysis. Since linear olefins are highly-valued polymer, detergent, and surfactant precursors, any catalysts with activity toward the upper right corner of the graph are desirable as they retain linear selectivity at high conversion. By comparing carbon-based $CoO_x/C$ and $2A\text{-}CoO_x/C$ with $CoO_x/SiO_2\text{-}Al_2O_3$, the enhanced selectivity for carbon materials is apparent. Ammonium hydroxide treatment before and after cobalt impregnation ($2A\text{-}CoO_x/C$) increases activity slightly with a slight decrease in linear $C_8$ products.

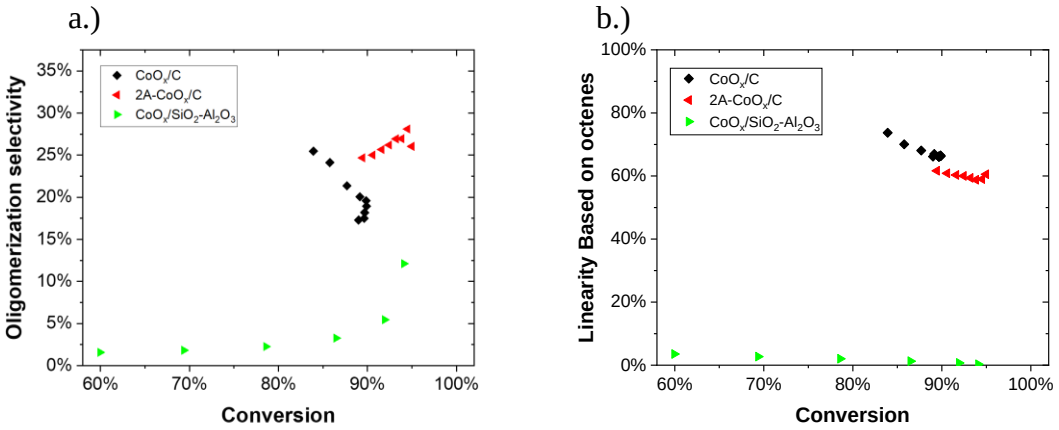


**Figure 5.2.** a) Oligomerization and b) linear octene selectivity as a function of conversion for different supports. Data included from 2-10 h TOS. Reaction Conditions: 80°C, 450 psi, 0.5 g catalyst, 0.05 mL/min 1-butene.

To evaluate the differences between the support materials and the prepared catalyst we can compared the material properties as determined by $N_2$ adsorption (Table 5.1) and XRD (Figure 5.3). From $N_2$ isotherms, all four support materials had relatively high surface area and similar average pore sizes. X-ray diffractograms all showed diffraction peaks consistent with the formation of $Co_3O_4$. Peak broadening is most apparent for the $CoO_x$/C-230 and suggests smaller average cobalt crystallite size.

**Table 5.1.** Physical properties estimated from $N_2$ isotherms.

| Catalyst Support | BET surface area ($m^2/g$) | BJH pore width, desorption (nm) |
|---|---|---|
| Carbon | 604.3 | 6.4 |
| $SiO_2$ | 509.8 | 5.5 |
| γ-$Al_2O_3$ | 204.8 | 5.8 |
| $SiO_2$-$Al_2O_3$ | 451.4 | 4.6 |

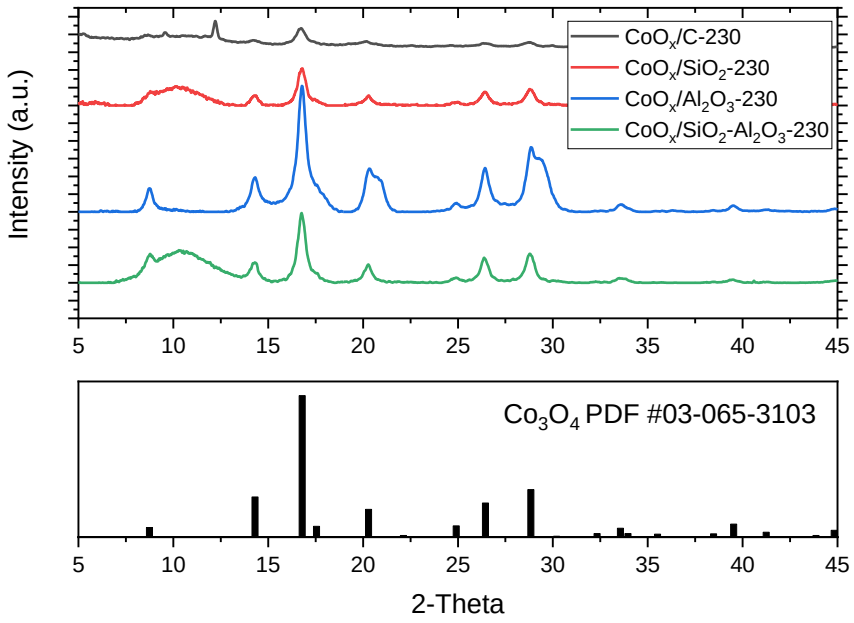


**Figure 5.3.** Top: XRD diffractograms for CoOx on various support materials. All four samples were pretreated at 230°C for 2 h. Bottom: Reference powder diffraction file for $Co_3O_4$.

### 5.3.2 Formation of active oligomerization sites

TPD-MS was used to track the decomposition products from the activated carbon support, unsupported $Co(NO_3)_2 \cdot 6H_2O$, and supports impregnated with cobalt nitrate (Figure 5.3). The MS spectra for the unmodified carbon support has significant contributions from $H_2O$, CO, and $H_2$. TPD is a popular method for tracking surface functional group compositions as the most common functionalities thermally desorb as either CO or $CO_2$. From Figure 5.3a, the broad CO peak at 890°C suggests that the activated carbon support contains a large amount of carbonyl surface groups (CO from carbonyl groups deposes from 700-980°C) [22]. It is possible that the surface functionality could play a role in the pretreatment. The unsupported $Co(NO_3)_2 \cdot 6H_2O$ (Figure 5.4b) has several dehydration steps which lead to an anhydrous cobalt nitrate (Equation 5.6). Beginning around 150°C, cobalt nitrate begins to decompose to form NO, $NO_2$, and $O_2$ (Equation 5.7) until

around 350°C leaving $Co_3O_4$, the most stable oxide of cobalt at low-to-moderate temperatures. Around 800°C, $O_2$ is released as $Co_3O_4$ converts to CoO, the most stable cobalt oxide at high temperatures.

$$Co(NO_3)_2 \times 6H_2O \rightarrow Co(NO_3)_2 + 6H_2O \quad [5.6]$$

$$Co(NO_3)_2(s) \rightarrow Co_3O_4(s) + xNO(g) + yNO_2(g) + zO_2(g) \quad [5.7]$$

The influence of the support material is on decomposition profile is rather significant. From Figure 5.4c-f, all four supports have different temperatures when the nitrate precursor is completely removed. One of the most noticeable features is the sharp peak from CO and $CO_2$ in Figure 5.4c at 600°C. The sudden desorption corresponds to the complete reduction of $CoO_x$ to Co by the carbon support. A close observation reveals that there is nearly-continuous $CO_2$ profile from 150-750°C. These results suggest that immediately after the formation of $Co_3O_4$ (confirmed by XRD), carbon continually reduced $CoO_x$ to primarily $Co^{2+}$ followed by a severe reduction at 600°C. The most intense desorption products at 230°C, the temperature at which catalysts are pretreated prior to catalytic experiments, are NO, $H_2O$, and $CO_2$. $CoO_x$/C is the only sample that has a significant $CO_2$ peak in the 150-400°C range.

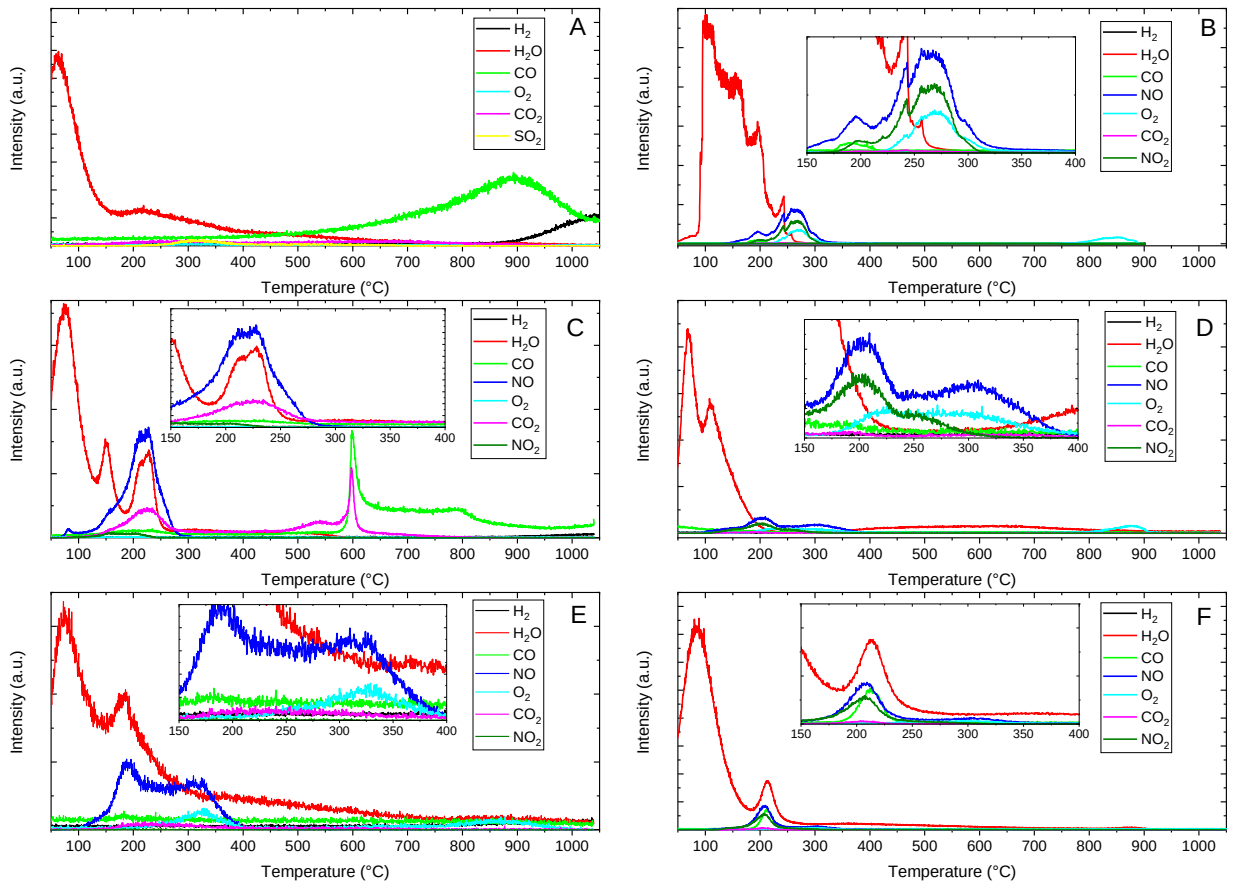


**Figure 5.4.** TPD-MS analysis of (a) unsupported $Co(NO_3)_2 \cdot 6H_2O$, (b) Norit Darco MRX carbon, (c) $CoO_x/C$, (d) $CoO_x/SiO_2$, (e) $CoO_x/Al_2O_3$, and (f) $CoO_x/SiO_2$-$Al_2O_3$. TPD Conditions: 5°C/min, 50 mL/min He flow.

### 5.3.3 Comparison of carbon-based materials

To further investigate the role of the carbon support on the formation of the active $CoO_x$ species, we tested several well-defined carbon structures to see if they were also active for oligomerization. Recent works by Xiong et al. [17] and Pham et al. [23] have investigated methods of depositing carbon layers on oxide surfaces by either chemical vapor deposition or the pyrolysis of sugar solutions impregnated within the pores. In both papers, the carbon coating protected the oxide support from the harsh acidic environment during biomass conversion. Based on their work,

we were able to synthesize a graphite-coated γ-$Al_2O_3$ ($CoO_x$/GC-Al2O3) it an attempt add carbon sites that would be able to reduce $CoO_x$ and activate the cobalt nitrate that was added subsequently. Additionally, to investigate the role of surface functional groups and their ability to react with cobalt nitrate, we used CNTs synthesized with primarily OH, $NH_2$, or COOH functional groups. The oligomerization and linear octene selectivity of these catalysts is presented in Figure 5.5. Compared to the results for the different oxide supports, all carbon-based materials were active for oligomerization. $CoO_x$/GC-$Al_2O_3$ has the highest linear selectivity and higher linear octene selectivity than $CoO_x$/C although at lower conversion. $CoO_x$/CNT-OH, $CoO_x$/CNT-$NH_2$, and $CoO_x$/CNT-COOH all had similar oligomerization and linear octene selectivity but no definitive trends for activity could be found.

Cheng et al. [2] demonstrated the autoreductive behavior of cobalt supported on $SiO_2$ pre-coated with a layer of carbon for FTS. They found that several layers of carbon coating had a sufficient interaction with carbon nanoparticles to form highly-reduced cobalt nanoparticles on carbon support in the absence of hydrogen. XRD characterization of the carbon-based materials suggested that all the supports formed primarily $Co_3O_4$ (Figure 5.6).

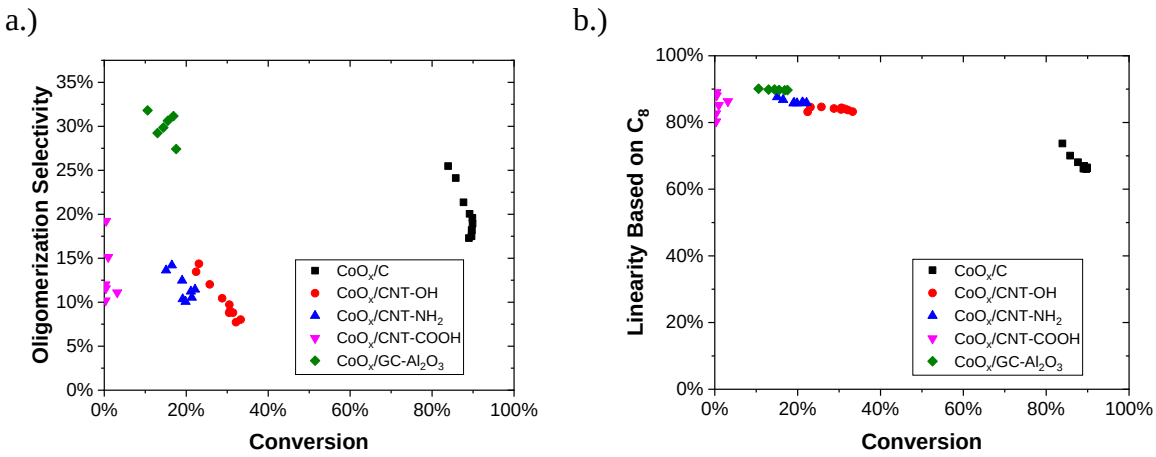


**Figure 5.5.** Oligomerization and linear octene selectivity as a function of conversion for carbon-based supports. Data included from 2-10 h TOS. Reaction Conditions: 80°C, 450 psi, 0.5 g catalyst, 0.05 mL/min 1-butene.

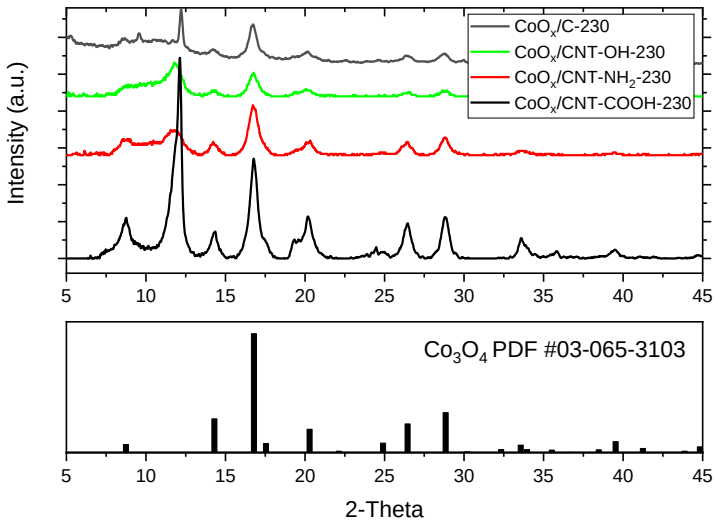


**Figure 5.6.** Top: XRD diffractograms for CoOx on various carbon-based materials. All four samples were pretreated at 230°C for 2 h. Bottom: Reference powder diffraction file for $Co_3O_4$.

### 5.3.4 Steady-state isotopic transient kinetic analysis

Due to the complicated surface structure of cobalt oxides, there is not a well-known method to quantify surface sites for cobalt oxide catalysts. Methanol chemisorption has been proposed as a potential method to quantify well-defined cobalt oxide surfaces [24, 25] but reactions with

activated carbon convolute the data. Additionally, there is not a procedure to selectively probe $Co^{2+}$ vs $Co^{3+}$ sites. SSITKA has been used previous count catalytic sites for FTS[26], CO hydrogenation[19], and Guerbet coupling [20]. In order to extract reliable estimates of both dispersion and kinetic parameters for $CoO_x$/C, we used SSITKA of $^{13}C$-labeled ethylene to count active oligomerization sites. SSITKA is a transient method that allows for the number of surface intermediates that lead to a specific reaction product to be quantified by observing the time it takes to completely replace the adsorbed surface species with labelled isotopologues after a step change. The technique is valid for any reaction mechanism as the reacting molecule is the probe. The only necessary condition is that steady-state conditions must be achieved. $CoO_x$/C deactivated rapidly during the first few hours of time-on-steam then slowed its deactivation to a pseudo steady-state condition that was stable enough to complete the analysis. By stopping several repeat reactions at different times-on-stream and analyzing the spent catalyst with $N_2$ adsorption we observed a continuous decrease in surface area, or pore filling, as the primary form of deactivation (Figure S5.2 and Table S5.1).

The normalized transient response for $CoO_x$/C is shown in Figure 5.7. The inert tracer and $^{12}C_2H_4$ drop off rapidly while the $^{12}C_4H_8$ and $^{12}C_6H_{12}$ have much longer transient times consistent with a stronger binding strength for longer alkyl intermediates. Average surface residence time for $^{12}C_2H_4$ and $^{12}C_4H_8$ were 2.7 and 29 s, respectively, which corresponds to a cobalt dispersion of 3.2%. The surface of $CoO_x$/C was found to be covered with primarily ethylene which rapidly desorb upon the isotopic switch. By counting the active surface sites, we calculated a TOF of 0.4 $s^{-1}$. We will be able to use this technique in future studies to quantitatively evaluate the reactivity of $CoO_x$ which are challenging to characterize with other methods.

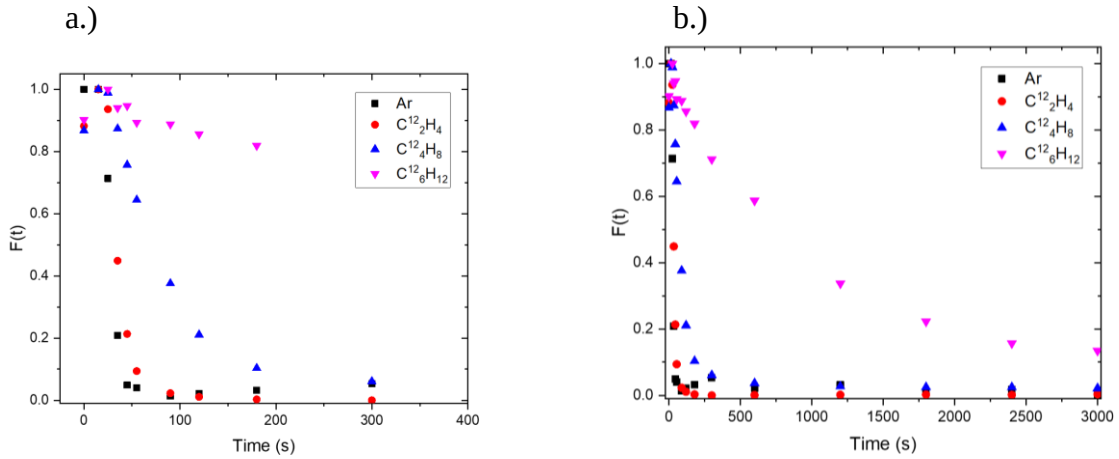


**Figure 5.7.** Normalized transient response for multi-product SSITKA of $C_2H_4$ oligomerization. a) Zoomed-in b) entire data range. Reaction conditions: 5 mL/min $C_2H_4$, 25 mL/min inert, 0.25 g catalyst, system pressure 16 psig.

## 5.4 Conclusions

In this chapter, we explored the effect of the support material on the activation and formation of heterogeneous, cobalt oxide oligomerization sites. Several common catalyst supports and cobalt precursors were tested for their activity and selectivity for 1-butene oligomerization. It was found that both carbon- and $SiO_2$-$Al_2O_3$-supported catalysts were active although only carbon-based supports could activate $CoO_x$ for linear oligomerization. Subsequently, several types of carbon-based materials, including functionalized MWCNTs and graphite-coated γ-$Al_2O_3$, were tested and demonstrated to have various degrees of activity. The different decomposition reactions for cobalt nitrate on various support materials was demonstrated with TPD-MS. X-ray diffraction patterns suggested that all catalysts tested are primarily comprised of $Co_3O_4$. It is hypothesized that $Co^{2+}$ is the active site for oligomerization and is formed from the partial reduction of $CoO_x$ due to the interaction of the cobalt nitrate precursor with carbon. The functionalization of the surface to a Co(II)-hydride species could not be excluded. Deactivation as a function of time-on-

stream was shown to occur rapidly due to pore filling. With SSITKA, we calculated that after 5h TOS <0.2% of cobalt was active for oligomerization with an average TOF of 0.4 $s^{-1}$.

## 5.5 Supplementary Information

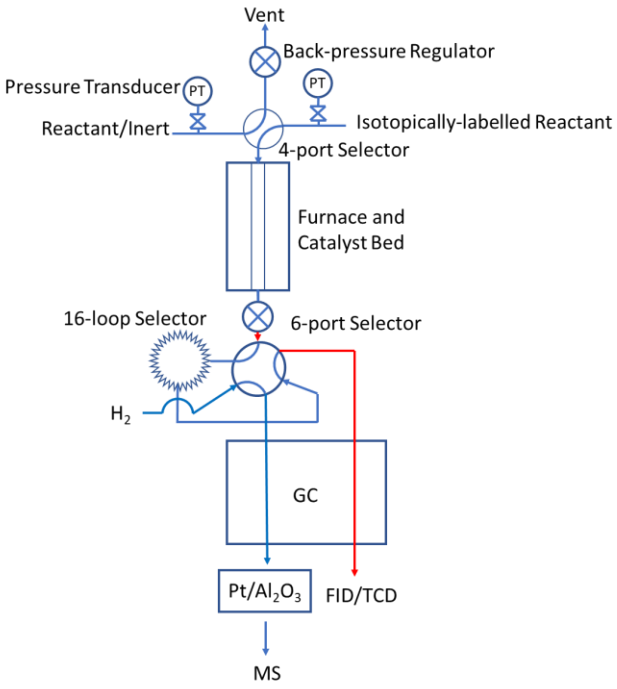


**Figure S5.1.** Reactor system for multi-product SSITKA.

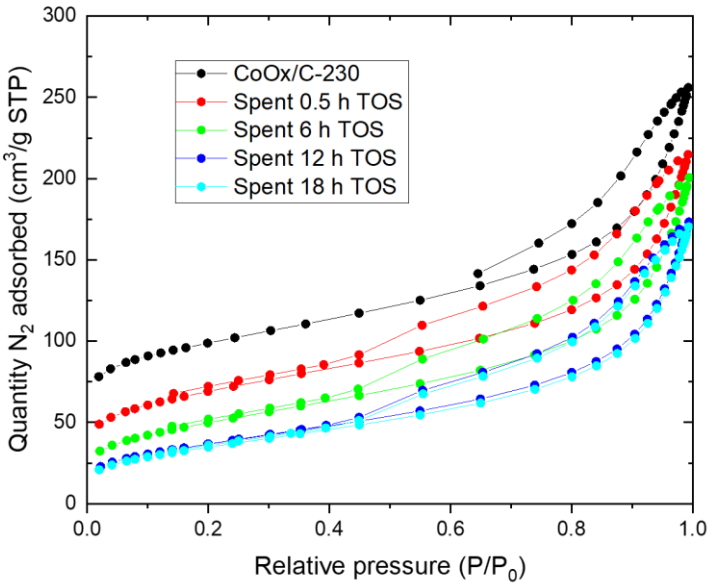


**Figure S5.2.** $N_2$ isotherms of CoOx/C after pretreatment at 230°C and after various times-on-stream for ethylene oligomerization.

**Table S5.1.** BET surface area and BJH pore size of CoOx/C after pretreatment at 230°C and after various times-on-stream for ethylene oligomerization.

| Co/C time on stream (h) | BET surface area ($m^2$/g) | BJH pore width, desorption (nm) |
|---|---|---|
| 0.0 | 333.5 | 6.0 |
| 0.5 | 241.5 | 6.3 |
| 6.0 | 179.4 | 6.6 |
| 12.0 | 134.1 | 6.8 |
| 18.0 | 127.9 | 7.0 |

## 5.6 References


1. G. Jacobs, T.K. Das, Y. Zhang, J. Li, G. Racoillet, B.H. Davis, Fischer–Tropsch synthesis: support, loading, and promoter effects on the reducibility of cobalt catalysts, Appl. Catal. A: Gen., 233 (2002) 263-281.
2. K. Cheng, V. Subramanian, A. Carvalho, V.V. Ordomsky, Y. Wang, A.Y. Khodakov, The role of carbon pre-coating for the synthesis of highly efficient cobalt catalysts for Fischer–Tropsch synthesis, J. Catal., 337 (2016) 260-271.
3. F. Rodríguez-reinoso, The role of carbon materials in heterogeneous catalysis, Carbon, 36 (1998) 159-175.
4. P.U. Karanjkar, S.P. Burt, X. Chen, K.J. Barnett, M.R. Ball, M.D. Kumbhalkar, X. Wang, J.B. Miller, I. Hermans, J.A. Dumesic, G.W. Huber, Effect of carbon supports on RhRe bifunctional catalysts for selective hydrogenolysis of tetrahydropyran-2-methanol, Catalysis Science & Technology, 6 (2016) 7841-7851.
5. W. Chen, X. Pan, M.-G. Willinger, D.S. Su, X. Bao, Facile Autoreduction of Iron Oxide/Carbon Nanotube Encapsulates, Journal of the American Chemical Society, 128 (2006) 3136-3137.
6. X. Haifeng, M. Mahluli, R.M. K., J.L. L., B.D. G., C.N. J., Autoreduction and Catalytic Performance of a Cobalt Fischer–Tropsch Synthesis Catalyst Supported on Nitrogen-Doped Carbon Spheres, ChemCatChem, 2 (2010) 514-518.
7. R.Y. Brogaard, U. Olsbye, Ethene Oligomerization in Ni-Containing Zeolites: Theoretical Discrimination of Reaction Mechanisms, ACS Catalysis, 6 (2016) 1205-1214.
8. R. Henry, M. Komurcu, Y. Ganjkhanlou, R.Y. Brogaard, L. Lu, K.-J. Jens, G. Berlier, U. Olsbye, Ethene oligomerization on nickel microporous and mesoporous-supported catalysts: Investigation of the active sites, Catal. Today, 299 (2018) 154-163.
9. I. Agirrezabal-Telleria, E. Iglesia, Stabilization of active, selective, and regenerable Ni-based dimerization catalysts by condensation of ethene withinordered mesopores, J. Catal., 352 (2017) 505-514.
10. V. Hulea, F. Fajula, Ni-exchanged AlMCM-41?An efficient bifunctional catalyst for ethylene oligomerization, J. Catal., 225 (2004) 213-222.
11. A. Martínez, M.A. Arribas, P. Concepción, S. Moussa, New bifunctional Ni–H-Beta catalysts for the heterogeneous oligomerization of ethylene, Appl. Catal. A: Gen., 467 (2013) 509-518.
12. S. Moussa, P. Concepción, M.A. Arribas, A. Martínez, Nature of Active Nickel Sites and Initiation Mechanism for Ethylene Oligomerization on Heterogeneous Ni-beta Catalysts, ACS Catalysis, 8 (2018) 3903-3912.
13. W. Kaminsky, Discovery of Methylaluminoxane as Cocatalyst for Olefin Polymerization, Macromolecules, 45 (2012) 3289-3297.
14. E.D. Metzger, R.J. Comito, C.H. Hendon, M. Dincă, Mechanism of Single-Site Molecule-Like Catalytic Ethylene Dimerization in Ni-MFU-4l, Journal of the American Chemical Society, 139 (2017) 757-762.

15. Z. Xu, D. Zhao, J.P. Chada, D.C. Rosenfeld, J.L. Rogers, I. Hermans, G.W. Huber, Olefin conversion on nitrogen-doped carbon-supported cobalt catalyst: Effect of feedstock, J. Catal., 354 (2017) 213-222.
16. P. Munnik, P.E. de Jongh, K.P. de Jong, Control and Impact of the Nanoscale Distribution of Supported Cobalt Particles Used in Fischer–Tropsch Catalysis, Journal of the American Chemical Society, 136 (2014) 7333-7340.
17. H. Xiong, J. Schwartz Thomas, I. Andersen Nalin, A. Dumesic James, K. Datye Abhaya, Graphitic‐Carbon Layers on Oxides: Toward Stable Heterogeneous Catalysts for Biomass Conversion Reactions, Angew. Chem. Int. Ed., 54 (2015) 7939-7943.
18. S.L. Shannon, J.G. Goodwin, Characterization of Catalytic Surfaces by Isotopic-Transient Kinetics during Steady-State Reaction, Chemical Reviews, 95 (1995) 677-695.
19. S. Hanspal, Z.D. Young, H. Shou, R.J. Davis, Multiproduct Steady-State Isotopic Transient Kinetic Analysis of the Ethanol Coupling Reaction over Hydroxyapatite and Magnesia, ACS Catalysis, 5 (2015) 1737-1746.
20. H. Shou, R.J. Davis, Multi-product steady-state isotopic transient kinetic analysis of CO hydrogenation over supported molybdenum carbide, J. Catal., 306 (2013) 91-99.
21. C. Ledesma, J. Yang, D. Chen, A. Holmen, Recent Approaches in Mechanistic and Kinetic Studies of Catalytic Reactions Using SSITKA Technique, ACS Catalysis, 4 (2014) 4527-4547.
22. J.L. Figueiredo, M.F.R. Pereira, M.M.A. Freitas, J.J.M. Órfão, Modification of the surface chemistry of activated carbons, Carbon, 37 (1999) 1379-1389.
23. H.N. Pham, A.E. Anderson, R.L. Johnson, T.J. Schwartz, B.J. O'Neill, P. Duan, K. Schmidt-Rohr, J.A. Dumesic, A.K. Datye, Carbon Overcoating of Supported Metal Catalysts for Improved Hydrothermal Stability, ACS Catalysis, 5 (2015) 4546-4555.
24. L.J. Burcham, L.E. Briand, I.E. Wachs, Quantification of Active Sites for the Determination of Methanol Oxidation Turn-over Frequencies Using Methanol Chemisorption and in Situ Infrared Techniques. 1. Supported Metal Oxide Catalysts, Langmuir, 17 (2001) 6164-6174.
25. M.M. Natile, A. Glisenti, Study of Surface Reactivity of Cobalt Oxides: Interaction with Methanol, Chemistry of Materials, 14 (2002) 3090-3099.
26. J. Yang, E.Z. Tveten, D. Chen, A. Holmen, Understanding the Effect of Cobalt Particle Size on Fischer−Tropsch Synthesis: Surface Species and Mechanistic Studies by SSITKA and Kinetic Isotope Effect, Langmuir, 26 (2010) 16558-16567.

# Chapter 6. Characterization of modified carbon-supported cobalt catalysts[7]

## 6.1 Introduction

In Chapters 3-5, we have demonstrated that cobalt oxide on carbon catalysts ($CoO_x$/N−C[8]) are active for 1-butene oligomerization. In this chapter, we report the enhanced activity and promotional effect due to the incorporation of chromium into $CoO_x$/N−C and the high 1-butene selectivity achieved during ethylene oligomerization. Chromium itself is also a widely used active metal in the oligomerization and polymerization of ethylene both in the form of soluble metal complexes [1] (requires co-catalyst for activation) and as a $SiO_2$-supported metal oxide [2, 3]. The objective of the chapter is to highlight the insights gained from the x-ray absorption spectroscopy (XAS) characterization of chromium-promoted samples.

## 6.2 Experimental

### 6.2.1 Catalyst synthesis

The 13 wt% cobalt on carbon catalyst was synthesized based on a wetness impregnation method previously described in Chapter 3. Chromium-promoted cobalt on carbon catalysts were

---

[7] This chapter was adapted with permission from: Zhuoran Xu, Joseph P. Chada, Lang Xu, Dongting Zhao, Devon C. Rosenfeld, Jessica L. Rogers, Ive Herman, Ethylene Dimerization and Oligomerization to 1-Butene and Higher Olefins with Chromium-Promoted Cobalt on Carbon Catalyst, ACS Catal., 2018, 8 (3), pp 2488-2497.

Author contributions: Z.X. discovered and tested Cr-$CoO_x$/N-C; J.P.C. performed XAS and STEM characterization/analysis; Z.X. and J.P.C wrote the sections of the article included in this chapter.

[8] The catalyst naming convention for Chapter 6, "$CoO_x$/N-C" represents the same ammonia-treated catalyst "2A-Co/C" originally described in Chapter 3. The change in terminology in our published articles after 2016 was made for clarity and consistency amount all published works.

synthesized by identical methods using mixtures of $Co(NO_3)_2 \cdot 6H_2O$ and $Cr(NO_3)_3 \cdot 6H_2O$ (Sigma-Aldrich). The theoretical metal loadings are 8 wt.% Co and 5 wt.% Cr. Chromium-promoted cobalt on carbon catalyst with other metal loadings including 8 wt.% Co, 0 wt.% Cr; 5 wt.% Co, 8 wt.% Cr and 3 wt.% Co, 10 wt.% Cr were also synthesized and initially tested for 1-butene oligomerization. The catalyst with 8 wt.% Co and 5 wt.% Cr demonstrated the highest catalytic activity and stability among all of them. In this chapter, focus will be given to the catalyst with the best performance (8 wt.% Co, 5 wt.% Cr, denoted as Cr-$CoO_x$/N-C) for ethylene oligomerization. Chromium on carbon (without cobalt) is denoted as $CrO_x$/N-C with 4.7 wt.% theoretical Cr loading.

### 6.2.2 Catalyst characterization

X-ray absorption spectroscopy (XAS) measurements of the Cr (5.989 keV) and Co K-edge (7709 eV) were collected at beamline 12-BM of the Advanced Photon Source at Argonne National Laboratory (Lemont, Il). Catalyst samples were crushed, diluted with boron nitride (Sigma Aldrich), and pelletized in a stainless-steel sample cylinder. The cylinder was then sealed in a kapton-windowed quartz tube under the flow of He. The pelletized sample was pretreated in a tube furnace, sealed, and transferred to the beamline hutch without exposure to air. All spectra were collected at room temperature in the transmission geometry utilizing three ion chamber detectors. A metal foil placed between the last two ion chambers was used for energy calibration. Spectra of CoO, $Co_3O_4$, $CrO_3$, and $K_2CrO_4$ were collected and used as experimental standards. All spectra were processed and analyzed with the Athena and Artemis software packages using IFEFFIT [4]. An average oxidation state was calculated by a linear combination fitting of experimental cobalt standards in the range of -20 to 30 eV above the edge energy.

Scanning transmission electron microscopy (STEM) images were collected with an FEI Titan microscope equipped with a Cs aberration corrector operated at 200 kV. High-angle annular dark field (HAADF) images were obtained in the range of 54 to 270 mrad using a 0.8 nm probe and 24.5 mrad probe convergence semi-angle. Catalyst samples were suspended in ethanol with sonication then deposited on a carbon-coated copper grid (EMS). Samples were plasma cleaned for 15 min prior to analysis.

### 6.2.3 Catalytic measurement

The ethylene oligomerization reactions were conducted in a tubular down-flow fixed-bed reactor. For a typical ethylene reaction, 0.5−2.0 g of the catalyst sample was packed into a 3/8 in. stainless steel tube without diluent. All catalysts were pretreated at 230°C under 150 mL/min of flowing helium prior to reaction. The reactions were carried out at 80°C and an overall pressure of 31 bar, ethylene (UHP, Airgas) was co-fed with helium (UHP, Airgas) at 34.8 mL/min and 45.4 mL/min, respectively. The gas effluent was analyzed by an online gas chromatograph (GC-FID, Shimadzu) every 0.5 h. The liquid products were gathered from a cold trap and analyzed by a GCxGC-MS. The GC operation conditions and the compound standard information can be found in Table S4.2. Ethylene conversion, product selectivity, product yield, α-butene distribution, and weight hourly space velocity (WHSV) were calculated identically as in previous chapters.

## 6.3 Results and Discussion

### 6.3.1 Reactivity

Figure 6.1 shows ethylene conversion over both Cr-$CoO_x$/N-C and $CoO_x$/N-C catalysts. The ethylene conversion with Cr-$CoO_x$/N−C is 1.6 times as high as $CoO_x$/N-C at steady state (after 6 h TOS) at 16.3 $h^{-1}$ WHSV. Note that the chromium-promoted sample contains a much lower

amount of cobalt (8 wt% vs 13 wt%). The difference between the Cr-promoted and non-promoted catalyst was less (1.2 times) at higher WHSV (32.6 $h^{-1}$). The Cr-$CoO_x$/N-C catalyst increased in conversion slightly after the initial transient period, which was not seen with the $CoO_x$/N-C catalyst. At both WHSVs, the Cr-$CoO_x$/N-C is more stable with TOS compared to $CoO_x$/N-C. Less than 0.1% ethylene conversion was observed with $CrO_x$/N−C (at 80°C, 13.4 bar ethylene partial pressure and 65.3 $h^{-1}$ WHSV) as compared to 8.6% conversion at the same conditions with Cr-$CoO_x$/N-C. This indicates that the activity of monometallic chromium on carbon is negligible. The product selectivity was studied at different ethylene conversions by varying the WHSV from 16.3 to 65.3 $h^{-1}$ as shown in Table 6.1. Product distributions were approximately equal to those over the non-promoted $CoO_x$/N-C catalyst [5]. Similar product distributions suggest that the promotional effect enhances activity without affecting product selectivity.

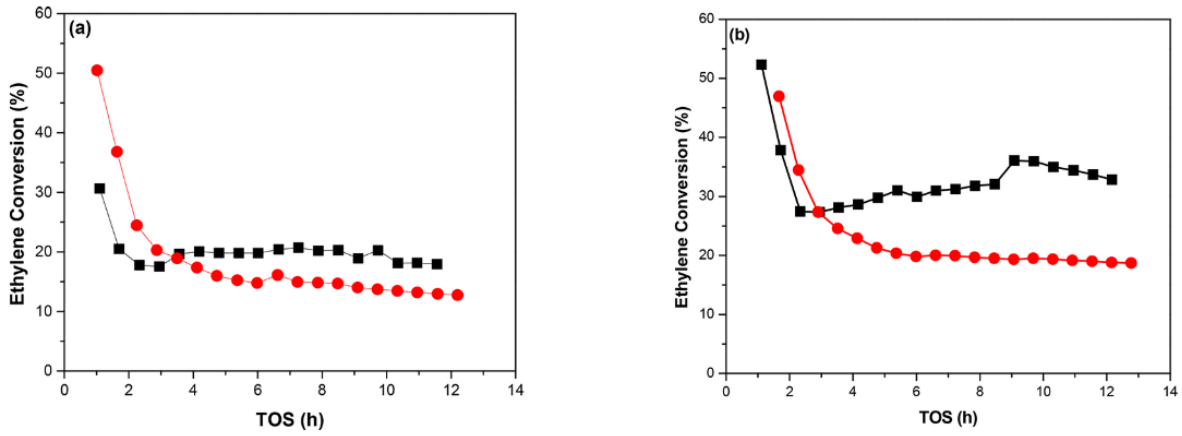


**Figure 6.1.** Ethylene conversion with time-on-stream for (black box) Cr-$CoO_x$/N-C and (red dot) $CoO_x$/N-C catalyst at (a) 32.6 $h^{-1}$ WHSV and (b) 16.3 $h^{-1}$ WHSV.

**Table 6.1.** Product selectivity and distribution of products as a function of ethylene conversion over Cr-$CoO_x$/N-C Catalyst[a]

| | | | | | |
|---|---|---|---|---|---|
| ethylene conversion (%) | | 8.6 | 20.8 | 27.3 | 32.1 |
| WHSV ($h^{-1}$) | | 65.2 | 32.6 | 21.7 | 16.3 |
| butene distribution (%) | 1-butene | 93.6 | 83.6 | 79.7 | 68.4 |
| | 2-butene | 6.4 | 16.3 | 20.2 | 31.6 |
| | total butene selectivity | 87.4 | 79.1 | 72.7 | 66.4 |
| hexene distribution (%) | 1-hexene | 31.5 | 9.8 | 7.3 | 3.4 |
| | 2- and 3-hexene | 66.7 | 88.0 | 89.3 | 93.1 |
| | 3-methyl-1-pentene | 1.7 | 2.1 | 3.3 | 3.5 |
| | total hexene selectivity | 12.4 | 14.3 | 17.7 | 20.7 |
| octene distribution (%) | 1-octene | 9.3 | 2.5 | 1.6 | 0.6 |
| | *trans*-2-octene | 7.1 | 7.9 | 8.0 | 8.8 |
| | *cis*-2-octene | 4.0 | 3.7 | 3.7 | 3.9 |
| | 3-octene | 60.5 | 63.2 | 58.2 | 63.4 |
| | 4-octene | 6.1 | 10.5 | 12.1 | 9.4 |
| | *trans*-3-methyl-2-heptene | 0.9 | 1.2 | 1.4 | 1.6 |
| | *trans*-5-methyl-2-heptene | 0.8 | 0.1 | 0.3 | 0.2 |
| | *cis*-5-methyl-2-heptene | 10.3 | 8.0 | 11.5 | 8.2 |
| | *trans*-5-methyl-3-heptene | 0.2 | 2.1 | 2.3 | 2.6 |
| | *cis*-5-methyl-3-heptene | 0.7 | 0.6 | 0.8 | 1.3 |
| | *total linear octene* | 87.1 | 87.8 | 83.6 | 86.1 |
| | total octene selectivity | 0.1 | 3.9 | 5.4 | 7.6 |

[a]Reaction conditions: 353 K, 13.4 bar ethylene partial pressure balanced in helium. Data averaged between 3.5 and 12.0 h TOS.

### 6.3.2 Characterization

The reduction of cobalt was observed to a larger extent for the Cr-$CoO_x$/N-C compared to $CoO_x$/N-C catalyst with both x-ray absorption near edge structure (XANES) and x-ray photoelectron spectroscopy (XPS; data not shown). Upon chromium addition, the Co K-edge shifted to lower energy indicative of a partial reduction of $Co^{3+}$ oxide to $Co^{2+}$ as shown in the left

side of Figure 6.2. Consistent with the XAS, XRD, and Raman spectroscopy results presented in Chapter 3[9], again the bulk cobalt oxidation state appears partially reduced compared to the most thermodynamically stable oxide, $Co_3O_4$. Our previous analysis of this effect [6] suggests that only the surface cobalt species experience the reduction because the bulk crystal structure as determined by EXAFS and XRD is primarily $Co_3O_4$. The analysis of the Cr K-edge showed that after cobalt addition, there is a shift to higher energy and more notably an increase in the intensity of the pre-edge features consistent with partial oxidation of the $Cr^{3+}$ to higher oxidation states.

The results from XANES and XPS analysis indicate a possible charge transfer from Cr to Co when both metals exist in their corresponding oxide form on the carbon support. As a group VIII metal, Co has a higher electronegativity ($\chi = 1.88$) than Cr ($\chi = 1.66$), and hence, Co would appear in a more reduced form when Cr is present. The electronic effect observed from bimetallic catalysts is very common in transition metal systems [7, 8]. The more reduced Co does not offer any advantage during the initial step where the formation of a metal-olefin complex is favored over a metal center with more electron-accepting feature [5, 9] However, the increased electron density in Co within our Cr-$CoO_x$/N-C catalyst allows for easier product desorption, [10] so that Cr-CoOx/N-C would suffer less from product olefin deposition. Our prior report hypothesized olefin product deposition as a mode of catalyst deactivation [5]. The weaker binding of the products on the Cr-CoOx/N-C catalyst could be the reason for the improved catalyst stability.

---

[9]In Chapter 4, 2A-Co/C-230 was measured with XANES. The LC fit had an average composition of 27.5% $Co^{2+}$ (CoO) and 72.5% $Co^{2+,3}$ ($Co_3O_4$).

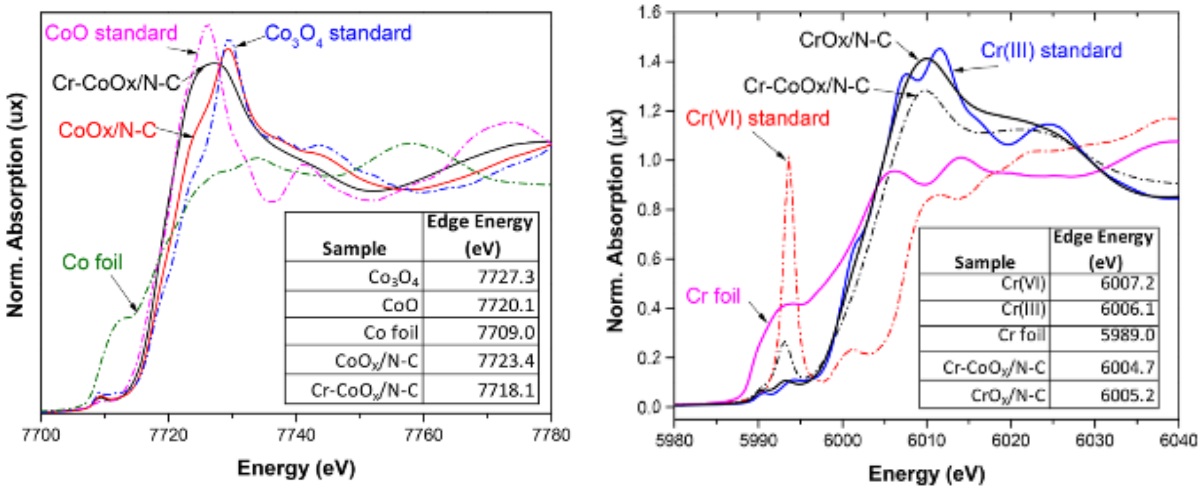


**Figure 6.2.** XANES spectra collected at the Co and Cr K edge. Left: Pink dotted trace: CoO standard; blue dotted trace: $Co_3O_4$ standard; green dotted line: Co foil; black trace: Cr-$CoO_X$/N-C catalyst; red trace: $CoO_X$/N-C catalyst. Right: Red dotted trace: Cr(VI) standard. Blue solid trace: Cr(III) standard. Pink solid trace: Cr foil. Black dotted trace: Cr-$CoO_X$/N-C catalyst. Black solid trace: $CrO_X$/N-C catalyst. The edge energy for each sample is reported in the table within each figure.

XRD patterns (not shown) were acquired of the non-promoted and promoted catalyst. No additional Cr-containing peaks were identified in the XRD patterns of Cr-$CoO_x$/N-C and CrOx/N−C, indicating that the Cr exists in either an amorphous form or with very small crystallite size. Figure 6.3 shows the STEM-HAADF image of the Cr-$CoO_x$/N-C catalyst. The high metal loading on an amorphous support resulted in a poor contrast. The particles were typically on the order of 5 nm or less. Occasionally large clusters were observed (10−50 nm). A precise particle size measurement was not obtained as it was challenging to resolve the smallest particles. The particle size observed with Cr-$CoO_x$/N-C was smaller than the particle size previously observed for $CoO_x$/N-C (5−10 nm).

Figure 6.4 shows the Co and Cr K-edge EXAFS of different catalysts. The first and second shells of $CoO_x$/N-C align with the spinel $Co_3O_4$ crystal structure. The first peak (~1.5 Å) in Figure

6.4b-d is assigned to the nearest Co−O bonds. The second (~2.5 Å) and third (3.1 Å) peaks in Figure 6.4b,c are from the two Co−Co scattering paths due to the coordination geometries of octahedral and tetrahedral Co sites [11] found in spinel structures. The spectrum of Cr-$CoO_x$/N-C shows similar shells although the features were too weak to definitively identify any Co−Cr scattering. The decrease in amplitude of the Fourier-transformed EXAFS (Figure 6.4d) can be attributed to either an increase in crystalline disorder or a decrease in particle size (i.e., lower coordination numbers). The weak scattering of higher shells (>3.5 Å) is further evidence for the high dispersion of this system.

XRD, EXAFS, and STEM collectively indicate a decrease in the particle size of the cobalt oxide on carbon for Cr-$CoO_x$/N-C compared to $CoO_x$/N-C. It should be noted that the cobalt loading of Cr-$CoO_x$/N-C (8 wt%) is less than the cobalt loading of $CoO_x$/N-C (13 wt%). This can partially explain the observed decrease in the cobalt oxide particle size with Cr-$CoO_x$/N-C. Nevertheless, geometric and electronic influences cannot often be separated. The change in geometry could alter the nature of the exposed planes and the topology of the surface sites while also affecting the electron bandwidth and binding energies of core electron [8]. When supported and properly calcined on silica, the chromium itself can act as an effective metal site for ethylene polymerization (Philips catalyst). Many studies have excluded $Cr^{6+}$ as an active oxidation state for ethylene conversion [3, 12, 13]. As reported in this study, the $Cr^{3+}$ on carbon was not active for ethylene oligomerization. The introduction of Cr has increased the dispersion and population of $Co^{2+}$ sites.

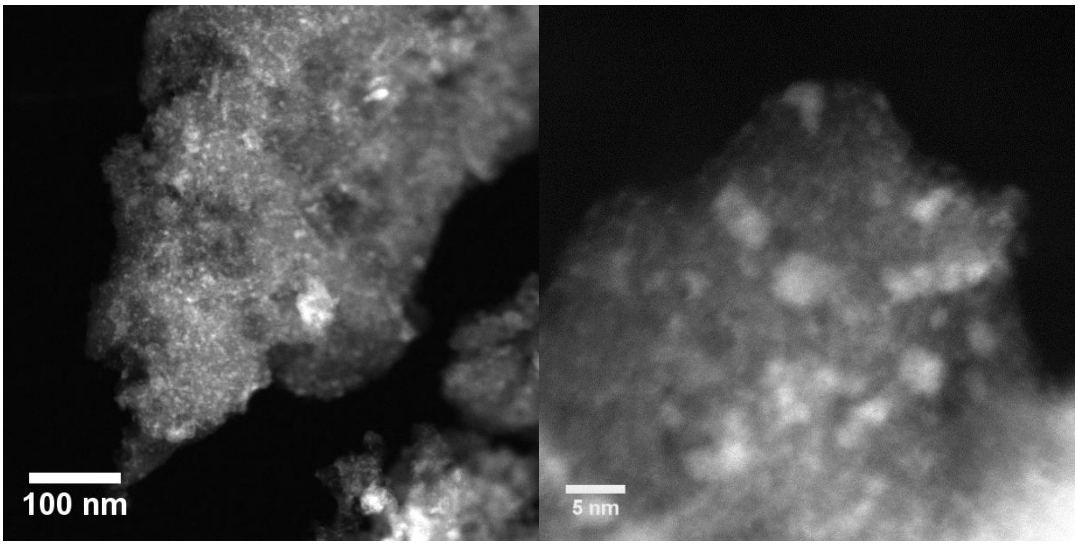


**Figure 6.3.** Representative STEM-HAADF images of Cr-$CoO_X$/N-C catalyst.

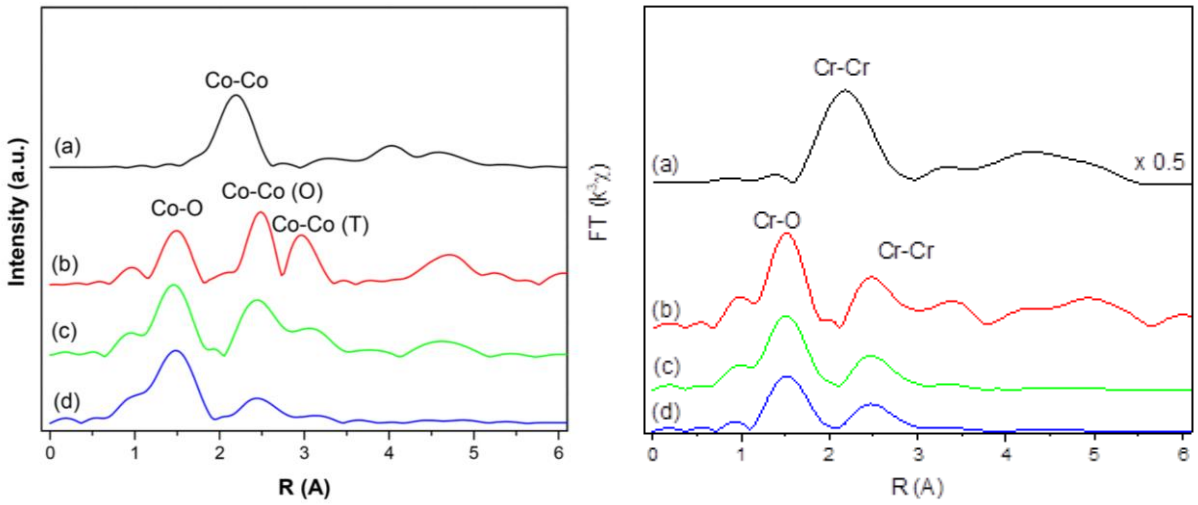


**Figure 6.4.** The $k^3$-weighted Fourier-transformed spectra from EXAFS collected at the Co and Cr K edge. Left: (a): Co foil; (b): $Co_3O_4$ standard; (c): $CoO_X$/N-C catalyst; (d): Cr-$CoO_X$/N-C catalyst. Right: (a): Cr foil; (b): $Cr_2O_3$ standard; (c): $CrO_X$/N-C catalyst; (d): Cr-$CoO_X$/N-C catalyst. All the catalysts were pretreated at 503 K in helium then cooled to RT prior to the measurement without exposure to air.

## 6.4 Conclusions

Compared to the $CoO_x$/N-C catalyst, Cr−$CoO_x$/N-C demonstrated 1.2−1.6 times higher apparent rates for ethylene oligomerization. The XANES spectra supports that the surface cobalt

species contain a high concentration of $Co^{2+}$ upon Cr addition. STEM and EXAFS results suggest a decrease of the $CoO_x$ particle size upon addition of Cr. Carbon-supported chromium (III) oxide was not active in ethylene conversion. The results presented in this chapter, combined with those in Chapter 3 and 5, suggest that $Co^{2+}$ is the most active cobalt oxidation state for olefin oligomerization.

## 6.5 References


1. R.M. Manyik, W.E. Walker, T.P. Wilson, A soluble chromium-based catalyst for ethylene trimerization and polymerization, J. Catal., 47 (1977) 197-209.
2. T. Agapie, Selective ethylene oligomerization: Recent advances in chromium catalysis and mechanistic investigations, Coordination Chemistry Reviews, 255 (2011) 861-880.
3. D.D. Beck, J.H. Lunsford, The active site for ethylene polymerization over chromium supported on silica, J. Catal., 68 (1981) 121-131.
4. B. Ravel, M. Newville, *ATHENA, ARTEMIS, HEPHAESTUS: data analysis for X-ray absorption spectroscopy using IFEFFIT*, J ournal of Synchrotron Radiation, 12 (2005) 537–541.
5. Z. Xu, D. Zhao, J.P. Chada, D.C. Rosenfeld, J.L. Rogers, I. Hermans, G.W. Huber, Olefin conversion on nitrogen-doped carbon-supported cobalt catalyst: Effect of feedstock, J. Catal., 354 (2017) 213-222.
6. D. Zhao, Z. Xu, J.P. Chada, C.A. Carrero, D.C. Rosenfeld, J.L. Rogers, I. Hermans, G.W. Huber, Cobalt Oxide on N-Doped Carbon for 1-Butene Oligomerization to Produce Linear Octenes, ACS Catalysis, 7 (2017) 7479-7489.
7. S. Hu, L. Scudiero, S. Ha, Electronic effect on oxidation of formic acid on supported Pd–Cu bimetallic surface, Electrochimica Acta, 83 (2012) 354-358.
8. B. Coq, F. Figueras, Bimetallic palladium catalysts: influence of the co-metal on the catalyst performance, J. Mol. Catal. A: Chem., 173 (2001) 117-134.
9. J.F. Hartwig, In Organotransition metal chemistry: from bonding to catalysis, in, Edward Brothers, Inc, Sausalito, CA, 210, pp. 47.
10. F.X. Cai, C. Lepetit, M. Kermarec, D. Olivier, Dimerization of ethylene into 1-butene over supported tailor-made nickel catalysts, J. Mol. Catal., 43 (1987) 93-116.
11. H.-Y. Wang, S.-F. Hung, H.-Y. Chen, T.-S. Chan, H.M. Chen, B. Liu, In Operando Identification of Geometrical-Site-Dependent Water Oxidation Activity of Spinel Co3O4, Journal of the American Chemical Society, 138 (2016) 36-39.
12. A. Zecchina, E. Groppo, Surface chromium single sites: open problems and recent advances, Proceedings of the Royal Society A: Mathematical, Physical and Engineering Science, 468 (2012) 2087-2098.
13. D.L. Myers, J.H. Lunsford, Silica-supported chromium catalysts for ethylene polymerization: The active oxidation states of chromium, J. Catal., 99 (1986) 140-148.

# Chapter 7. Conclusions and Future Work

## 7.1 Summary of conclusions

The work in this dissertation discusses our efforts to thoroughly evaluate and characterize heterogeneous catalytic materials suitable for the oligomerization of light olefins. Experimental studies were used to investigate the performance of an acidic medium-pore zeolite, H-ferrierite, and carbon-supported, cobalt oxide nanoparticles in terms of catalytic activity, selectivity, and stability for olefin oligomerization.

It was found that H-ferrierite is a suitable oligomerization catalyst at relatively low temperatures (150°C) as undesirable side reactions (i.e. cracking reactions) can be effectively suppressed. With the aid of state-of-the-art chromatography techniques, we extensively identified reaction products which were used to evaluate the reaction pathways. For all reactions conditions tested, skeletal and double-bond isomerization reactions dominated and oligomerization product mixtures had negligible levels of linear oligomers. By operating the reaction in supercritical feed conditions (1-butene, 150°C, 900 psi), stable catalytic conditions were identified which could be valuable for the upgrading olefins to highly branched fuel-range molecules.

In contrast to the highly-branched oligomerization products obtained over the acidic sites on H-ferrierite, we showed that carbon-supported cobalt oxide is an effective catalytic material to selectively produce linear oligomers. The linear oligomer composition of the $C_8$ product range from 1-butene oligomerization was as high as 87%. The selectivity from $CoO_x$/C catalysts can be rationalized assuming oligomerization proceeds via a Cossee-Arlman mechanism in which α-olefins are successively inserted into a growing cobalt alkyl. β-Hydride elimination terminates the catalytic cycle and regenerates an active site which can coordinate with another olefin. As

described in several chapters of this thesis, the effect of the support material on the partial reduction and functionalization of the cobalt surface characterization was thoroughly characterized. XAFS, XRD, Raman, and XPS all support the formation of high concentrations of $Co^{2+}$ on the surface of the $CoO_x$ particles which is believed to be the active oxidation state. Catalyst deactivation occurs due to the accumulation of oligomers as suggested by a substantial decrease in BET surface area as a function of TOS. Primary products for 1-butene dimerization were 2-, 3-, and 4-octene due to double-bond isomerization.

To demonstrate the commercial feasibility of this catalytic system to upgrade light olefins, the internal linear products from 1-butene oligomerization were collected and further upgraded to linear aldehydes via a hydroformylation reaction. The materials analyzed in this work are of interest in the development new process in the field of higher olefin or fuel production from light olefin feedstocks. An understanding of the composition and formation of selective oligomerization catalysts can be used to guide further studies to better understand the selectivity of these materials.

## 7.2 Future Work

### 7.2.1 Identification and characterization of $CoO_x$ oligomerization active site

To date, we have developed methods to synthesize, test, and characterize the bulk properties of carbon-supported, $CoO_x$ systems. We have proposed that the carbon support acts as a reducing agent during the formation of active sites; however, we do not have a complete understanding of the cobalt coordination environment required for oligomerization activity. One proposed path forward would be to synthesis and test well-defined nanoparticles that contain cobalt in different oxidation states and coordination geometries. Gu et al. [1] performed a similar study where they synthesized supported spinel oxides with various metal nitrates to identify the most

active cobalt for CO oxidation. They were able to synthesize supported $Co^{2+}$ in the tetrahedral geometry ($Co_3O_4$, $CoCr_2O_4$), $Co^{2+}$ in the octahedral geometry (CoO, $CoFe_2O_4$) and $Co^{3+}$ in the octahedral geometry ($CuCo_2O_4$). They concluded that the open octahedral geometry of $Co^{2+}$ in CoO was the most easily accessible and active for this reaction. In terms of oligomerization, a more complete understanding of the coordination environment around the cobalt active center could guide further experimental studies and be used as a starting point for theoretic efforts such as DFT to provide insights into the binding strength of the olefin intermediates.

### 7.2.2 Identification of stable catalytic conditions/catalysts

While the linear olefin selectivity of $CoO_x$/C is one of the highest reported in literature for a heterogeneous material, the catalysts deactivate rapidly thus limiting the potential applications. Surface area measurements ($N_2$ isotherms) suggest that oligomer build-up within the pores of the catalyst pore-filling is substantial. If conditions were identified where deactivation was moderated it would be possible to further investigate methods of increasing the activity and selectivity towards linear products. Agirrezabal-Telleria and Iglesia [2] recently reported on a Ni-MCM-41 catalyst for ethylene dimerization that experienced similar rates of deactivation as cobalt oxide at 448 K. They demonstrated that by operating at sub-ambient conditions (240-260 K) the activity was stable. The stable operation was attributed to the condensation of ethylene within the mesopores of MCM-41 at sub-ambient temperature.

### 7.2.3 Kinetic modelling of the reaction network

The ability of $CoO_x$/C to oligomerize ethylene at low temperatures with minimal side reactions makes it an attractive process for producing either linear fuels or chemicals. Though we have characterized many of the $C_4$-$C_8$, we do not have the ability to predict changes in activity and

selectivity at various reaction conditions. The development of a kinetic model would enable us to better understand the effect of material modifications in terms of quantitative kinetic descriptors. Toch and co-workers [3] used this approach to model ethylene oligomerization over Ni/$SiO_2$-$Al_2O_3$ with sufficient accuracy by making simplifying assumptions about the product mixture. Their method of single event microkinetic modeling (SEMK) accounts for only the skeletal composition of product molecules (i.e. 1-, 2-, 3-, and 4-octene would be in the sample family of products and have one single event rate coefficient). By grouping products into families with similar structures, they were able reduce the number of kinetic parameters that need to be solved.

## 7.3 References

1. D. Gu, C.-J. Jia, C. Weidenthaler, H.-J. Bongard, B. Spliethoff, W. Schmidt, F. Schüth, Highly Ordered Mesoporous Cobalt-Containing Oxides: Structure, Catalytic Properties, and Active Sites in Oxidation of Carbon Monoxide, Journal of the American Chemical Society, 137 (2015) 11407-11418.
2. I. Agirrezabal-Telleria, E. Iglesia, Stabilization of active, selective, and regenerable Ni-based dimerization catalysts by condensation of ethene withinordered mesopores, J. Catal., 352 (2017) 505-514.
3. K. Toch, J.W. Thybaut, G.B. Marin, Ethene oligomerization on Ni-SiO2-Al2O3: Experimental investigation and Single-Event MicroKinetic modeling, Appl. Catal. A: Gen., 489 (2015) 292-304.